Probing the Depths: Relativistic, Hydrodynamic Simulations and X-ray Observations of Pulsar Wind Nebulae

by

Joseph P. Bernstein

A dissertation submitted in partial fulfillment
of the requirements for the degree of
Doctor of Philosophy
(Astronomy and Astrophysics)
in The University of Michigan
2008

Doctoral Committee:

Research Scientist Philip A. Hughes, Chair
Professor Hugh D. Aller
Professor Joel N. Bregman
Professor R. Paul Drake
Professor Douglas O. Richstone

No matter where you go, there you are.

– popularized by Buckaroo Banzai, 1984;
likely adapted from Confucius.

For my wife and family, my teachers and mentors, and the human pursuit of fundamental, but non-fundamentalist, scientific knowledge.

ACKNOWLEDGMENTS

This dissertation, as with any other, greatly benefited from the help of numerous persons to whom I am eternally grateful; thank you. In particular, I thank the members of my dissertation committee for their invaluable guidance. Rebecca Bernstein (no relation), formerly of the University of Michigan Department of Astronomy, served on my committee from 02/2003 through 07/2007). The observational aspects of this work greatly benefited from collaboration, discussion, and consulatation with Ilana M. Harrus, Patrick O. Slane, Bryan M. Gaensler, John P. Hughes, David Moffett, and Richard Dodson. I am grateful to Steve Kuhlmann of Argonne National Laboratory for providing access to computing resources. I thank Norman and Marged Bernstein for proof reading this document, not once but twice. Funding was provided by the University of Michigan Rackham Graduate School and Department of Astronomy, the National Aeronautics and Space Administration (NASA), and via the individual grants of Robert Petre and Ilana M. Harrus of the NASA/Goddard Space Flight Center, and Philip A. Hughes of the University of Michigan Department of Astronomy.

CONTENTS

LIST OF FIGURES

Figure

LIST OF TABLES

CHAPTER 1

Introduction

At the end of a massive star's life, the collapse of its core to a compact object, i.e., a neutron star or black hole, drives a shockwave into its outer layers, thereby heating and ejecting them into the interstellar medium (ISM) in a supernova (SN) explosion. Subsequently, the shockwave overtakes the ejecta and expands into the ISM forming a supernova remnant (SNR). Typically, a SN releases $\sim 10^{51}$ erg of mechanical energy that drives expansion of the SNR, sweeping up ISM material, heating it to X-ray temperatures and infusing it with metals (fusion products beyond Lithium), which are available for the formation of new stars and planetary systems, and the evolution of life.

In a subclass of SNRs, for progenitor masses between 10 and 25 solar masses (e.g., Heger et al., 2003), the compact object formed in the SN explosion is a rapidly-spinning, highly-magnetized neutron star surrounded by a magnetosphere of charged particles. The combination of the rotation and the magnetic field gives rise to extremely powerful electric fields that accelerate charged particles to high velocities. The magnetic field interacts with the charged particles resulting in the spin-down of the neutron star and the release of spin-down energy. A relatively small fraction of this energy is converted into beamed emission manifest as an apparent pulse if the neutron star's rotation sweeps the beam across the Earth; hence the designation "pulsar". The bulk of the spin-down energy is converted into a pulsar wind (Michel, 1969) which is terminated at a strong shock, downstream of which the flow is indistin-

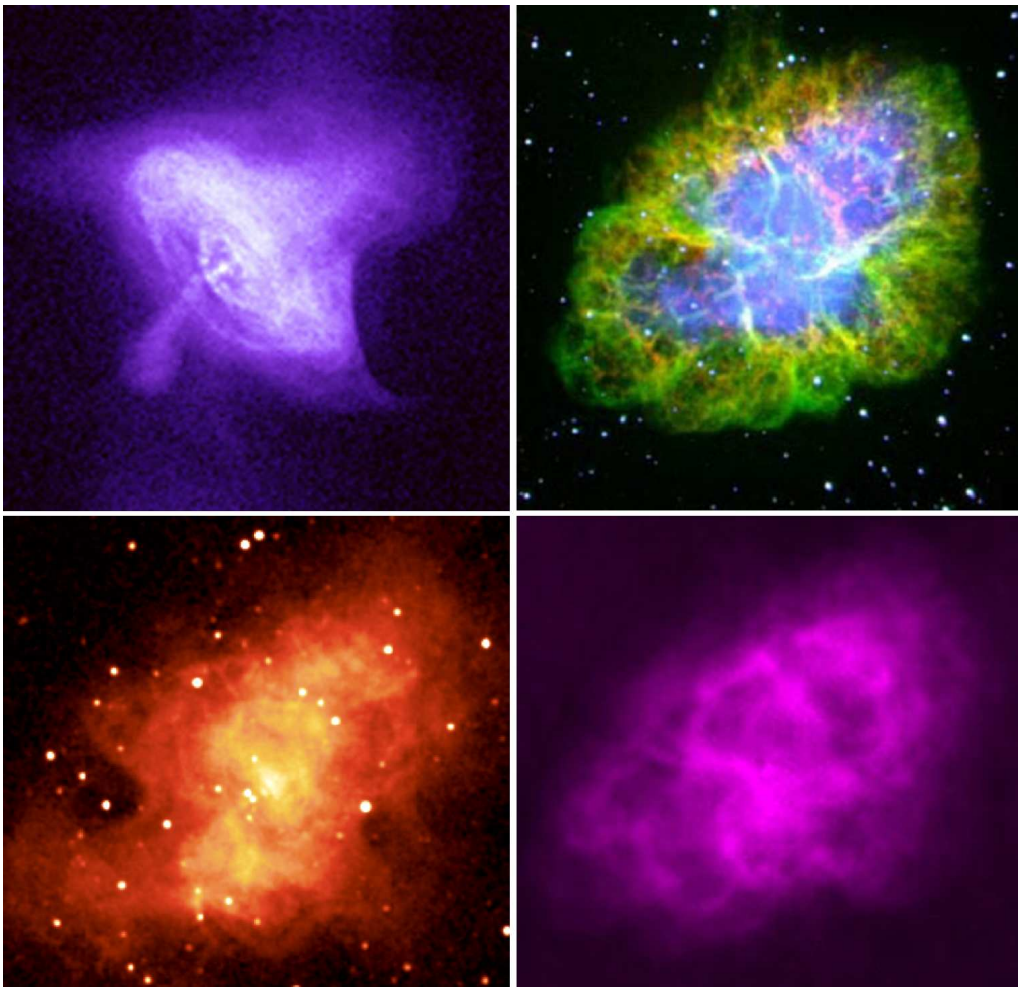

Figure 1.1: Multi-band images of the Crab nebula. Clockwise from the upper left are X-ray, optical, infrared, and radio images. Note that the images are not to scale. Credits: NASA/CXC/SAO (X-ray), Palomar Observatory (optical), 2MASS/UMass/IPAC–Caltech/NASA/NSF (infrared), NRAO/AUI/NSF (radio).

guishable from being spherically symmetric (e.g., Chatterjee & Cordes, 2002, see §1.2 for a detailed discussion). The wind particles interact with the magnetic field causing them to emit synchrotron radiation, forming a pulsar wind nebula (PWN). The Crab Nebula (see Fig. 1.1), formed in the SN explosion of 1054 CE, is the canonical object of this type. The Crab exhibits pulsations from the radio, all the way up to X-rays, and is a prodigious source of γ-rays.

The wind in the immediate vicinity of the pulsar is a diffuse, relativistic gas unlikely to be directly observable. However, the classic structure of forward and reverse

shocks separated by a contact surface (Weaver et al., 1977) arises from the interaction of the wind with the SNR or ISM. A probe of this interaction is provided by optical emission from the swept-up ambient ISM, thermal X-ray emission from the SNR and/or the shocked ISM, and X-ray synchrotron emission from the shocked wind. Furthermore, the high space velocity that is typical of pulsars (Cordes & Chernoff, 1998) implies an asymmetric ram pressure on the pulsar wind from the denser ambient medium. The details of the morphology and of the distribution of the density, pressure, and velocity within the PWN depend upon the density, speed, momentum, and energy flux of the pulsar wind. Thus, comparison of PWN simulations with observational data can provide an unparalleled method for investigating pulsar winds and, therefore, how the surrounding medium taps the rotational energy of the pulsar.

Pacini & Salvati (1973) and Rees & Gunn (1974) pioneered the basic model of PWNe; a model further developed by Kennel & Coroniti (1984a,b) and Emmering & Chevalier (1987). An excellent observational review of PWNe studies is Gaensler & Slane (2006); Bucciantini (2008) is the theoretical counterpart. For a number of reasons, a detailed, quantitative study of PWNe is now particularly timely. First, there is a cornucopia of high quality data from space-born observatories such as the *Chandra* X-ray Observatory and XMM-Newton. Second, even recent hydrodynamic simulations (e.g. Bogovalov et al., 2005; van der Swaluw et al., 2004) do not incorporate cooling, and, as stressed by Bucciantini (2002), the development of realistic models is crucial to the interpretation of observational PWNe data. Third, the total energy radiated by PWNe accounts for only a small fraction of the spin-down energy, leaving a large energy reservoir available for interaction with the SNR and the acceleration of ions, the partitioning of which is not well understood.

1.1 Evolution of Pulsar Wind Nebulae

The evolution of PWNe can be broken into four broad phases: 1) free-expansion, 2) SNR reverse shock interaction, 3) expansion inside a Sedov SNR, and 4) bow shock formation. In what follows, I briefly discuss these stages. For a detailed treatment, see Gaensler & Slane (2006), and references therein.

1.1.1 PWN in freely expanding SNR

The blastwave generated by a SN explosion initially expands freely at speeds of order 10^3 km s^{-1}. In general, the explosion is not perfectly symmetric, giving the newly formed pulsar a space or "kick" velocity with typical values in the range 4–5 $\times$ 10^2 km s^{-1}, but with known examples exceeding 10^3 km s^{-1}. The pressure in the SNR is much lower than that of the pulsar wind and the wind expands freely and rapidly. During this stage, and for the spherically symmetric case, van der Swaluw et al. (2001) showed that the time dependence of the nebula radius is given by:

$$R_{pwn}(t) \simeq 0.889 \left(\frac{L_0 t}{E_0}\right)^{1/5} V_0 t \propto t^{6/5}, \tag{1.1}$$

where E_0 is the total mechanical energy of the SN explosion, L_0 is the pulsar's mechanical luminosity, $V_0 \equiv \sqrt{(10E_0/3M_{ej})}$, and M_{ej} is the mass of the SN ejecta, while noting that Chevalier (1977) and Reynolds & Chevalier (1984) had previously obtained the $t^{6/5}$ relation. In this stage, the PWN *is* observationally quite symmetric as exemplified by the case of G21.5–0.9 (e.g., Matheson & Safi-Harb, 2005, see Fig. 1.2). One can readily show that the magnitude of the expansion velocity from Eqn. 1.1 far exceeds the sound speed in the SNR.

1.1.2 PWN–SNR reverse shock interaction

During the free expansion stage, the reverse shock generated in the SN explosion travels outward with the blastwave due to the ram pressure of the outwardly streaming stellar ejecta (see Fig. 1.2 for a schematic). As the radius of the SNR increases, the

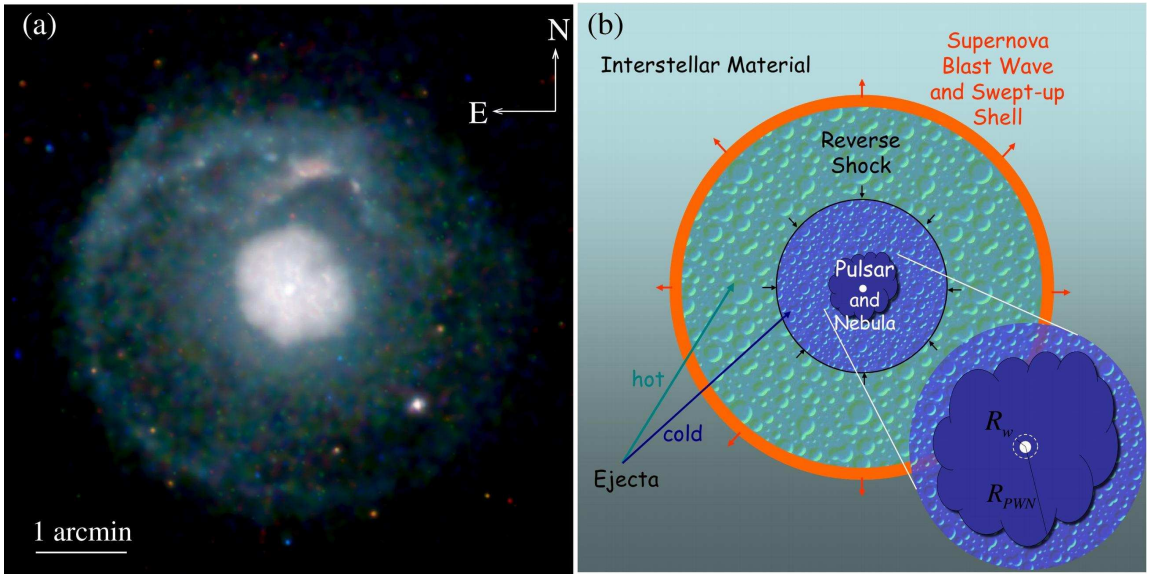

Figure 1.2: Gaensler & Slane (2006) Fig. 2. *Left:* a *Chandra* image of G21.50.9 (Matheson & Safi-Harb, 2005), an example SNR housing a symmetric PWN. *Right:* illustrative PWN schematic. Note that this picture does not directly correspond to G21.50.9 as it is unlikely that the reverse shock has detached from the boundary shock in this young SNR.

ram pressure decreases while the blastwave sweeps up increasing amounts of ISM material. Once the blastwave has swept up a few times the ejecta mass the reverse shock "detaches" (van der Swaluw, 2005, and references therein), travels back toward the center of the remnant, and interacts with the PWN. The free expansion of the nebula lowers its internal pressure to a value far below that in the SNR. The reverse shock collides with the nebula in a time given by Reynolds & Chevalier (1984):

$$t_{col} = 1 \times 10^4 \left(\frac{M_{ef}}{15 M_\odot}\right)^{5/6} \left(\frac{E_0}{10^{51}\ \mathrm{erg}}\right)^{-1/2} \left(\frac{n_0}{1\ \mathrm{cm}^{-3}}\right)^{-1/3} \mathrm{yr}, \tag{1.2}$$

where n_0 is the number density of the ambient material. This is the onset of the reverberation stage of the SNR during which time the PWN is compressed until the internal pressure is increased to the point where the nebula is able to push back and suddenly expand, causing the pressure to drop and the whole process to repeat (e.g., van der Swaluw et al., 2001). This is a complicated, three-dimensional interaction that can leave the nebula with a crumpled, asymmetric shape.

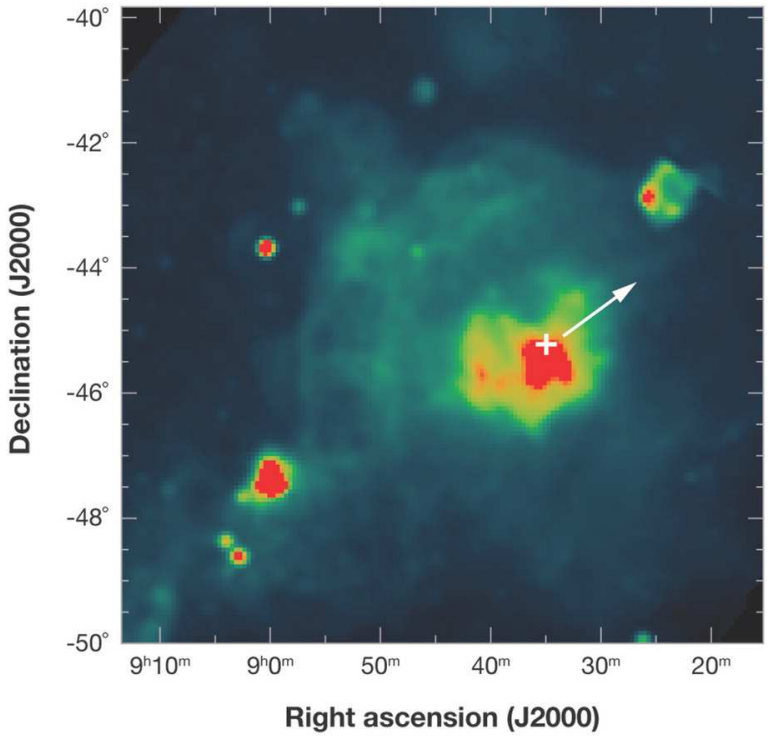

Figure 1.3: A Parks 2.4 GHz image (Duncan et al., 1996) of G263.93.3 (Vela) showing the SNR and central PWN. The cross marks the position of the pulsar while the arrow shows its direction of motion (Dodson et al., 2003). The reverse shock interaction scenario is strongly supported by the distorted shape of the PWN, as well as by the location and motion of the pulsar. Source: Gaensler & Slane (2006).

This interaction will, in general, depend on both the structure of the ISM, into which the SNR forward shock expands, and the space motion of the pulsar (van der Swaluw, 2005). As further discussed by van der Swaluw (2005), simulations by Blondin et al. (2001) and van der Swaluw et al. (2004) show that a two-component PWN structure results with 1) a relic nebula containing the majority of the particles supplied by the pulsar since its formation and 2) a new, smaller nebula associated with the active injection of wind particles. The new nebula will be X-ray bright and dimmer in the radio, relative to the relic nebula, which will be X-ray dim. This is due to the fact that the magnetic field in the relic nebula is intensified by the crushing event, and that the synchrotron lifetime of radio-emitting particles is much longer than their X-ray emitting counterparts.

The timescale for this crushing event is comparable to that for the previous free expansion stage (van der Swaluw, 2005, and references therein) implying that a significant number of observed PWNe should be experiencing this interaction. The classic example of such a system is the Vela SNR (see Fig. 1.3) and I argue in Chap. 2 that the hitherto mysterious SNR MSH 11–6*2* is another.

1.1.3 PWN in a Sedov-Taylor SNR

After the reverberations of the reverse shock die down, which happens quickly compared to the time in Eqn. 1.2, the reverse shock has traveled all the way back to the center of the SNR, re-energizing the interior of the remnant, and bringing the PWN into pressure equilibrium with the thermal SNR. This results in a large increase in the sound speed, and the nebula subsequently expands subsonically into the remnant. During this phase, for a constant pulsar luminosity, the evolution of the remnant can be approximated by the analytical Sedov-Taylor solution (Taylor, 1950a,b; Sedov, 1959) and the radius of the nebula evolves as (van der Swaluw et al.,

2001, and references therein):

$$R_{pwn}(t) \simeq 0.421 \left(\frac{L_0 t}{p_i(t)} \right)^{1/3} \propto t^{11/15}, \tag{1.3}$$

where, if $R_{pwn} \ll R_{snr}$ (the radius of the remnant), $p_i(t)$ can be taken to be the central pressure from the Sedov-Taylor solution with 5/3 for the adiabatic index of the ambient medium (van der Swaluw et al., 2001):

$$p_i(t) \simeq 0.074 \left(\frac{E_0}{R_{snr}^3} \right) \propto t^{-6/5}. \tag{1.4}$$

As discussed by van der Swaluw et al. (2001), the result immediately above is not very realistic by the time the reverse shock interaction stage is complete because the luminosity of the pulsar is more realistically governed by the luminosity evolution of a rotating magnetic dipole:

$$L(t) = \frac{L_0}{\left(1 + \frac{t}{\tau}\right)^2}. \tag{1.5}$$

The initial pulsar spin-down timescale, τ, is given by:

$$\tau \equiv \frac{P_0}{(n-1)} \left(\frac{dP_0}{dt} \right)^{-1}, \tag{1.6}$$

where P_0 is the initial period of the pulsar and n is the breaking index (equal to 3 for a dipole). This necessitates a numerical solution to the PWN energy-balance equation. Neglecting the initial free-expansion stage, van der Swaluw et al. (2001) found:

$$R_{pwn} \propto t^{3/10}, \tag{1.7}$$

in agreement with the pressure equilibrium result of Reynolds & Chevalier (1984). Gaensler & Slane (2006) note that the realm of applicability of Eqns. 1.3 & 1.7 is quantitatively distinguished by whether $t < \tau$ or $t > \tau$.

1.1.4 PWN bow shock formation

The time it takes for the pulsar to cross the SNR was obtained by van der Swaluw et al. (2003):

$$t_{cr} = 1.4 \times 10^4 \left(\frac{E_0}{10^{51}\ \mathrm{erg}}\right)^{1/3} \left(\frac{v_{psr}}{10^3\ \mathrm{kms}^{-1}}\right)^{-5/3} \left(\frac{n_0}{1\ \mathrm{cm}^{-3}}\right)^{-1/3}, \tag{1.8}$$

where v_{psr} is the velocity of the pulsar. Once the PWN-SNR system has evolved to the Sedov-Taylor stage, the time elapsed is sufficiently large that it is possible for the pulsar to have reached the edge of the nebula, or even beyond (van der Swaluw et al., 2001). Thus, the pulsar escapes its original wind bubble, leaving behind a "relic" PWN, and traverses the SNR while inflating a new PWN. As the pulsar moves away from the center of the remnant, the sound speed decreases. Following van der Swaluw et al. (1998), van der Swaluw et al. (2004) calculated the Mach number of the pulsar, $\mathcal{M}_{psr}$, and found that $\mathcal{M}_{psr}$ exceeds unity after a time $t = 0.5t_{cr}$, at which point the pulsar has traveled a distance $R_{psr} \simeq 0.677R_{snr}$, and the nebula is deformed into a bow shock. The condition on the pulsar velocity for this transition to occur while the remnant is in the Sedov-Taylor phase is given by (van der Swaluw et al., 2004, and references therein):

$$v_{psr} \geq 325 \left(\frac{E_0}{10^{51}\ \mathrm{erg}}\right)^{1/17} \left(\frac{n_0}{1\ \mathrm{cm}^{-3}}\right)^{2/17} \mathrm{km\ s}^{-1}, \tag{1.9}$$

a relation showing a strikingly weak dependence on the physical parameters. A significant fraction (30–40% depending on the velocity distribution model) of the pulsars compiled by Arzoumanian et al. (2002) satisfy this condition. As shown by van der Swaluw et al. (2003), once the pulsar reaches the edge of the remnant, its Mach number is $\mathcal{M}_{psr} \simeq 3.1$. Subsequently, the pulsar moves through the ISM where its velocity corresponds to a hypersonic Mach number typically on the order of 10^2.

The most famous example of a PWN in this stage is the Guitar nebula (Cordes et al., 1993, see Fig. 1.4), so named because of its cometary neck connecting to a

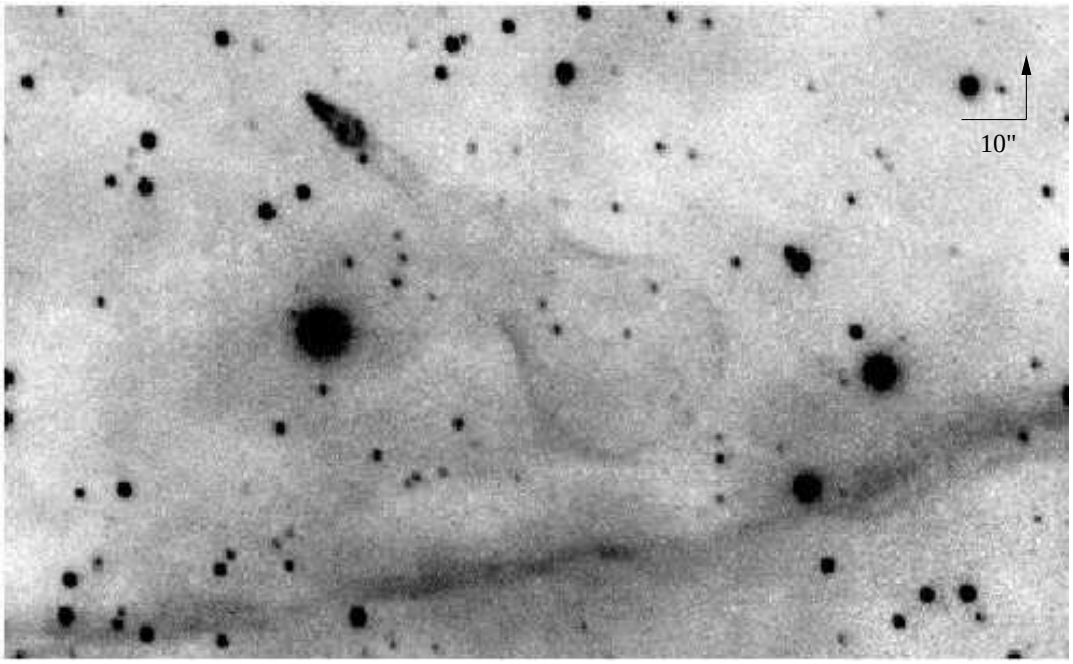

Figure 1.4: A 1995 Hale Telescope Hα image of the Guitar Nebula (20 at 6564 angstroms; Chatterjee & Cordes, 2002). The cometary neck connecting to a spherical bubble is clearly evident.

bubble. Fig. 1.5 shows numerous other examples. A case of particular import to this work is that of the X-ray emission associated with PSR1929+10 (see Fig. 1.6). Wang et al. (1993) posited that the morphology is due to a relativistic backflow behind the pulsar, a suggestion that has gone unconfirmed for realistic wind Lorentz factors and pulsar velocities, and was a prime motivator for this project. The simulations in Chap. 5 directly probe the morphology and interior structure of PWNe during this phase, motivate how the shape of the Guitar nebula persists, without resorting to tailored ISM geometry, and confirm the interpretation of Wang et al. (1993).

1.2 The Current State of Pulsar Wind Nebulae Studies

The last decade has seen an explosion in the depth and breadth of the PWNe field. Observations from the *Chandra* X-ray Observatory and XMM-Newton have fleshed out structures of the inner nebula that, due to advances in computing, simulations

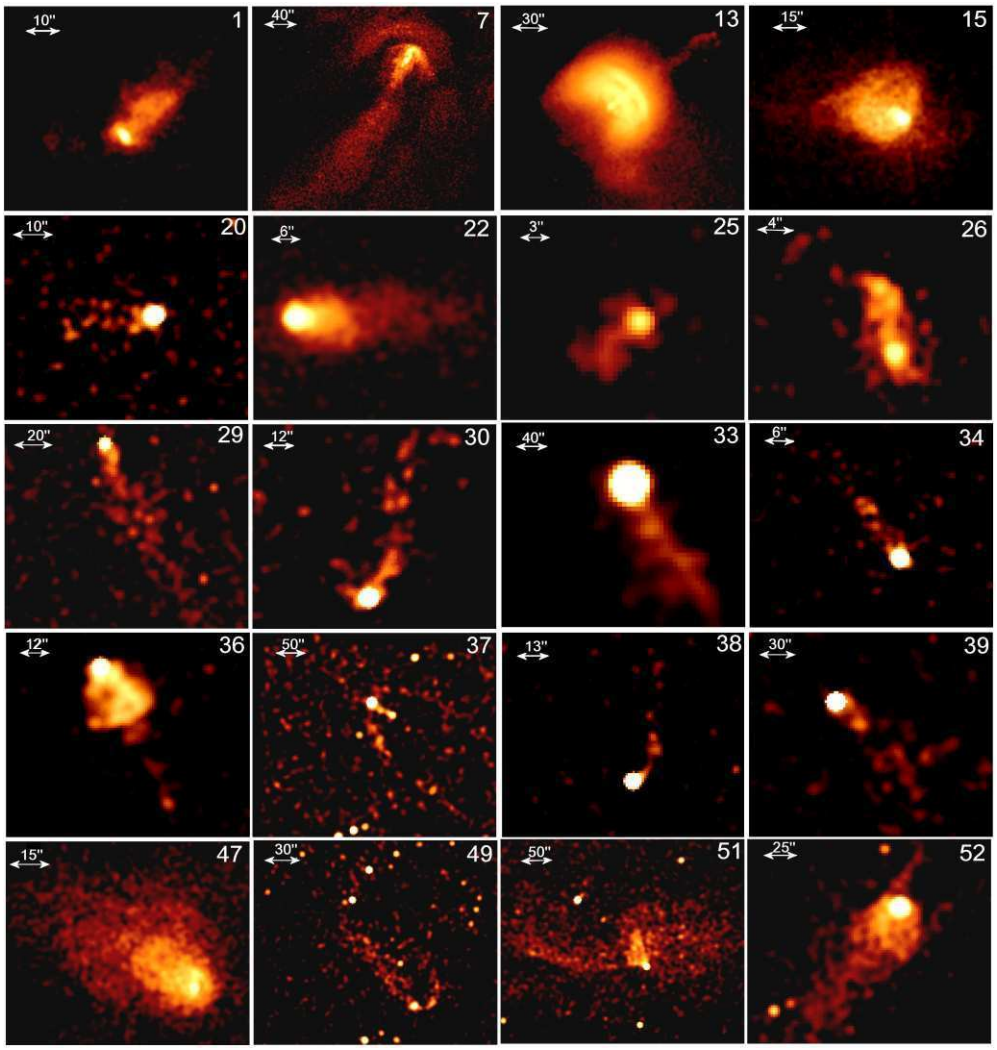

Figure 1.5: X-ray images where the morphology of PWNe is influenced by the pulsar motion. The numbers on each image correspond to entries in tables found in the paper. Credit: Kargaltsev & Pavlov (2008).

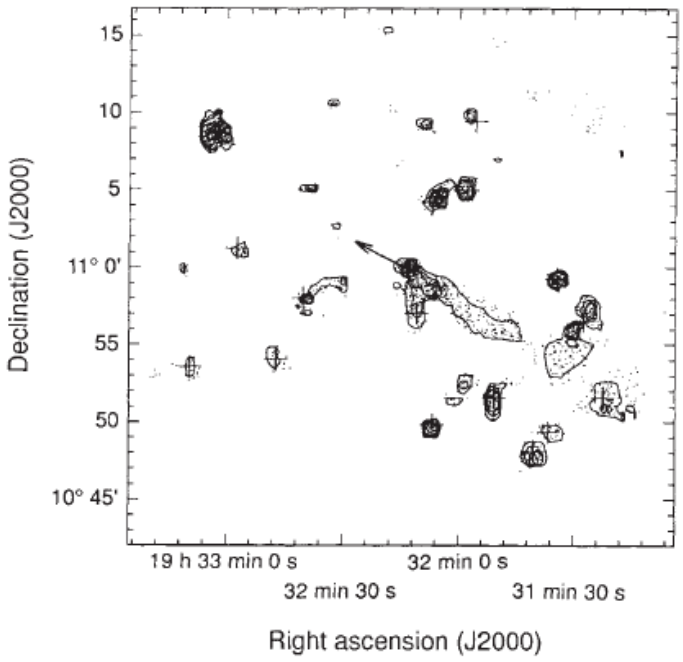

Figure 1.6: *R*OSAT X-ray surface brightness in the field of PSR1929+10 showing the X-ray tail. Wang et al. (1993) suggested that the X-ray morphology is due to the acceleration of particles behind the pulsar forming a relativistic backflow. North is up and East is left. Credit: Wang et al. (1993).

have been able to reproduce. For the first time, detailed, realistic models of PWNe from bow-shock systems, such as the Guitar, to young, energetic systems like the Crab seem to be within reach.

1.2.1 Observations

PWNe exhibit a non-thermal spectrum continuous from the radio to the X-ray band. The model has long been synchrotron emission arising from the helical motion of charged particles in the nebular magnetic field. This model clearly explains why the Crab appears smaller at higher frequencies (e.g., Bucciantini, 2008) due to the fact that the higher energy emitting particles radiate their energy at preferentially higher rates. However, not all PWNe exhibit this size difference. A notable example is 3C 58, where the lack of a size difference has been attributed to the lower magnetic field (e.g., Gaensler & Slane, 2006).

Figs. 1.1 & 1.7 show amazingly detailed images of the Crab nebula revealing the inner structures of the nebula. Clearly evident are the torus arising from the toroidal magnetic field, and collimated polar emission (see §1.2.2 for a discussion of the physics behind these features). Also present is a bright inner ring that has been interpreted as marking the location of the wind termination shock. This "jet/torus" morphology has been observed in other PWNe, e.g., 3C 58 (see Fig. 1.8) and has become the standard picture for the interior regions of young PWNe (see Fig. 1.9 for additional examples). In order to explain the dynamics and emission properties of PWNe, the bulk wind Lorentz factor has been estimated to be on the order of 10^6 (e.g., Bucciantini, 2008). The toroidal magnetic field model explains why many young PWNe, such as the Crab and 3C 58, have ellipsoidal shapes, as the field exerts more pressure along the poles than on the equator (Bucciantini, 2008, and references therein). A classic question that remains, however, is what happens to the pulsar's magnetic field? As renewed by Arons (2002), simple arguments conclude that the magnetization, $\sigma \equiv$ (Poynting flux)/(kinetic energy flux), should be invariant and, unless the current pulsar paradigm is completely wrong, $\sigma \gg 1$ must hold near the pulsar (Arons, 2002). However, observations indirectly imply $\sigma \ll 1$ for the post-termination-shock flow. This is the long-standing "σ problem", the solution to which remains an active research issue (e.g., Arons, 2002; Contopoulos & Kazanas, 2002; Kirk & Skjæraasen, 2003; Lyutikov, 2003; Vlahakis, 2004).

There is an apparent contradiction between the toroidal magnetic field and the essentially spherically symmetric shape typical of PNWe (recall G21.50.9 in Fig. 1.2). Indeed, the Poynting flux near the pulsar goes as $sin^2(\theta)$, while Chatterjee & Cordes (2002) used $H\alpha$ observations of bow shock nebulae to argue that the post-termination-shock flow is indistinguishable from being isotropic. The resolution lies in the fact the wind undergoes a violent change as it transitions from an order 10^6 Lorentz-factor flow to an order unity flow across the termination shock. This sets up large pressure

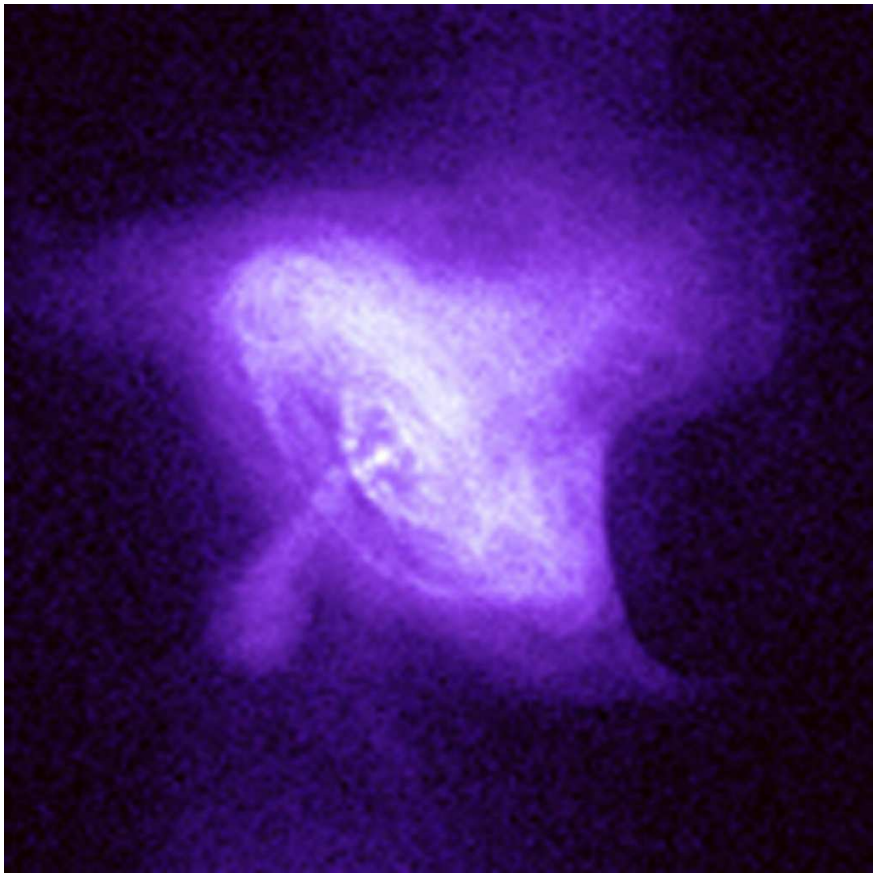

Figure 1.7: A *Chandra* X-ray image of the Crab nebula showing the core jet/torus structure. The bright, inner ring has been identified as marking the termination shock of the wind. Credit: NASA/CXC/SAO.

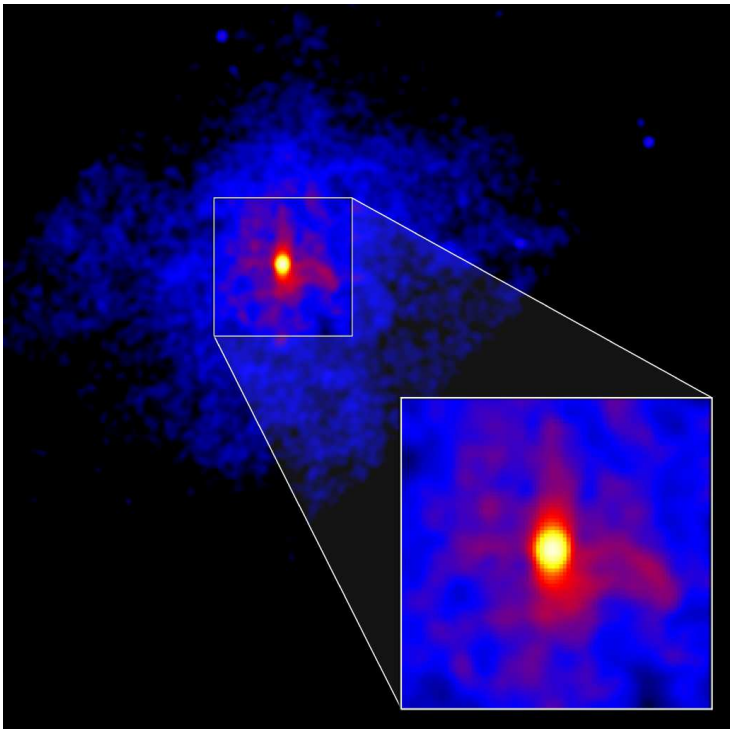

Figure 1.8: A *Chandra* X-ray image of 3C 58 that strongly suggests an inner jet/torus structure. Credit: NASA/SAO/CXC/Slane et al. (2004).

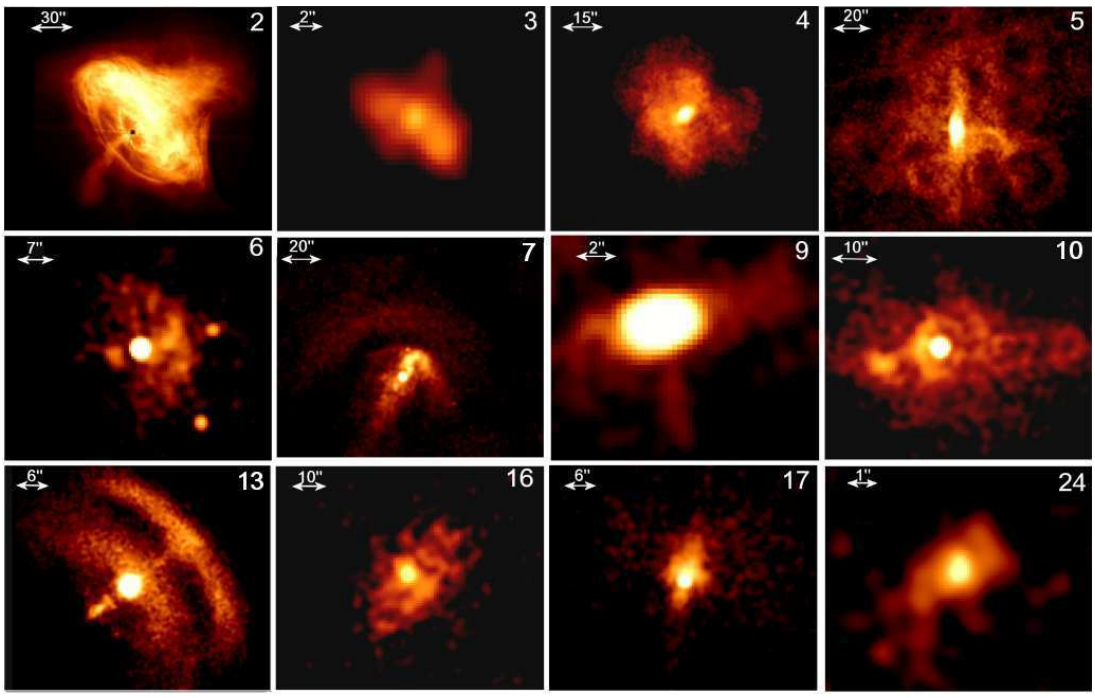

Figure 1.9: X-ray images of PWNe with a toroidal component. The numbers on each image correspond to entries in tables found in the paper. Credit: Kargaltsev & Pavlov (2008).

gradients that smear out the toroidal geometry and produce the essentially spherically symmetric post-shock flow. This is the justification for the radial wind flow used for the simulations presented in Chap. 5.

1.2.2 Simulations

Efforts to model PWNe span three decades (with seminal papers Rees & Gunn, 1974; Kennel & Coroniti, 1984a,b; Emmering & Chevalier, 1987). While the case for a non-isotropic pulsar wind energy flux has long been made (Michel, 1973), only recently has a theoretical explanation of the mechanism behind the jet/torus structure has been put forward and have the predictions of Michel (1973) been confirmed (Bucciantini, 2008). In particular, Bucciantini (2008) highlighted that a detailed description has been made possible by the increase in the efficiency and robustness of relativistic, numerical MHD codes, citing Komissarov (1999), Del Zanna et al. (2003) and Gammie et al. (2003).

Fig. 1.10 depicts simulations by Del Zanna et al. (2004) showing that jet formation in PWNe is intimately related to the magnetization inside the nebula. In particular, these results show that jet formation is tied to where the magnetic field attains equipartition. Once equipartition is reached, the magnetic field can no longer be compressed. If this happens close to the termination shock, then, due to the mildly relativistic nature of the post-shock flow, hoop stresses can become efficient, and most of the flow is diverted back toward the axis and collimated. The magnitude of the magnetization is key: if it is too small, equipartition is reached outside the nebula, hoop stresses remain inefficient, and no collimation is produced.

While higher levels of magnetization are required to produce collimation, they inhibit the formation of the torus because the equatorial flow is diverted back toward the axis. How then does the torus arise? The simulation results of Del Zanna et al. (2004) provide a suggestion. The key lies in the fact that pulsars are almost certainly

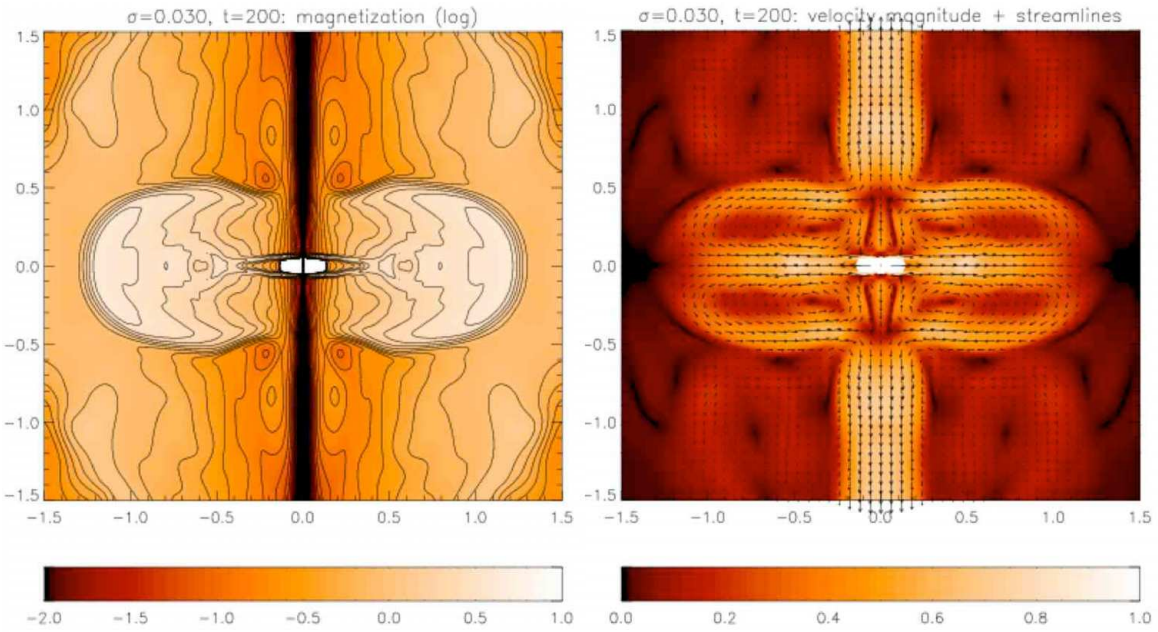

Figure 1.10: MHD simulations by Del Zanna et al. (2004) addressing the formation of the polar flow responsible for the beamed emission for an aligned rotator. Left: the nebula magnetization. Right: the flow velocity. The magnetization is higher in the equatorial regions, and so equipartition is reached sooner at lower latitudes. Once this occurs, magnetic pressure prevents further compression of the magnetic field and hoop stresses are able to set up collimation. If the magnetization is high enough, then equipartition is reached within the nebula, and most of the plasma is diverted back toward the poles and a collimated flow is produced. Credit: Bucciantini (2008).

oblique rotators. The misalignment of the spin axis and the magnetic poles results in a folded current sheet, and dissipation of the magnetic field can lead to a null magnetization at the equator (Bucciantini, 2008, and references therein). This results in the equatorial flow achieving equipartition outside the nebula and an equatorial channel persists far into the post-shock flow (see Fig. 1.11). At higher latitudes, however, magnetic field dissipation is far weaker, allowing equipartition to be reached much sooner, resulting in the diversion of the flow and collimation (as discussed above). As stressed by Bucciantini (2008), results about the details of the stripped wind region show a direct link to the strength of the collimated flow and the size of the termination shock (Del Zanna et al., 2006), both of which are observable. Photon-index maps present another observable test for PWNe. Fig. 1.12 shows a simulated map by Bucciantini (2008) compared to an observed map by Mori et al. (2004). While the main features are well simulated, the spectrum of the jet was not able to be reproduced without wiring in assumptions about the physics of the collimated flow. Bucciantini (2008) suggests that this failure might be due to effects not captured by axisymmetric simulations. This result highlights the fact that there are still many important pieces left to solve.

The discussion above applies to the central engine that powers young PWNe, and the modeling involved addresses the inner jet/torus structures. Other modeling is concerned with the *global* structure of PWNe such as, for example, that presented in Chaps. 5 & 6. In particular, recall the bow-shock PWNe representing the later stages of PWN evolution discussed in §1.1.4. Bucciantini et al. (2005) and Vigelius et al. (2007) are two recent examples of simulations addressing such a system. Bucciantini et al. (2005) were the first to apply a fully-relativistic MHD code (Del Zanna et al., 2003; Del Zanna & Bucciantini, 2002), and, for an axisymmetric geometry, obtained a relativistic backflow behind the pulsar, as predicted by Wang et al. (1993) for PSR1929+10. However, the pulsar velocity and the wind Lorentz factor were 9000

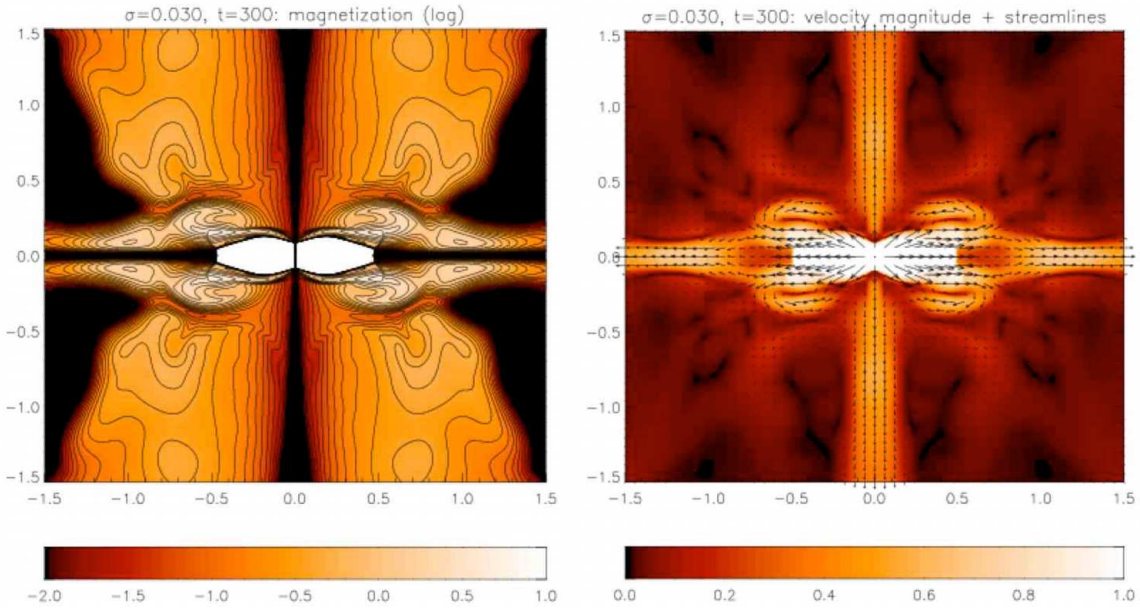

Figure 1.11: MHD simulations by Del Zanna et al. (2004) addressing the formation of the polar flow responsible for the beamed emission and the torus as observed in, e.g., the Crab. Left: the nebula magnetization. Right: the flow velocity. These simulations differ from those in Fig. 1.10 in that the pulsar is modeled more realistically as a misaligned rotator. This produces a folded current sheet in the equatorial region that is possibly able to extend to higher latitudes. This can lead to a null magnetization in this "stripped" wind region, allowing an equatorial flow to persist far from the pulsar. Bucciantini (2008) suggested this model to explain the inner-ring/outer-torus structure observed in many PWNe. Credit: Bucciantini (2008).

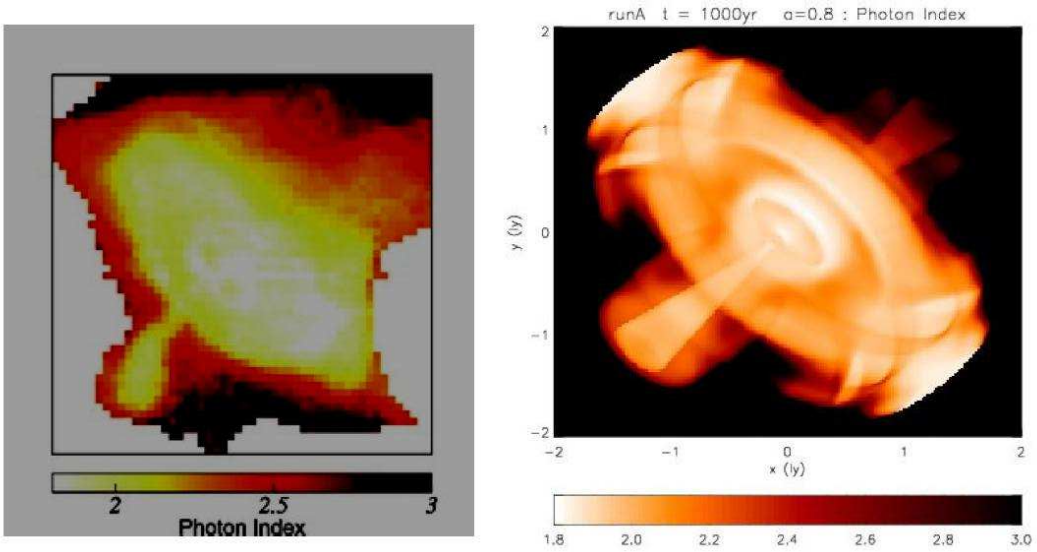

Figure 1.12: Left: a Crab nebula photon-index map from Mori et al. (2004). Right: axisymmetric simulation of the photon index (Bucciantini, 2008) showing that the major features are represented. Bucciantini (2008) further discussed the fact that simulations are not able to produce the correct jet spectrum without assuming some form of dissipation and re-energization due to heavy synchrotron losses, and posited that this might be due to toroidal magnetic field instabilities (citing Begelman, 1998) that are not captured by axisymmetric simulations. Credit: Bucciantini (2008).

km s^{-1} and 10, respectively, which are far from the typical values of 500 km s^{-1} (recall that the Guitar pulsar, the fastest known, has a transverse velocity of $\sim$1700 km s^{-1}) and 10^6. In addition, the paper does not address the "bubble" in the Guitar. Vigelius et al. (2007) performed *non*-relativistic, hydrodynamic simulations with a relaxation of cylindrical symmetry. The full 3-D FLASH code (Fryxell et al., 2000) was employed and an anisotropic pulsar wind, cooling of the shocked ISM, ISM density gradients, and ISM walls were considered. While the authors employed a realistic pulsar velocity of 400 km s^{-1}, the non-relativistic nature of the simulations limits the Lorentz factor to order unity. In Chaps. 5 & 6, I present 2D, fully-relativistic, hydrodynamic simulations for bow-shock PWNe for a realistic pulsar velocity and wind Lorentz factor both with and without wind cooling. In particular, I address the origin of relativistic backflows leading to a persistent bubble.

1.2.3 Trends for the future

While substantial recent progress has been made, there are many avenues for future improvement. As stressed by Bucciantini (2008), all (relativistic) simulations to date have been axisymmetric and observed time-variability is not well understood. The fact that the Crab exhibits non-axisymmetric time variability in the jet clearly shows that full 3-D simulations are needed. In addition, the PWN/SNR interaction has not been studied from within the context of the new models of the PWN core region discussed in the previous section. In particular, the interaction between the PWN and SNR reverse shock is 3-dimensional and complex, and current observational results (see, e.g., Chap. 2 of this work) are, for the first time, making possible a detailed probe of such crushed PWNe. Last, but not least, is the need for full-blown PWNe simulations including realistic Lorentz factors for the pulsar wind and both wind and ambient-medium cooling. I present simulations of bow-shock PWNe for wind Lorentz factors up to 10^5 in Chap. 5. Given the magnetized and ionized nature of pulsar winds, synchrotron losses are bound to have an important impact on the morphology and dynamics of PWNe. Chap. 6 of this work details the initial stages of simulations to address this issue.

CHAPTER 2

Observations of MSH 11-6*2*

In the simplified model of the demise of a massive star via a supernova explosion, the collapse of the star's core drives a shockwave into its outer layers, thereby heating and ejecting them into the ISM. Thus, the spectrum of the SNR is expected to show the thermal signatures of a high-temperature plasma.

There exists, however, a class of SNRs that does not conform to this scenario, exhibiting a non-thermal, centrally-peaked X-ray spectral component. The most well-known example is the Crab Nebula, in which the dominant X-ray emission mechanism is synchrotron radiation arising from a relativistic ion wind and magnetic field powered by the spin-down energy of the compact object, a neutron star, created in the SN explosion. The emission from this PWN is the signature of the neutron star and is the smoking gun of a Type Ib/c or Type II SN (i.e., the core collapse of a massive star). Relativistic electrons and positrons streaming along polar magnetic field lines are thought to give rise to highly beamed emission.[1] In the case of the Crab Nebula, pulsed emission has been detected at all wavelengths, confirming the nature of the compact object. However, there are many examples, including MSH 11–6*2*, in which the pulses escape detection. In such cases, X-ray analysis provides a superior method for 1) demonstrating the presence of a compact object via detection of its synchrotron nebula and 2) gathering information about the energetics of the system.

[1]There is a competing model, however, that places the origin of the high-energy emission in the outer gaps of the neutron star's magnetosphere (Cheng & Zhang, 1999); while the viability of this model remains open for debate, it currently faces serious challenges (e.g., Hui & Becker, 2007).

The *Chandra* X-ray Observatory (Weisskopf et al., 1996) ushered in a new era of X-ray analysis for objects such as PWNe with an improvement in spatial resolution of more than two orders of magnitude as compared to its predecessor, the Advanced Satellite for Cosmology and Astrophysics (ASCA, Inoue, 1993). This increase in resolution allows *Chandra* to directly image PWNe (e.g., Wang et al., 2001). The Advanced CCD Imaging Spectrometer (ACIS) aboard *Chandra* has arcsecond spatial resolution and is sensitive to X-rays in the 0.2-10.0 keV energy band with an energy resolution of 0.1 keV at 1 keV. Recent examples of *Chandra's* X-ray prowess being brought to bear on SNRs containing PWNe include: G11.2-0.3 (Roberts et al., 2003), G292.0+1.8 (Hughes et al., 2003), and G292.2-0.5 (Gonzalez & Safi-Harb, 2003) in the Galaxy and B0453-685 (Gaensler et al., 2003) in the Large Magellanic Cloud. Previous ASCA results for MSH 11–6*2* show the presence of an unresolved non-thermal source (Harrus et al., 1998) within the larger thermal SNR. In what follows, I present the results and interpretation of *Chandra* X-ray data on MSH 11–6*2* and its putative PWN. In §2.1 – §2.4, I detail the data reduction techniques and spatial and spectral analyses. In §2.5, I discuss the results.

2.1 Data Reduction

A 50 kilosecond *Chandra* ACIS-S3 observation of MSH 11–6*2* (I. M. Harrus, principle investigator) was performed on 2002 April 8 with pointing $11^{\rm h}11^{\rm m}55^{\rm s}$,-60°39′40″. Jack Hughes reduced the data following **CIAO 3.2.2** prescriptions. I employed **XSPEC v11.3** (Arnaud, 1996) to analyze spectra. The incidence of high-energy particles gives rise to the "particle background" which is manifest as 1) a spectral rise and plateau above $\sim$ 8 keV due to the direct impact of high-energy particles on ACIS, and 2) bona fide X-ray lines below $\sim$1 keV due to the fluorescence of detector hardware impacted by high-energy particles near ACIS. To protect against contamination by the particle background, I restricted the analysis energy range to 0.7-7 keV.

2.2 Spatial Analysis

Fig. 2.1 shows a MSH 11–6*2* 1.4 GHz radio image taken with the Australian Telescope Compact Array (ATCA; data courtesy Bryan Gaensler, David Moffett, and Richard Dodson). The image clearly shows the central region and overall elongated shape of the SNR. The brightening of the emission along the South-East and North-West boundaries of the SNR, but not along the South-West and North-East strongly suggests that MSH 11–6*2* is a member of the class of bilateral SNRs (Gaensler, 1998), which are also known as "barrel" (Kesteven & Caswell, 1987) or "bipolar" (Fulbright & Reynolds, 1990) SNRs. Fig. 2.2 shows the *Chandra* ACIS X-ray image of MSH 11–6*2*, the ATCA radio contours, and an overlay of the two showing that essentially the entire ACIS-S3 chip is covered by SNR emission and that the X-ray peak is located at the South-West end of the radio bar. I defined large SNR source regions (hereafter "SNR_S2" and "SNR_S3", respectively) on the S2 and S3 chips far from the hard emission region for the analysis of the SNR (see Fig. 2.3). These definitions allow an exploration of the thermal emission in two different parts of the remnant; e.g., variation in ionization timescales would indicate different ionization states.

I defined two regions for the analysis of the non-thermal emission. First, I defined a 2″-radius region containing 700 net counts centered on the X-ray peak (located at $11^{\rm h}11^{\rm m}48^{\rm s}.62$,-60°39′26″.2) to be the compact-component region ("cc" region) for analyzing the hard emission from the putative pulsar. Fig. 2.4 shows the radial profiles (I generated these using CIAO's **SHERPA** package) for the cc region and for the *Chandra* point-spread function from which I conclude that the central X-ray source is consistent with a point source. Second, I defined the nebula region ("neb" region) from the extent of the hard emission in the 2–6 keV energy range. This resulted in the elliptical region in Fig. 2.3 with radii 100″×30″ containing 5950 net counts. Using HI absorption data, collaborators Gaensler, Moffett, and Dodson determined the near-distance to MSH 11–6*2* to be ∼3.5 kpc. Using the results from an updated

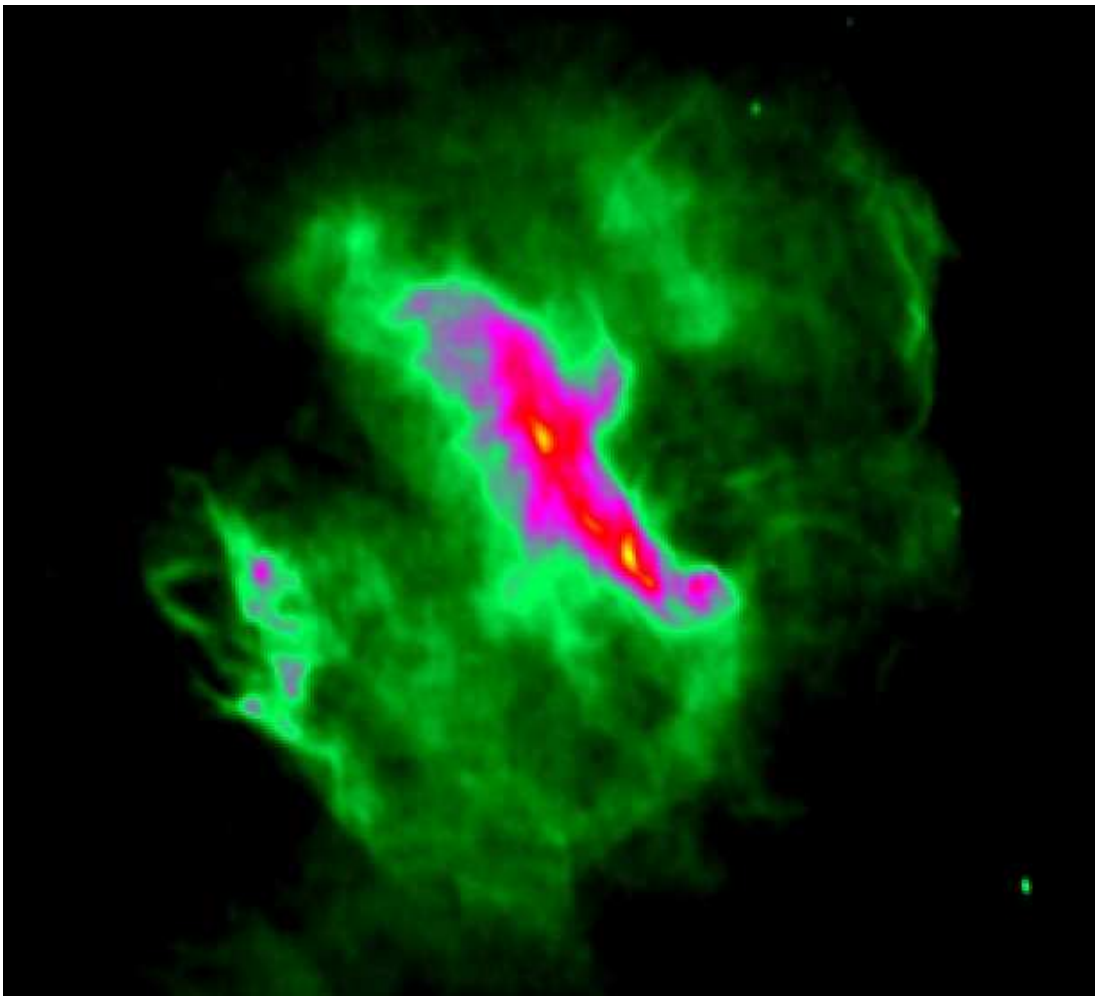

Figure 2.1: A 1.4 GHz ATCA image of MSH 11–6*2* with DS9 "A" false-color coding clearly showing the overall elongated shape of the central region of the SNR, enhanced brightening along the SE and NW boundary, and lack of boundary emission to the SW and NE. This morphology strongly suggests that MSH 11–6*2* is a member of the class of bilateral (or "barrel") SNRs (Gaensler, 1998). It is noteworthy that such SNRs are typically oriented with their symmetry axis parallel to the Galactic plane, consistent with the orientation of the Galactic magnetic field (Gaensler, 1998). However, the symmetry axis of MSH 11–6*2* is nearly perpendicular to the plane, a fact which lends itself to a dynamical interpretation of the barrel morphology, as opposed to a magnetic field argument.

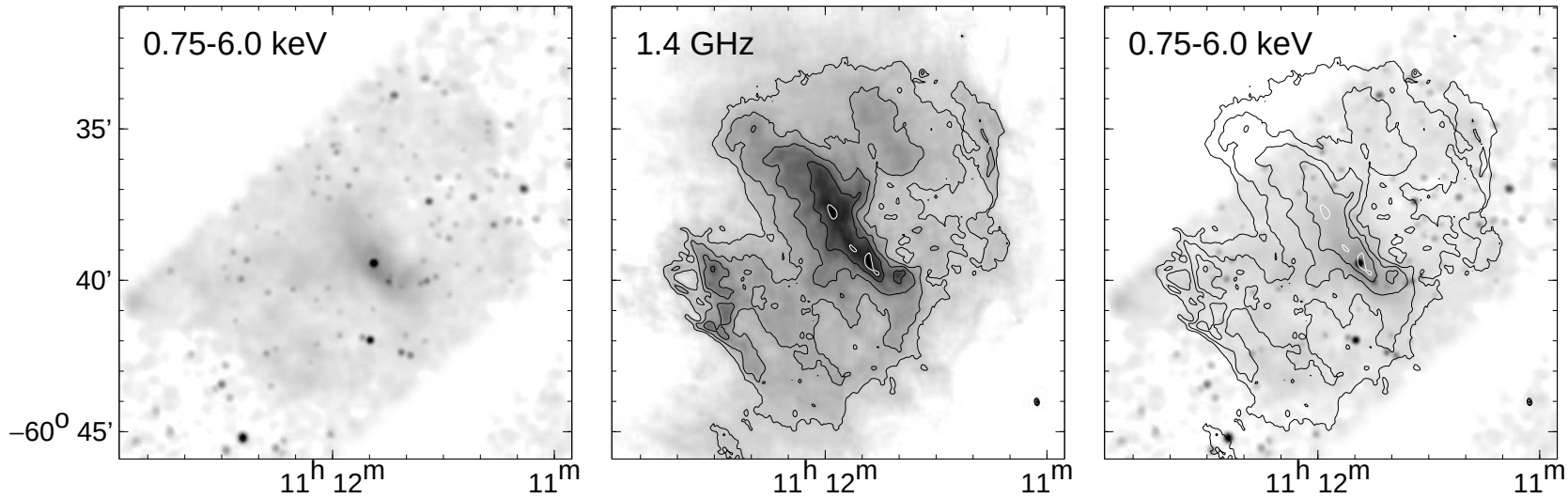

Figure 2.2: A *Chandra* ACIS X-ray image of MSH 11–6*2* (left), ATCA radio contours (center), and X-ray image with radio contours overlaid (right). Credit: Jack Hughes.

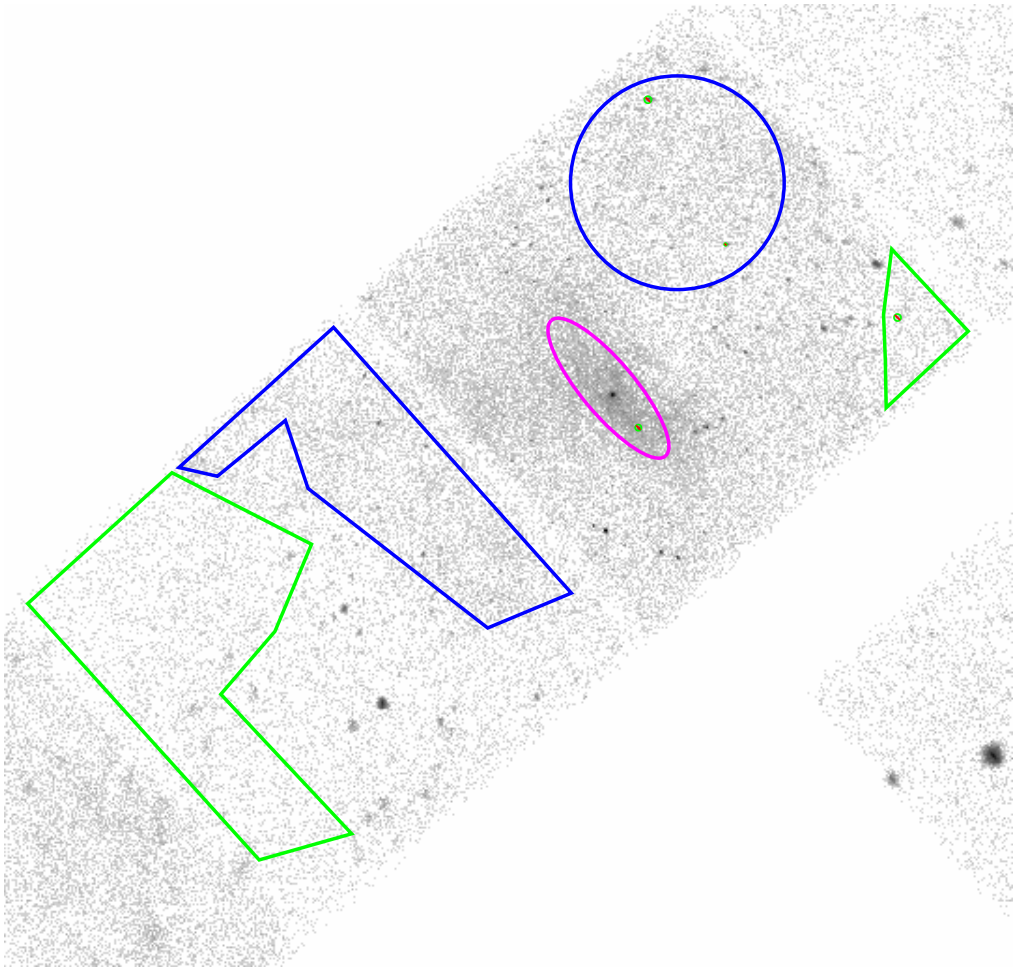

Figure 2.3: *Chandra* ACIS X-ray image with the spectral analysis regions overlaid: nebula (magenta ellipse), SNR_S2 source (blue polygon), SNR_S2 background (green polygon), SNR_S3 source (blue circle), and SNR_S3 background (green triangle). Not shown is the 2″-radius circular compact-component region centered on the X-ray peak (near the center of the nebula region) due to the scale of the image.

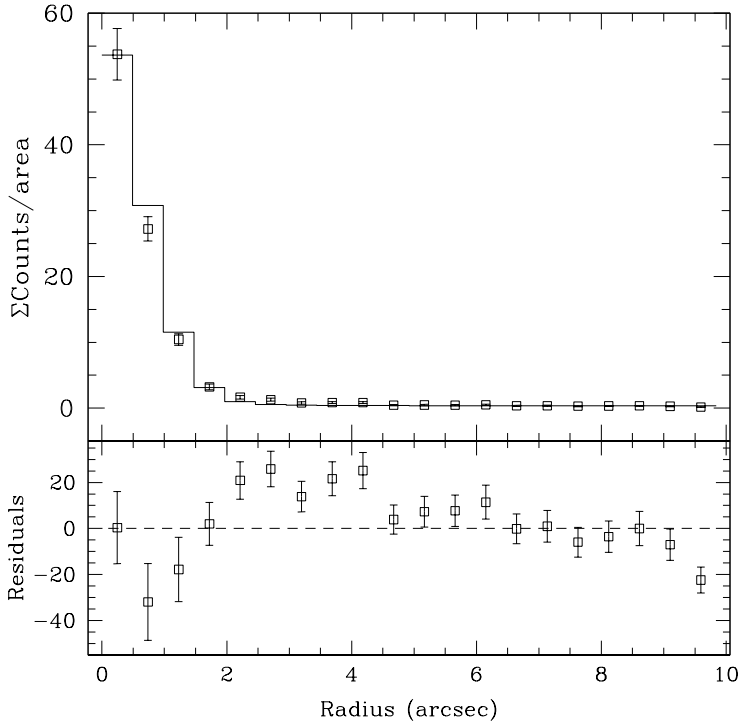

Figure 2.4: Radial profile of the MSH 11–6*2* compact component (points) and the *Chandra* point-spread function (line) showing that the central X-ray source is consistent with a point source.

statistical study of the spiral structure of the Galaxy (Vallée, 2005), I estimated that MSH 11–6*2* is located in the Carina arm with a far-distance ∼7.5 kpc (see Fig. 2.5). Thus, I adopt a distance of 5.5 kpc for MSH 11–6*2*.

Fig. 2.6 and 2.7 show three-band and "true-color" X-ray images for MSH 11–6*2* created by Jack Hughes. For the latter, red, green, and blue correspond to the 0.75-1.45, 1.45-2.6, and 2.6-6.0 keV energy bands. The low-energy contribution from the SNR is clearly visible. In agreement with the previous ASCA results (Harrus et al., 1998), this emission dominates outside the nebula region, which is clearly visible in white, along with the compact component which marks the location of the putative neutron star. A striking feature is the elongated appearance of the nebula along the same axis as the radio bar.

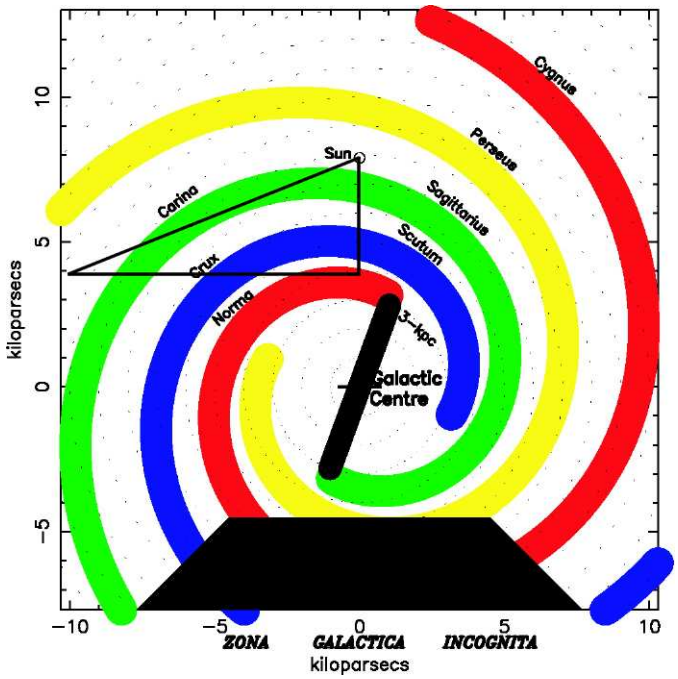

Figure 2.5: Spiral structure of the Galaxy from Vallée (2005). My overlaid triangle shows the direction to MSH 11–6*2* (hypotenuse) and suggests that the SNR is located in the Carina arm within 7.5 kpc.

2.3 Spectral Models

As mentioned previously, MSH 11–6*2* exhibits both thermal and non-thermal emission necessitating a two-component model. In this section, I discuss the models selected for analysis of MSH 11–6*2*.

2.3.1 Thermal modeling

The thermal models currently available for fitting SNR spectra cover a broad range of complexity. In general, SNR spectra cannot be fit with standard X-ray models because they are not in ionization equilibrium (e.g., Borkowski, 2000). Rather, a non-equilibrium ionization (NEI) model is required. In what follows, I discuss a simple, single-temperature, single ionization timescale model, a single-temperature plane-parallel shock model, and a Sedov model (called NEI, PSHOCK, and SEDOV, respectively, in **XSPEC**; see Borkowski et al., 2001, for a detailed discussion).

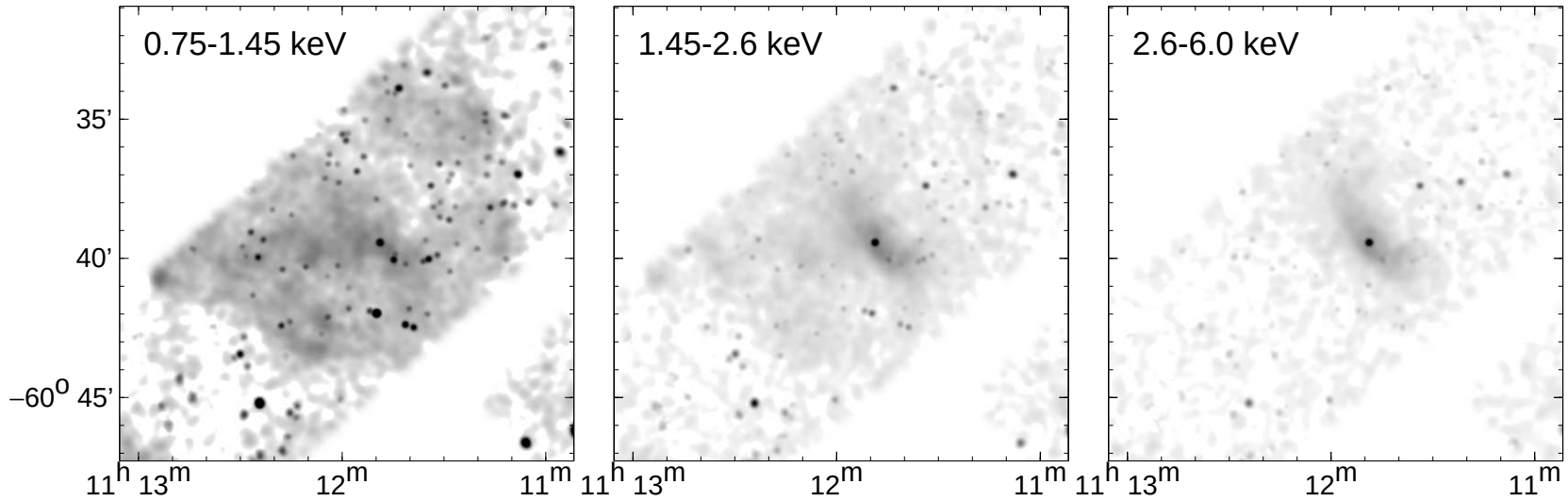

Figure 2.6: Smoothed *Chandra* ACIS X-ray images of MSH 11–6*2* in, from left to right, the 0.75-1.45 keV, 1.45-2.6 keV, and 2.6-6.0 keV energy bands. Credit: Jack Hughes.

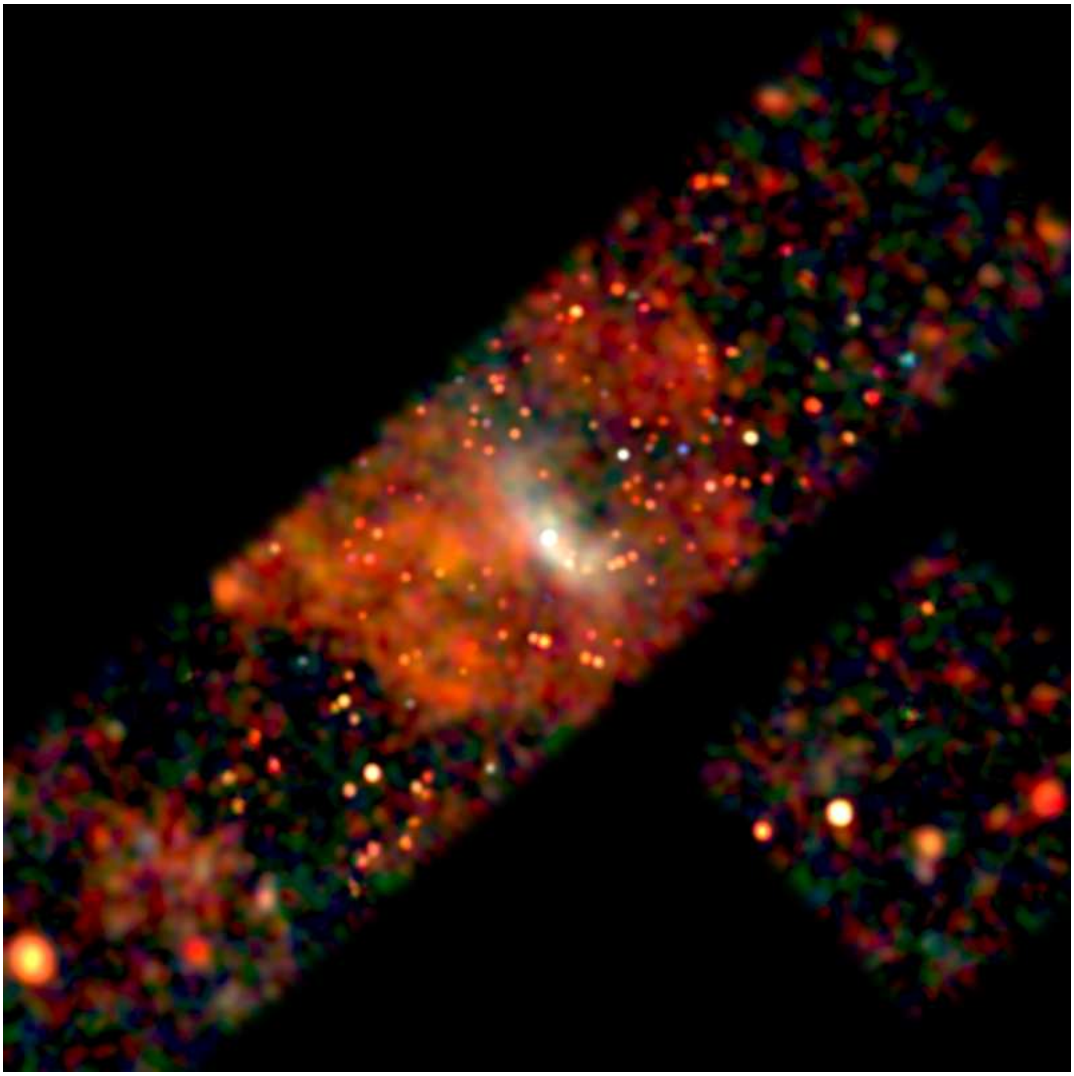

Figure 2.7: *Chandra* ACIS X-ray true-color image of MSH 11–6*2*. The diffuse emission and point sources for the 0.75-1.45 keV, 1.45-2.6 keV, and 2.6-6.0 keV energy bands were smoothed with separate Gaussians and recombined. Credit: Jack Hughes.

The NEI model assumes an impulsively heated, uniform gas with the following parameters:

- kT = the plasma temperature in keV.
- abund = Metal abundances (He cosmic value): C, N, O, Ne, Mg, Si, S, Ar, Ca, Fe, Ni using the Anders & Grevesse mixtures.
- τ = Ionization timescale $\equiv n_e t$ in s cm^{-3} (n_e = electron density, t = shock age).
- z = redshift (fixed to 0 for this work).
- $\mathrm{N_T} = \frac{10^{-14}}{4\pi(\mathrm{D_A}*(1+\mathrm{z}))^2} \int n_e n_H dV$ where $\mathrm{D_A}$ is the angular size distance to the source (cm) and n_H is the hydrogen density (cm^{-3}).

This model is not physical; rather, it characterizes the spectrum. It approximates the ionization distribution versus emission measure as a delta function leading to significant error in fitting SNR spectra in most cases (Borkowski et al., 2001, and references therein).

The PSHOCK model assumes a plane-parallel shock with a constant post-shock temperature, but offers an improvement over the NEI model as it includes a linear distribution of ionization timescales. The parameters are as follows:

- kT = the plasma temperature in keV.
- abund = Metal abundances (He cosmic value): C, N, O, Ne, Mg, Si, S, Ar, Ca, Fe, Ni using the Anders & Grevesse mixtures.
- τ_{l} = Lower limit on ionization timescales in s cm^{-3}.
- τ_{u} = Upper limit on ionization timescales in s cm^{-3}.
- z = redshift (fixed to 0 for this work).
- $\mathrm{N_T} = \frac{10^{-14}}{4\pi(\mathrm{D_A}*(1+\mathrm{z}))^2} \int n_e n_H dV$.

The admission of varying τ results in a much better approximation to SNR spectra, but still leaves much to be desired, particularly at lower energies (Borkowski et al., 2001).

The SEDOV model assumes a spherical blastwave governed by Sedov dynam-

ics with Coulomb and collisionless electron heating. This model provides the most realistic approximation to SNR spectra as it includes separate ion and electron temperatures in addition to a range in τ:

- kT_a = mean shock temperature in keV.
- kT_b = electron temperature immediately behind the shock front in keV.
- abund = Metal abundances (He cosmic value): C, N, O, Ne, Mg, Si, S, Ar, Ca, Fe, Ni using the Anders & Grevesse mixtures.
- τ_l = Lower limit on ionization timescales in s cm^{-3}.
- τ_u = Upper limit on ionization timescales in s cm^{-3}.
- z = redshift (fixed to 0 for this work).
- $N_T = \frac{10^{-14}}{4\pi(D_A*(1+z))^2} \int n_e n_H dV$.

This is the model for routine use in fitting SNR spectra (Borkowski, 2000). It is noteworthy that this model is computationally intensive and requires extended time to obtain fits.

2.3.2 Non-thermal modeling

As previously mentioned, the model for the non-thermal emission in SNRs such as the Crab is synchrotron emission arising from the gyration of charged wind particles in the nebular magnetic field. It is well known that the ensemble spectrum from a broad population of synchrotron emitting particles is a simple power-law. Thus, I selected the **XSPEC** model POWERLAW to analyze the non-thermal emission in MSH 11–6*2* with the following parameters:

- Γ = dimensionless photon index.
- N_Γ = photons keV^{-1} cm^{-2} s^{-1} at 1 keV.

2.3.3 Modeling absorption

I opted for the Tuebingen-Boulder ISM absorption model (TBABS **XSPEC** model) to account for absorption along the line of site to MSH 11–6*2*. The sole parameter

is the equivalent hydrogen column, N_H, in units of 10^{22} atoms cm^{-2}. I selected this model because it calculates the ISM X-ray absorption cross-section via the summation of the cross-sections due to gas, grains, and molecules. Shielding by the grains is accounted for while only molecular hydrogen is considered. The gas cross-section is the abundance-weighted sum of the elements' photoionization cross-sections including grain depletion and updated ISM abundances (see Wilms et al., 2000).

2.4 Spectral Analysis

I used the **XSPEC** models NEI, PSHOCK, and SEDOV to elucidate the thermal nature of MSH 11–6*2* using the SNR regions defined above. Fitting a thermal model to the nebula region required a temperature of 13 keV, more than an order of magnitude too high for a thermal SNR. Thus, I used the **XSPEC** model POWERLAW to probe the spectral nature of the inner regions of MSH 11–6*2* because, if they are indeed powered by a pulsar, the high energy spectrum can be approximated by a simple power-law resulting from the synchrotron emission mechanism. I accounted for absorption by employing the **XSPEC** model TBABS.

While the PWN emission contributes the non-thermal component, if present, in a SNR, I expected the spectra for the SNR regions to be thermal and modeled it as TBABS×NEI, TBABS×PSHOCK, and TBABS×SEDOV. The salient parameters of these combined models are N_H (frozen to the value from the nebula fit; see below), the plasma temperature, the ionization age, τ, and normalization, N_T. Fig. 2.8 and Table 2.1 show the spectra and fit parameters, respectively. In particular, the lower ionization timescale for the SNR_S3 region, at a few times 10^{10} to 10^{11} s cm^{-3}, as compared to SNR_S2 suggests that the former is further from ionization equilibrium.

I fit the **XSPEC** model TBABS×POWERLAW to the compact and nebula region spectra (see Fig. 2.9 and Table 2.2) using the SNR_S3 region spectrum as background with hydrogen column frozen to the value from the nebula fit (see below). I divided

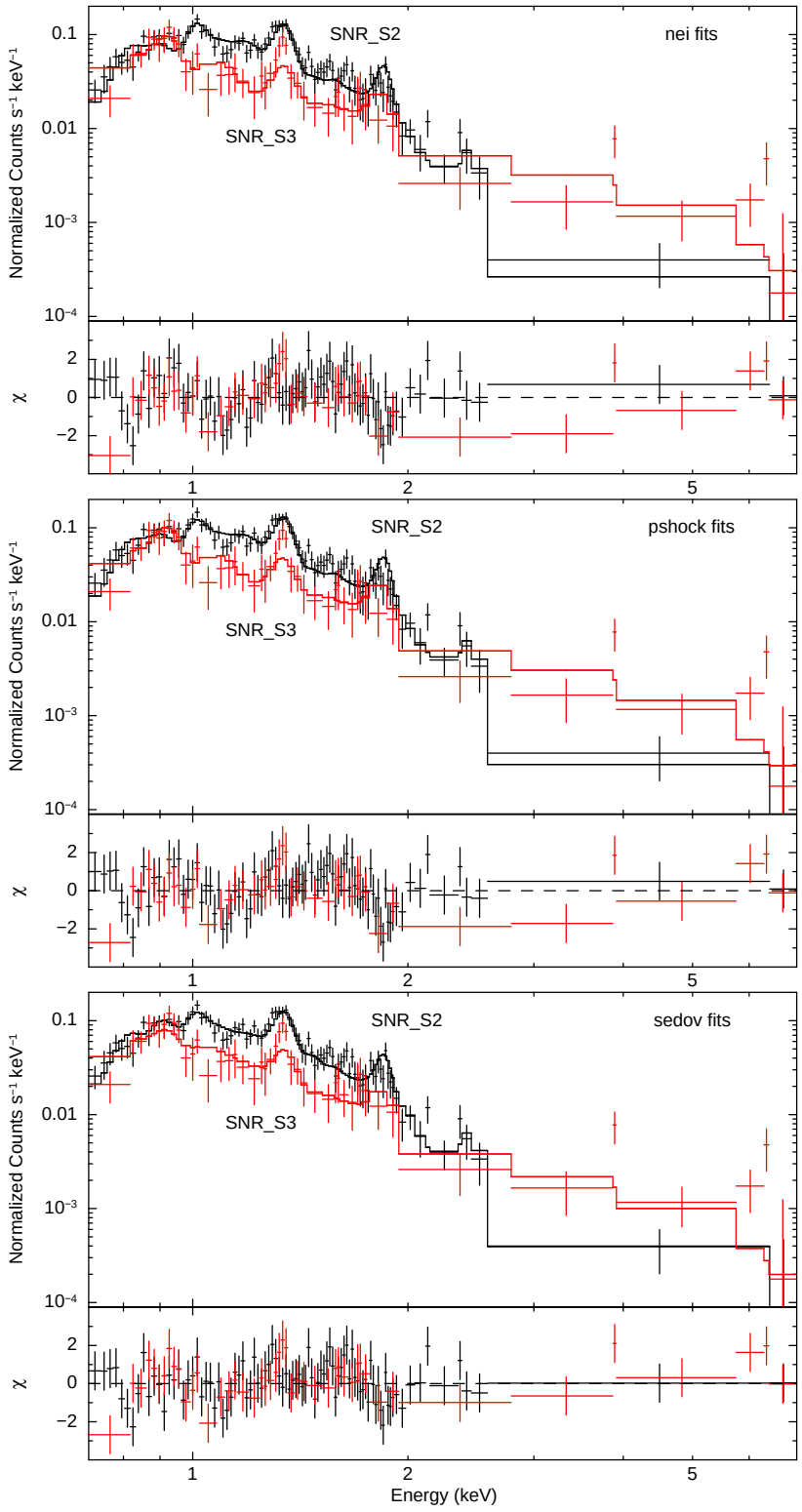

Figure 2.8: *Chandra* ACIS X-ray thermal spectra for the SNR_S2 (black) and SNR_S3 (red) regions. The top, middle, and bottom panels are for the NEI, PSHOCK, SEDOV models, respectively.

Table 2.1: *Chandra* thermal spectral fit parameters for MSH 11–6*2*. The column density was fixed to the value from the non-thermal fit. The fit parameters show non-trivial variation between the two regions. In particular, the ionization timescales suggest that different parts of the remnant are in different ionization states. For this reason, I take the range of pressures implied by the fits for the pressure-balance calculations in §2.5. The lower temperatures for the SEDOV model are to be expected since it is a multi-temperature model and, thus, it can fit the same data as the other two models with lower temperatures. Note that the S2 and S3 regions were fit simultaneously for each model.

Region	Model	N_H	kT	τ	N_T	χ^2_ν	*dof*
	(10^{22} cm^{-2})	(keV)	(10^{10} s cm^{-3})	(10^{-5})	(10^{-5})		
S2	NEI	1.06 (fixed)	$0.50^{+0.03}_{-0.06}$	30^{+60}_{-9}	270^{+100}_{-40}	1.1	299
	PSHOCK*	1.06 (fixed)	$0.54^{+0.04}_{-0.05}$	60^{+330}_{-19}	250^{+950}_{-35}	1.1	300
	SEDOV$^\diamondsuit$	1.06 (fixed)	$0.37^{+0.05}_{-0.02}$	49^{+27}_{-15}	350^{+110}_{-74}	1.0	300
S3†	NEI	1.06 (fixed)	$0.35^{+0.12}_{-0.10}$	$1.7^{+4.2}_{-0.7}$	380^{+580}_{-210}	1.1	299
	PSHOCK*	1.06 (fixed)	$0.33^{+0.08}_{-0.08}$	$2.9^{+2.4}_{-2.1}$	580^{+910}_{-350}	1.1	300
	SEDOV$^\diamondsuit$	1.06 (fixed)	$0.16^{+0.06}_{-0.04}$	17^{+16}_{-17}	1200^{+3400}_{-800}	1.0	300

$\dagger$: $\Gamma = 1.8$ power-law added with fitted norms $8.3^{+1.6}_{-2.2}$ (NEI), $7.9^{+2.1}_{-1.8}$ (PSHOCK), $5.3^{+1.9}_{-1.9}$ (SEDOV)

$\star$: quoted τ is τ_u; τ_l was fixed at 0

$\diamondsuit$: quoted kT is the fit with the shock and electron temperatures linked

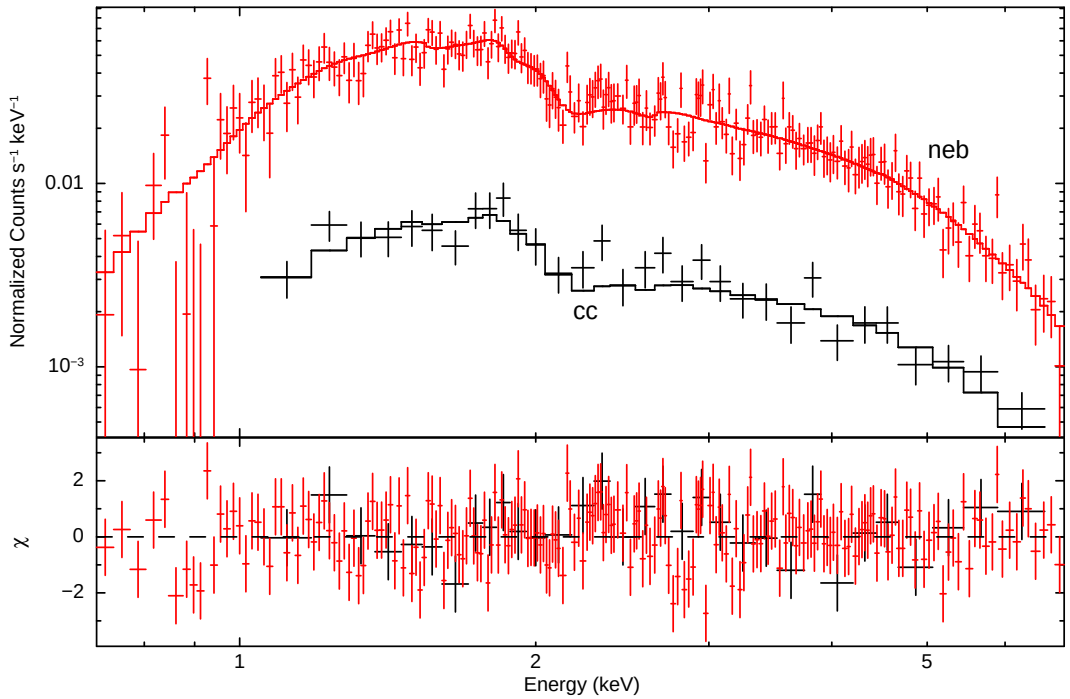

Figure 2.9: *Chandra* ACIS X-ray compact component (black) and nebula (red) spectra with absorbed power-law fit.

the nebula region into 20″ and 15″-wide slices (the "non-thermal sequence") along the long and short axes, i.e., "NE-SW" and "SE-NW", respectively, with overlapping slices at the position of the compact component. I linked the value of N_H for the slices (in order to obtain a global fit of $1.06^{+0.08}_{-0.07}\times10^{22}$ cm^{-2}) and let the power-law spectral indexes and normalizations vary freely, again using the SNR_S3 region for background. Fig. 2.10 shows the variation of the spectral index of the hard emission with increasing distance from the compact component once again showing that the hard emission is asymmetric. The spectral index increases with distance, consistent with the expected shorter synchrotron lifetime of the higher energy emitting particles.

2.5 Discussion

As mentioned above, no pulses have been detected from MSH 11–6*2*. I employed the results of the X-ray analysis to infer properties of the supposed neutron star and its synchrotron nebula. Using the model fit, I calculated the unabsorbed X-ray fluxes

Table 2.2: *Chandra* non-thermal spectral fit parameters for MSH 11–6*2*. For the compact-component and nebula regions, the data were fit jointly with the spectral index and normalization free to vary for each data set and the column density was fixed to the global fit value for the non-thermal sequence. For the sequence itself, the data were fit jointly with all parameters free. The regions numbered "0" and "6" represent the box covering the compact component and those farthest from it, respectively. "NE-SW" and "SE-NW" denote which nebula axis is being sampled and the single ordinates, e.g. "NE" denote which direction the box is displaced from the center.

Region	N_H (10^{22} cm^{-2})	Γ	N_Γ (10^{-5})	χ^2_ν	*dof*
compact	1.06 (fixed)	$1.51^{+0.14}_{-0.13}$	$4.24^{+0.79}_{-0.54}$	0.9	248
nebula	1.06 (fixed)	$1.78^{+0.05}_{-0.05}$	$42.7^{+2.4}_{-2.4}$	0.9	248
non-thermal sequence					
0NE-SW	$1.06^{+0.08}_{-0.07}$	$1.52^{+0.11}_{-0.09}$	$11.9^{+1.71}_{-2.1}$	1.0	665
1NE	*	$1.86^{+0.17}_{-0.14}$	$6.81^{+1.29}_{-0.88}$	*	*
2NE	*	$1.97^{+0.20}_{-0.15}$	$5.22^{+1.13}_{-1.44}$	*	*
3NE	*	$1.65^{+0.24}_{-0.21}$	$3.04^{+0.81}_{-0.29}$	*	*
4NE	*	$2.03^{+0.25}_{-0.13}$	$3.38^{+0.90}_{-0.63}$	*	*
5NE	*	$2.40^{+0.32}_{-0.28}$	$4.18^{+1.25}_{-0.94}$	*	*
6NE	*	$2.22^{+0.38}_{-0.18}$	$2.65^{+0.97}_{-0.72}$	*	*
1SW	*	$1.85^{+0.17}_{-0.15}$	$7.13^{+1.34}_{-0.93}$	*	*
2SW	*	$1.88^{+0.18}_{-0.16}$	$5.98^{+1.21}_{-0.95}$	*	*
3SW	*	$1.96^{+0.20}_{-0.09}$	$5.83^{+1.23}_{-0.96}$	*	*
4SW	*	$2.06^{+0.25}_{-0.22}$	$4.09^{+1.06}_{-0.82}$	*	*
5SW	*	$1.78^{+0.41}_{-0.37}$	$1.95^{+0.82}_{-0.62}$	*	*
6SW	*	$2.97^{+0.64}_{-0.52}$	$2.87^{+1.41}_{-1.02}$	*	*
0SE-NW	*	$1.58^{+0.12}_{-0.10}$	$12.0^{+1.76}_{-1.34}$	*	*
1SE	*	$1.67^{+0.17}_{-0.08}$	$5.74^{+1.12}_{-0.89}$	*	*
2SE	*	$2.20^{+0.38}_{-0.33}$	$2.96^{+1.04}_{-0.77}$	*	*
3SE	*	$3.64^{+1.00}_{-0.76}$	$4.55^{+1.48}_{-1.73}$	*	*
4SE	*	$3.41^{+0.53}_{-0.66}$	$3.01^{+1.69}_{-1.14}$	*	*
1NW	*	$1.82^{+0.17}_{-0.15}$	$6.25^{+1.18}_{-0.82}$	*	*
2NW	*	$1.73^{+0.24}_{-0.22}$	$2.82^{+0.78}_{-0.48}$	*	*
3NW	*	$1.86^{+0.19}_{-0.33}$	$1.55^{+0.63}_{-0.49}$	*	*
4NW	*	$1.78^{+0.53}_{-0.23}$	$0.83^{+0.51}_{-0.38}$	*	*

*: simultaneous fit

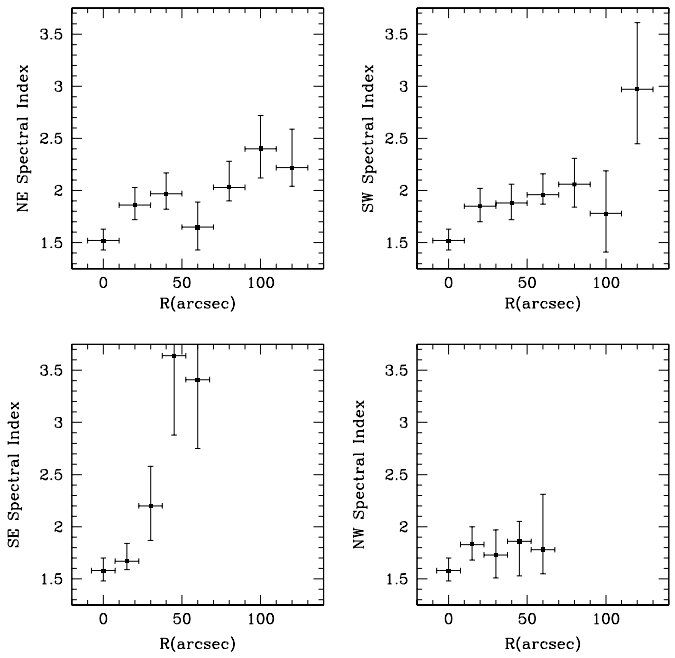

Figure 2.10: Spectral indices from the nebula non-thermal sequence showing the variation with increasing distance from the compact component (located at "0 arcsec" in all four plots).

(see Table 2.3). Assuming a distance of 5.5 kpc, I used the 2.0-10.0 keV flux to calculate the non-thermal X-ray luminosity for the compact component and nebula: $L_{X,cc} = 8.7^{+3.9}_{-2.7}\times10^{32}$ erg s^{-1}, and $L_{X,neb} = 55.0^{+8.0}_{-7.2}\times10^{32}$ erg s^{-1}, respectively. I make use of three empirical relationships relating the spin-down luminosity of the putative neutron star, $\dot{E}$, to observable properties of the non-thermal emission (Becker & Truemper, 1997; Possenti et al., 2002; Gotthelf, 2003):

$$log(L_{X,0.1\text{–}2.4}) = -3 + log(\dot{E}), \quad (2.1)$$

$$log(L_{X,2\text{–}10}) = -14.36 + 1.34log(\dot{E}), \quad (2.2)$$

$$\Gamma_{PSR} = 2.08 - 0.029(\dot{E}/10^{40} ergs^{-1}), \quad (2.3)$$

where I took Γ_{PSR} to be Γ_{cc}, and "0.1–2.4" (note for the *Chandra* flux, I used 0.2–2.4) and "2–10" refer to the energy band in keV. These three relations give estimates for $\dot{E}$ of 6×10^{36}, 8×10^{35}, 3×10^{37} erg s^{-1} , respectively. While these values are rough

Table 2.3: Unabsorbed non-thermal model X-ray fluxes for MSH 11–6*2*.

Region	Energy Band (keV)	Unabsorbed Flux (10^{-13} erg cm^{-2} s^{-1})
compact		
	0.2-2.4	$1.5^{+0.3}_{-0.2}$
	0.2-4.0	$2.1^{+0.5}_{-0.3}$
	2.0-10	$2.4^{+1.1}_{-0.7}$
nebula		
	0.2-2.4	$15.9^{+1.2}_{-1.1}$
	2.0-10	$15.4^{+2.2}_{-2.0}$

estimates only, they are all strongly supportive of rotation-powered emission.

The apparent asymmetry of the hard emission and the structure of the SNR boundary suggest that the nebula is being (or has been) crushed by the reverse shock of the SNR. The presence of two bright limbs opposite from each other suggest that MSH 11–6*2* is a member of the class of bilateral (also called "barrel") SNRs, or "BSNRs" (Gaensler, 1998). In order to investigate this possibility, I assess the pressures within the SNR as, if this is the case, pressure balance between the SNR and the nebula is expected (see §1.1.2). I begin by writing down the pressure inside the SNR:

$$P_{\rm SNR} = \sum_i P_i \approx 1.85 n_{\rm e} k T_{\rm e}, \tag{2.4}$$

where the index i is over the particle species present in the SNR, $n_{\rm e}$ and $T_{\rm e}$ are the electron density and temperature, respectively, and I have assumed solar abundances. The fit electron temperature and normalization allow an estimation of the electron density in MSH 11–6*2* as an average of the values for all three thermal models for both the SNR_S2 and SNR_S3 regions: $n_{\rm e} \approx 5.6^{+7.9}_{-1.8} \times 10^{-1}\ f^{-1/2}$ cm^{-3}, where I have approximated the product of the electron and hydrogen densities to be the product of their average values multiplied by a filling factor f (generally categorized as "unknown" in the literature, though there are examples of quoted values on the

order of a few tenths, e.g., Jackson et al., 2008). This is consistent with the value reported by Harrus et al. (1998). This allows the calculation of the SNR pressure via Eqn. 2.4. The average value for both SNR regions and all three models is:

$$P_{\rm SNR} \approx 5.8^{+8.0}_{-1.8} \times 10^{-10} f^{-1/2} \text{ erg cm}^{-3}. \tag{2.5}$$

Next, I calculate the pressure inside the nebula assuming pressure balance of the SNR and a pulsar wind (Rees & Gunn, 1974):

$$P_{\rm bal} = \frac{\dot{E}}{4\pi r_{\rm ts}^2 c} \tag{2.6}$$

where $r_{\rm ts}$ is the radius of the wind termination shock and c is the speed of light. As Fig. 2.4 shows a smooth fall-off, I can only assume a lower limit on the angular radius of the termination shock $\theta_{\rm ts} < 2''$ ($r_{\rm ts} < 0.05$ pc at 5.5 kpc). Thus, using the estimates of the spin-down luminosity above, I obtain a range for the lower limit of the nebula pressure of $8{\times}10^{-11}$ – $3{\times}10^{-9}$ cgs. This range is consistent with the range of pressures for the SNR supporting the interpretation that the synchrotron nebula has been crushed by the reverse shock of the SNR. The asymmetry of the nebula can be explained by a non-uniform distribution of the local ambient medium. Suppose that MSH 11–6*2* is evolving inside an elongated cavity of lower density with its long axis oriented parallel to the symmetry axis of the remnant, as is the case for G320.4-1.2, a bilateral SNR harboring an X-ray pulsar that Dubner et al. (2002) concluded had a morphology influenced by the local ISM. In this case, the boundary shock would reach the walls first in the direction perpendicular to the symmetry axis, more material would be swept up along those directions causing those limbs to brighten earlier, and the reverse shock would detach sooner and propagate back to the synchrotron nebula resulting in an asymmetric crushing event. Assuming an ISM number density of 1 cm^{-3}, a 9:1 number ratio of hydrogen to helium, a distance of 5.5 kpc, and a spherical blastwave geometry, the ∼8 arcmin radio extent of MSH 11–6*2* implies ∼35 solar masses have been swept up. Such a mass is more than sufficient for

the reverse shock to have detached (e.g., Heger et al., 2003). In total, this scenario would provide additional affirmation for the dynamical model for some bilateral SNRs invoked by Gaensler (1998).

There are other possible models to explain the features of MSH 11–6*2*. A competing model for bilateral SNRs ascribes the morphology to the Galactic magnetic field geometry (e.g., Gaensler, 1998). In this scenario, the SNR is oriented with the symmetry axis parallel to the Galactic plane, which is in stark contrast to the case of MSH 11–6*2*. Orlando et al. (2007) show via 3D MHD simulations that a gradient in the local magnetic field or ISM density that increases in the direction opposite to the direction of the global magnetic field could produce a radio map similar to that for MSH 11–6*2* (see panels C & D of Fig. 2.11). However, these scenarios would require an additional explanation of the morphology of the putative PWN. Bilateral SNRs have been observed with an orientation of the symmetry axis similar to MSH 11–6*2* (e.g., Gaensler, 1998, and references therein), suggesting two classes of barrel SNRs exist: those that are magnetically produced and those that are dynamically produced. Orlando et al. (2007) preferred a magnetic origin for bilateral SNRs, but noted that they can result from variations in the local magnetic field or ISM density. The preference for a magnetic field origin is consistent with the fact that bilateral SNRs with symmetry axes highly inclined to the galactic plane are relatively rare (e.g., Gaensler, 1998).

There are still other possible scenarios. Willingale et al. (1996) suggests that the brightened NE and SW limbs seen in the remnant of SN 1006 are due to relativistic electrons beamed from an unseen central compact object. While this model remains a possibility for SN 1006 (e.g., Dyer et al., 2004), it is unlikely that such an explanation applies to MSH 11–6*2* as the position of the presumed pulsar is not on a line connecting the brightened limb regions. In addition, this scenario would require further explanation of the asymmetry of the synchrotron nebula. Another possible

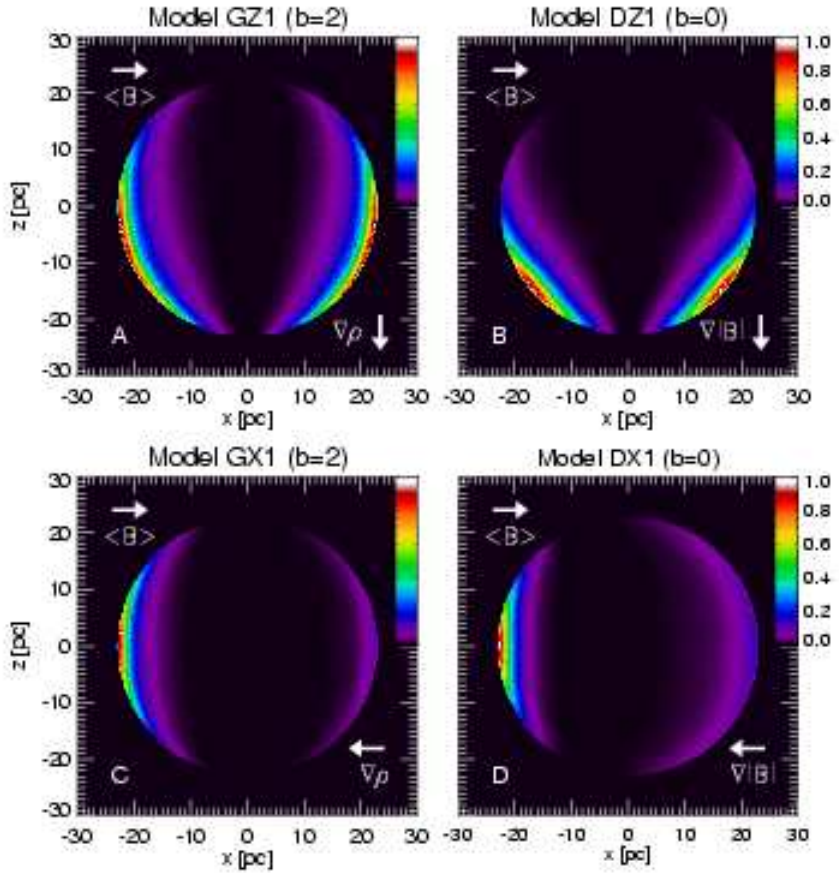

Figure 2.11: Synthesized synchrotron radio maps from 3D MHD simulations of bilateral SNRs by Orlando et al. (2007). Panels C& D are relevant to alternate scenarios discussed for MSH 11–6*2*. Credit: Orlando et al. (2007).

interpretation is that the geometry of the nebula is due to a bow-shock morphology oriented such that the pulsar is moving along the line of sight. This is problematic for two reasons. First, the displacement of the compact object from the peak of the radio emission implies a velocity vector largely perpendicular to the line of sight, which is inconsistent with the observed position of the compact object in the center of the X-ray nebula (see Fig. 1.5) in the context of a bow-shock interpretation. Second, simulations have shown that, in general, for a pulsar within a SNR (as is the case here), the space velocity of the pulsar is subsonic with respect to the SNR sound speed until the pulsar is 2/3 of the way to the edge of the remnant (van der Swaluw et al., 2004). The displacement of the compact object from the center of the radio remnant is not consistent with this picture given the extent of the remnant. Another argument could be made based on the fact, as previously discussed, that the magnetic field geometry of pulsars is toroidal, leading to elliptical PWN. However, such a scenario would have difficulty explaining the 3:1 aspect ratio of the PWN in MSH 11–6*2* given typical ellipticity of PWNe (see Figs. 1.1, & 1.8, & 1.9). In addition, both of these last two scenarios would require an additional argument to explain the barrel morphology of the remnant.

Via spectral and spatial analysis, I have constructed a strong and consistent case for the existence of a pulsar in MSH 11–6*2*. This leaves the question of why pulses are not detected. The most obvious cause is the viewing angle. The pulsed emisan SNRsion from energetic, young neutron stars is highly beamed and MSH 11–6*2* might simply be a case of a SNR harboring a pulsar whose beams do not sweep across the Earth (e.g., Brazier & Johnston, 1999). In fact, the Pulsar Wind Nebula Catalog (Roberts, 2004) lists MSH 11–6*2* as one of approximately 43% of PWNe (24 of 56) for which no pulsar has been detected.

2.6 Summary

I have presented the results of a *Chandra* analysis of the SNR MSH 11–6*2* which was previously shown to be a composite remnant with an unresolved synchrotron component. While MSH 11–6*2* exhibits this non-thermal spectral component, and thus breaks with the typical scenario of a thermal SNR formed out of the core-collapse of a massive star, it shows no evidence of the pulses that are the direct signature of the pulsar expected to be the engine driving the synchrotron emission. The current analysis provides overwhelming evidence for the presence of a compact object and the absence of pulses may be readily explained by a misalignment of our line of sight and the beamed emission responsible for pulsations.

The superior capabilities of *Chandra* as compared to ASCA located the compact component to within $\sim 2''$. From the spectral fit to the nebula emission, I inferred a spin-down luminosity for the putative pulsar that is consistent with the scenario of a rotationally powered PWN. I have tightly constrained the spatial extent of the synchrotron nebula and its spectral properties. The ACTA radio image of the SNR strongly suggests that MSH 11–6*2* is a so-called "barrel SNR" and shows a striking asymmetry in the non-thermal nebula, which is roughly elliptical with a 3:1 aspect ratio and a long axis that is nearly perpendicular to the galactic plane. The asymmetry is mirrored in the X-ray images and the SNR and nebula are consistent with being in pressure balance, strongly supporting an argument for the interpretation that the SNR reverse shock has asymmetrically crushed the synchrotron nebula. I discussed numerous other possible arguments and showed that all have noticeable deficiencies. Thus, MSH 11–6*2* provides evidence that, in this case, the density of the ISM has had a clear dynamical effect on the morphology of the SNR and its PWN. In the chapters that follow, I further explore the dynamical effect of the ISM in the context of bow-shock PWNe via simulations produced with a fully-relativistic, hydrodynamic code of an ultra-relativistic pulsar wind interacting with a slow, dense ambient flow.

CHAPTER 3

A Relativistic, Hydrodynamic Code

Hydrodynamic simulations have been widely used to model a broad range of physical systems. When the velocities involved are a small fraction of the speed of light and gravity is weak, the classical Newtonian approximation to the equations of motion may be used. However, these two conditions are violated for a host of interesting scenarios, including, for example, heavy ion collision systems (Hirano, 2004), relativistic laser systems (Delettrez et al., 2005), and many from astrophysics (Ibanez, 2003, and references therein), that call for a fully relativistic, hydrodynamic (RHD) treatment. The methods of solution of classical hydrodynamic problems have been successfully adapted to those of a RHD nature, albeit giving rise to significant complications; in particular, the physical quantities of a hydrodynamic flow (the rest-frame mass density, n, pressure, p, and velocity, v) are coupled to the conserved quantities (the laboratory-frame mass density, R, momentum density, M, and energy density, E) via the Lorentz transformation. Modern RHD codes typically evolve the conserved quantities necessitating the recovery of the physical quantities (often referred to as the "primitive variables") from the conserved quantities in order to obtain the flow velocity. Thus, the calculation of the primitives from the conserved variables has become a critical element of modern RHD codes (Martí & Müller, 2003).

I present the application of an existing adaptive-mesh, axisymmetric, RHLLE (the **r**elativistic extension by Schneider et al., 1993, of the solver introduced by **H**arten, **L**ax, van **L**eer, 1983, and refined by **E**infeldt, 1988) hydrodynamic code to the sim-

ulation of a light, fast pulsar wind interacting with a slow, dense ambient medium. Duncan & Hughes (1994) & Hughes et al. (2002) extensively used the code to simulate galactic jets, in both 2D and 3D, with Lorentz factors ($\gamma \equiv (1 - v^2)^{-1/2}$, where v is the bulk flow velocity normalized to the speed of light) up to 50. The code was validated via the comparison of relativistic shock-tube simulations to the analytical solutions of Thompson (1986). Admitting flows with such ultra-relativistic Lorentz factors as 10^6 required significant refinement to the method used to calculate the flow velocity from the conserved quantities. In particular, such extreme Lorentz factors lead to severe numerical problems such as effectively dividing by zero and subtractive cancellation. In Chap. 4, I elucidate the details of the refinement and present the refined primitives algorithm (see §4.1 & §4.2).

In the following sections, I delve further into the 2-D RHLLE method and adaptive mesh refinement (AMR), and continue with a discussion of two modifications to the code necessitated by the application to pulsar winds. First, I present the initial and boundary conditions necessary for simulating a spherical pulsar outflow streaming into a cross-flowing ambient medium. Second, I preview the refinement to the hydrodynamic solver necessitated by the ultra-relativistic nature of the pulsar wind. At the conclusion of this chapter, I discuss the formalism of recovering the primitive variables from the conserved quantities, within the context of the Euler equations, representing special relativistic, hydrodynamic (SRHD) flows.

3.1 The 2-D RHLLE Scheme

The code employs the RHLLE solver introduced by Schneider et al. (1993) as the relativistic extension of the HLLE method (Harten et al., 1983; Einfeldt, 1988). Motivation for this extension involved admitting heavy ion collisions with energies greater than 100 GeV ($\gamma \sim 10$). For collisions below this energy, experimental results were well reproduced by the hydrodynamic model of Graebner (1985). However, diffi-

culties such as violations of the relativistic conditions $R, M \leq E$ and $v < 1$ arose upon taking $\gamma \geq 10$. Schneider et al. (1993) note that, while Norman & Winkler (1986) contended that a fully implicit treatment is required to obtain a consistent solution to the relativistic, hydrodynamic equations for large Lorentz factors[1], and that adaptive, co-moving meshes should be used to combat numerical diffusion, this combination was too computationally expensive to be practical. This provided the motivation to consider explicit schemes, such as HLLE.

The HLLE method is a Godunov-type scheme (Godunov, 1959) for systems of conservation laws. In Godunov's original scheme, the conservative variables are considered to be piecewise-constant over a mesh of computational cells, and time evolution is calculated by finding either the exact or approximate solution to the local Riemann problem at the cell boundaries. The discontinuities that initially separate the constant states break down leading to rarefaction waves or shockwaves. The numerical fluxes of the conserved variables that form the basis of the technique depend explicitly on the maximum and minimum wave (or signal) velocities, making the accuracy of their estimation critical to the success of the method (e.g., Martí & Müller, 2003). Einfeldt (1988) proposed a way to calculate the signal velocities (for the non-relativistic case). The HLLE scheme is a positively conservative, robust, upwind method for solving the Euler equations.

A major advantage of the RHLLE scheme is that special relativistic effects are included within the scheme itself by internally using the relativistic expressions for the estimates of the minimum and maximum signal velocities. When the conserved quantities are taken as piecewise-constant, the HLLE solver is highly diffusive, leading to unsatisfactory results (e.g. Duncan & Hughes, 1994). The RHLLE method obtains 2nd-order accuracy in space, based on the approach of van Leer (1979), by taking

[1]Also noteworthy is the fact that implicit schemes, unlike explicit schemes, are not subject to the CFL condition (Courant et al., 1928).

the conservative variables to be piecewise-linear. In addition, fluxes are calculated at both the half and full time steps resulting in 2nd-order time accuracy. As discussed in §3.4, for the relativistic case, the Euler equations are strongly coupled via a Lorentz transformation leading to a quartic equation for the flow velocity. Schneider et al. (1993) presented a numerical root-finder to solve the quartic that is sufficiently fast and efficient to be preferable to the analytical method. As I introduce in §3.3.2, this numerical technique breaks down for γ larger than $\sim 10^2$.

3.2 Adaptive Mesh Refinement

Spatial resolution plays a critical role in computational hydrodynamics involving supersonic flows due to the fact that shockwaves, being discontinuities, are thin by nature. However, for a uniform computational grid, computational expense increases rapidly with increased resolution. This is especially true for relativistic simulations that evolve the conserved quantities due to the large overhead of the Lorentz transformations required each time the physical quantities are calculated. Implementing a series of fixed grids of varying grid spacing offers a useful improvement if the areas requiring refinement are known from the onset, e.g., simulations of galaxy clusters where the majority of the action is in the central regions of the cluster. However, for a host of interesting systems, e.g., galactic jets and pulsar winds, features such as shocks travel from one side of the computational domain to the other. In these situations, adaptive mesh refinement (Berger, 1982; Berger & Colella, 1989) alleviates this problem by dynamically refining the computational grid in areas of interest and removing resolution when it is no longer needed, thereby minimizing computational expense.

The hydrodynamic code harnessed for this study employs the AMR framework developed by Quirk (1991) from the work of Berger (1982) and Berger & Colella (1989). The algorithm discretizes the computational domain via a hierarchy of grids

comprised of embedded, rectangular meshes with uniform spacing within a given mesh in the coordinate directions. The user sets the number of cells in the coarse grid, N_c, the number of levels of refinement, L_{max}, and the refinement factor, N_r, for each coordinate direction, by which each cell-dimension is subdivided at level L in constructing the grid at L+1. Grid cells are continually monitored and when specified conditions, e.g. a sudden jump in mass density and pressure, are detected, the cells involved are flagged for refinement and grouped into meshes. The variable controlling flagging is the density change threshold, F_{TOL}, for the application discussed in Chap. 5. The value of F_{TOL} is integral in determining if the density gradient between cells is large enough to warrant refinement. Boundary zones are constructed to ensure that a given mesh at a given grid level contains only flagged cells; i.e., there are no unflagged cells within a mesh of flagged cells. The algorithm further manages processes for sweeping over all meshes in all refinement levels to update the physical variables while ensuring that flow conservation is maintained. The flagging routine allows for a few buffer cells so that shocks are completely contained within refined meshes ensuring that no accuracy is lost due to shock leakage. In addition to employing spatial refinement, the code refines temporally. The time step at level L+1 is smaller than that at level L by a factor equal to the larger of the refinement factors for the coordinate directions. A mismatch in the advancement of the flow solution at adjacent levels could degrade accuracy. In order to avoid this, integration is interleaved at different levels so that the flow solution is synchronized.

3.3 Code Modifications for PWN Simulations

3.3.1 Initial and boundary conditions

As mentioned previously, the code has been extensively tested and used for simulating extragalactic jets. A fixed ambient flow enters the domain along the West (left when "looking down") side of the computational domain and the boundary conditions on

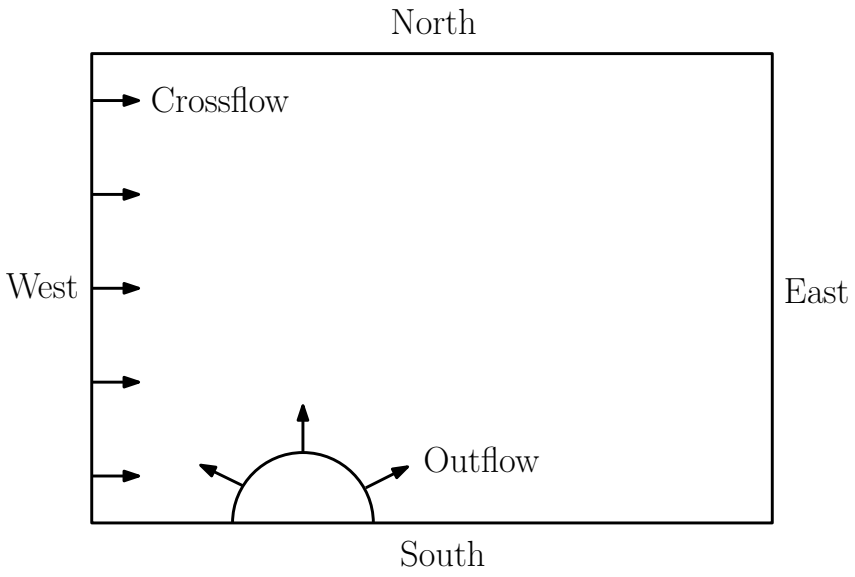

Figure 3.1: Schematic diagram of the computational domain as modified for pulsar wind simulations. Note that the size of the on-axis hemisphere is exaggerated for the sake of clarity.

the North and East sides are extrapolating and on the South side (the flow axis) they are reflecting. Applying the code to pulsar winds required the definition of a wind outflow region. Philip Hughes implemented the modification as follows (see Fig. 3.1 for a schematic). The ambient flow was extended to cover the entire Western boundary and represents the ISM flow resulting from the space motion of the pulsar. The pulsar wind is introduced by imposing an outflow, within the ISM crossflow, from an on-axis hemisphere at every call of the boundary routines. This leads to "cut cells", i.e., those that are partially inside and outside the hemisphere. This is mitigated by averaging the outflow and crossflow variables weighted by the fraction of the cell internal and external to the hemisphere. An initial state for the pulsar-wind problem is specified via the ambient-flow (i.e., crossflow) velocity normalized to the speed of light, v_a, Mach number, $\mathcal{M}$, and mass density, n_a, of the ambient medium, and the Lorentz factor, γ_o, pressure, p_o, and mass density, n_o, of the pulsar-wind outflow. Numerical values are discussed in §5.1.2.

3.3.2 Ultra-relativistic Lorentz factors

Applying the code above to ultra-relativistic flows required refinement of the hydrodynamic solver. This became apparent via an investigation of the solver's behavior when wind Lorentz factors (γ) are large. Beyond $\gamma \sim 10^2$, the solver failed due to the break down of the Newton-Raphson iteration routine involved in the laboratory-frame to rest-frame transformation. The problem lies in the fact that the quartic, $Q(v)$, used to calculate the hydrodynamic flow velocity, exhibits dual roots leading to root confusion as γ increases, as detailed in the next chapter. A simple, highly effective solution, allowing the recovery of Lorentz factors up to 10^6, is to 1) rewrite $Q(v)$ as $Q(\gamma)$, and 2) to use a hybrid method to solve the quartic equation wherein Newton-Raphson iteration and an analytical solution are employed for lower and higher Lorentz factors, respectively. See Chap. 4 for details.

3.4 Recovering the Primitive Variables from R, M, and E

In general, recovering the primitives from the conserved quantities reduces to solving a quartic equation, $Q(v) = 0$, for the flow velocity in terms of R, M, and E. Implementation typically involves a numerical root finder to recover the velocity via Newton-Raphson iteration which is very efficient and provides robustness because it is straightforward to ensure that the computed velocity is always less than the speed of light. This is a powerful method that is independent of dimensionality and symmetry. The latter point follows directly from the fact that symmetry is manifest only as a source term in the Euler equations and does not enter into the derivation of $Q(v)$ (see the axisymmetric example below). Dimensional generality arises because regardless of the coordinate system, one may always write $M = \sqrt{\sum M_{x_i}^2}$, where the M_{x_i} are the components of the momentum-density vector along the orthogonal coordinates x_i (M_ρ and M_z in the axisymmetric example below). In the case of magnetohydrodynamic (MHD) flows, there are, of course, additional considerations. However,

non-magnetic (RHD) simulations still have a significant role to play in astrophysics, e.g., from simulations of extragalactic jets (Hughes et al., 2002; Hughes, 2005) and pulsar wind nebulae (van der Swaluw et al., 2004; Vigelius et al., 2007), to theories of the generation of gamma-ray bursts (Zhang et al., 2003) and the collapse of massive stars to neutron stars and black holes (Shibata, 2003).

As an example, consider the case of the axisymmetric, relativistic Euler equations, which I apply to pulsar winds. In cylindrical coordinates ρ and z, and defining the evolved-variable, flux, and source vectors

$$\begin{aligned} U &= (R, M_\rho, M_z, E)^T, \\ F^\rho &= (Rv^\rho, M_\rho v^\rho + p, M_z v^\rho, (E+p)v^\rho)^T, \\ F^z &= (Rv^z, M_\rho v^z, M_z v^z + p, (E+p)v^z)^T, \\ S &= (0, p/\rho, 0, 0)^T, \end{aligned} \tag{3.1}$$

the Euler equations may be written in almost-conservative form as:

$$\frac{\partial U}{\partial t} + \frac{1}{\rho}\frac{\partial}{\partial \rho}(\rho F^\rho) + \frac{\partial}{\partial z}(F^z) = S.$$

The pressure is given by the ideal gas equation of state $p = (\Gamma - 1)(e - n)$, where e and Γ are the rest-frame total energy density and the adiabatic index. Note that the velocity and pressure appear explicitly in the relativistic Euler equations, in addition to the evolved variables, and that pressure and rest density are needed for the computation of the wave speeds that form the basis of Godunov-type numerical, hydrodynamic solvers. These values are obtained by performing a Lorentz transformation where the

rest-frame values are required:

$$\begin{aligned} R &= \gamma n, \\ M_\rho &= \gamma^2(e+p)v^\rho, \\ M_z &= \gamma^2(e+p)v^z, \\ E &= \gamma^2(e+p)-p, \\ \gamma &= (1-v^2)^{-1/2}, \end{aligned} \tag{3.2}$$

where $v^2 = (v^\rho)^2 + (v^z)^2$ and $M^2 = \gamma^4(e+p)^2[(v^\rho)^2+(v^z)^2] = \gamma^4(e+p)^2v^2$. When the adiabatic index is constant, combining the above equations with the equation of state creates a closed system which yields the following quartic equation for v in terms of $Y \equiv M/E$ and $Z \equiv R/E$:

$$\begin{aligned} Q(v) &= (\Gamma-1)^2(Y^2+Z^2)v^4 - 2\Gamma(\Gamma-1)Yv^3 \\ &+ \left[\Gamma^2 + 2(\Gamma-1)Y^2 - (\Gamma-1)^2Z^2\right]v^2 \\ &- 2\Gamma Yv + Y^2 = 0. \end{aligned} \tag{3.3}$$

Component velocities, and the rest-frame total energy and mass densities are then given by:

$$\begin{aligned} v^\rho &= M_\rho \frac{v}{M}, \\ v^z &= M_z \frac{v^\rho}{M_\rho}, \\ e &= E - M_\rho v^\rho - M_z v^z, \\ n &= \frac{R}{\gamma}. \end{aligned}$$

3.5 Summary

This dissertation project was motivated by the desire to understand asymmetric pulsar wind nebulae. Toward this end, along with Advisor Philip A. Hughes, I undertook simulations of bow-shock PWNe (see Chap. 5). Given the highly-relativistic nature

of pulsar winds, a relativistic treatment of the computational flow dynamics is essential to obtaining realistic results for the interaction of the wind with the ambient medium. I have applied (see Chap. 5) an existing fully-relativistic, 2D-hydrodynamic code employing the Adaptive Mesh Refinement (AMR) framework of Quirk (1991). AMR locally refines the computational mesh in areas of interest, allowing for high resolution while minimizing computational expense. I discussed how the code was modified to satisfy the initial and boundary conditions for simulating the interaction of pulsar winds with the ambient flow. The code has been previously applied to studies of galactic jets with Lorentz factors up to 50 (Duncan & Hughes, 1994; Hughes et al., 2002).

Application to pulsar wind nebulae with bulk Lorentz factors $\sim 10^6$ necessitated a substantial modification to the hydrodynamic solver. As with many modern solvers, the evolved quantities are the conserved variables (R, M, and E). I discussed the formalism of recovering the physical quantities (n, p, and v) in the context of the Euler equations which, for a constant adiabatic index, involves the solution of a quartic equation for the flow velocity. I previewed the problem, noted that the shape of this velocity quartic leads to a confusion of roots at higher Lorentz factors, and advertised that the solution is to recast the quartic in terms of the Lorentz factor. The following chapter deals with this subject in detail.

CHAPTER 4

Refining a Hydrodynamic Solver to Admit Ultra-relativistic Flows

I have applied (Chap. 5) a proven, robust astrophysical code (see Chap. 3) with previous application to relativistic galactic jets with $\gamma \leq 50$ (Duncan & Hughes, 1994; Hughes et al., 2002) to a study of pulsar wind nebulae. The ultra-relativistic nature of pulsar winds necessitated an investigation of the behavior of the primitives algorithm upon taking $\gamma >> 1$. I found that beyond $\gamma \sim 10^2$ the algorithm suffers a severe degradation in accuracy that worsens with increasing Lorentz factor until complete breakdown occurs due to the failure of the Newton-Raphson iteration process used to calculate the flow velocity.

The problem lies in the shape of the quartic, $Q(v)$, one must solve to calculate the primitive variables. The quartic equation as derived using the velocity as a variable exhibits two roots for typical physical parameters of the flow (see Fig. 4.1). In general, for $\gamma < 10^2$, the two roots are sufficiently separated on the velocity axis such that the Newton-Raphson (N-R) iteration method converges to the correct zero very quickly and accurately (for $M/E < 0.9$ and $R/E > 10^{-5}$, corresponding to $\gamma < 2$, the roots approach each other sufficiently such that the incorrect root is selected; see §4.3). In fact, N-R iteration can be so efficient that it is more desirable to use this method than it is to calculate the roots of the quartic analytically (see §4.2). However, as the Lorentz factor of the flow increases, the roots move progressively closer together and the minimum in $Q(v)$ approaches zero. Eventually, the minimum equals zero to machine accuracy which causes $dQ/dv = 0$ to machine accuracy resulting in a

divide by zero and the Newton-Raphson method fails (see Fig. 4.2). I present the solution below. I show that the use of an analytical quartic root finder is required for Lorentz factors above 10^2, but that an iterative quartic root finder, which is known to be robust for Lorentz factors up to at least 50, offers a 24% speed advantage. I demonstrate the existence of a simple diagnostic allowing for a hybrid primitives recovery algorithm that includes an automatic, real-time toggle between the iterative and analytical methods. I further determine the accuracy of the iterative and hybrid algorithms for a comprehensive selection of input parameters.

4.1 Refinement of the Root Finder

Rewriting the velocity quartic, $Q(v)$ (Eqn. 3.3), in terms of the Lorentz factor (i.e., make the substitution $v^2 = 1 - \gamma^{-2}$) to obtain the quartic equation in γ (recall $Y \equiv M/E$ and $Z \equiv R/E$):

$$\begin{aligned} Q(\gamma) &= \Gamma^2(1-Y^2)\gamma^4 - 2\Gamma(\Gamma-1)Z\gamma^3 \\ &+ \left[2\Gamma(\Gamma-1)Y^2 + (\Gamma-1)^2Z^2 - \Gamma^2\right]\gamma^2 \\ &+ 2\Gamma(\Gamma-1)Z\gamma - (\Gamma-1)^2(Y^2+Z^2) = 0, \end{aligned} \tag{4.1}$$

paves the way for a simple and highly effective solution (see §4.3 for details) to the above problem. As Fig. 4.1 exemplifies, $Q(\gamma)$ exhibits a single root for the physical range $\gamma \geq 1$. However, Newton-Raphson iteration also fails in this case at high Lorentz factors because of the steepness of the rise in $Q(\gamma)$ through the root. Thus, I choose to use an analytical method of solving a quartic, but note that there are other ways to mitigate the problems that arise in high-γ primitives recovery (e.g., the appendix in Mignone & McKinney, 2007). Below, I discuss the implementation.

4.1.1 Solving a quartic equation

I use the prescription due to Bronshtein & Semendyayev (1997) in order to analytically solve for the roots of a quartic. I chose this method because it provides equations

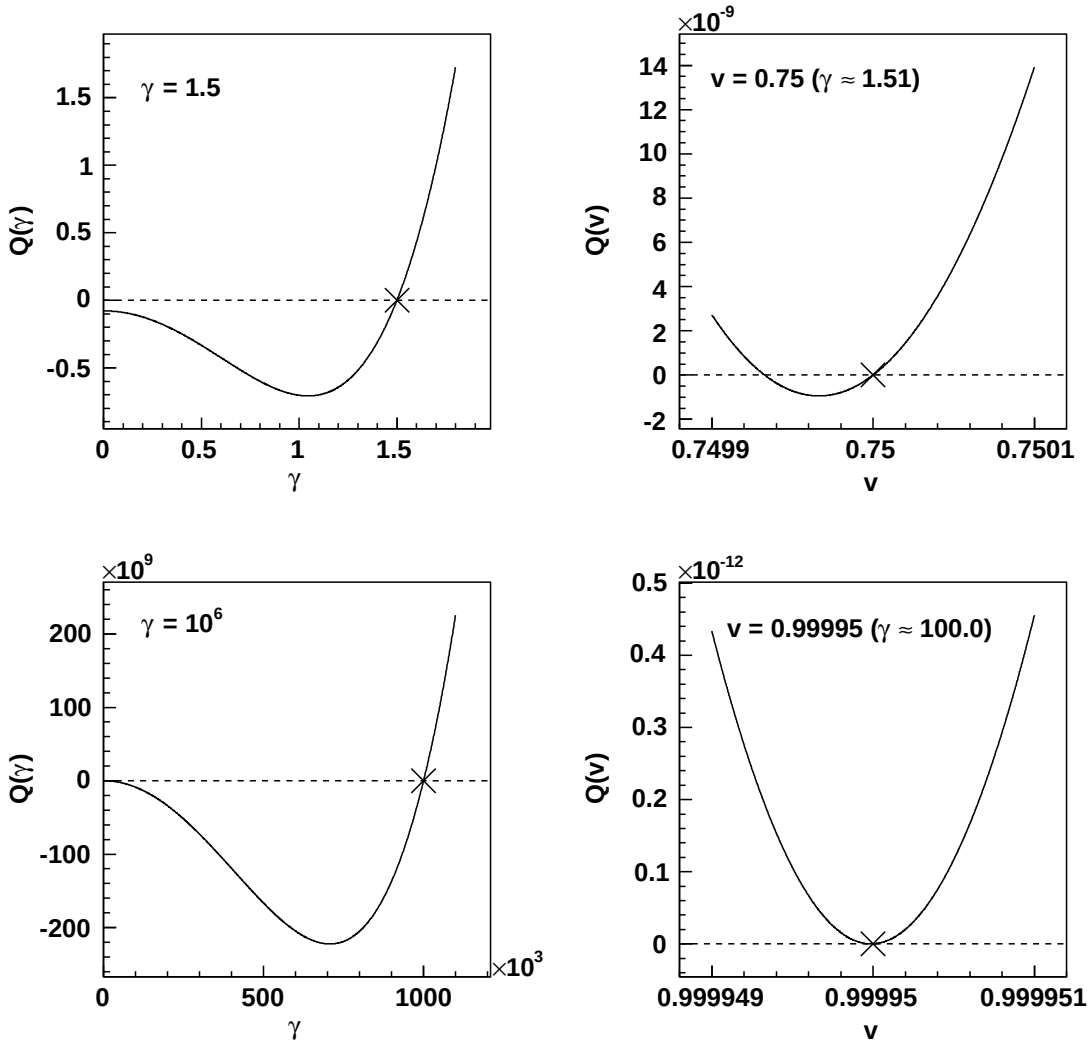

Figure 4.1: The left-hand plots show the shape of the Lorentz factor quartic over a run of Lorentz factors for a mildly relativistic flow ($\gamma_{rad} = 1.5$) and an ultra-relativistic flow ($\gamma_{rad} = 10^6$). The right-side plots show the shape of the velocity quartic over a run of velocity for a mildly relativistic flow ($v_{rad} = 0.75$ or $\gamma_{rad} \approx 1.5$) and a highly (but not ultra-) relativistic flow ($v_{rad} = 0.99995$ or $\gamma_{rad} \approx 10^2$). The crosses mark the location of the physical root. From the plot in the lower right, one can see the onset of the zero derivative problem as the roots are not distinguishable from each other or the local minimum even on a scale of 10^{-13}, which begins to encroach on the limit of 8-byte accuracy.

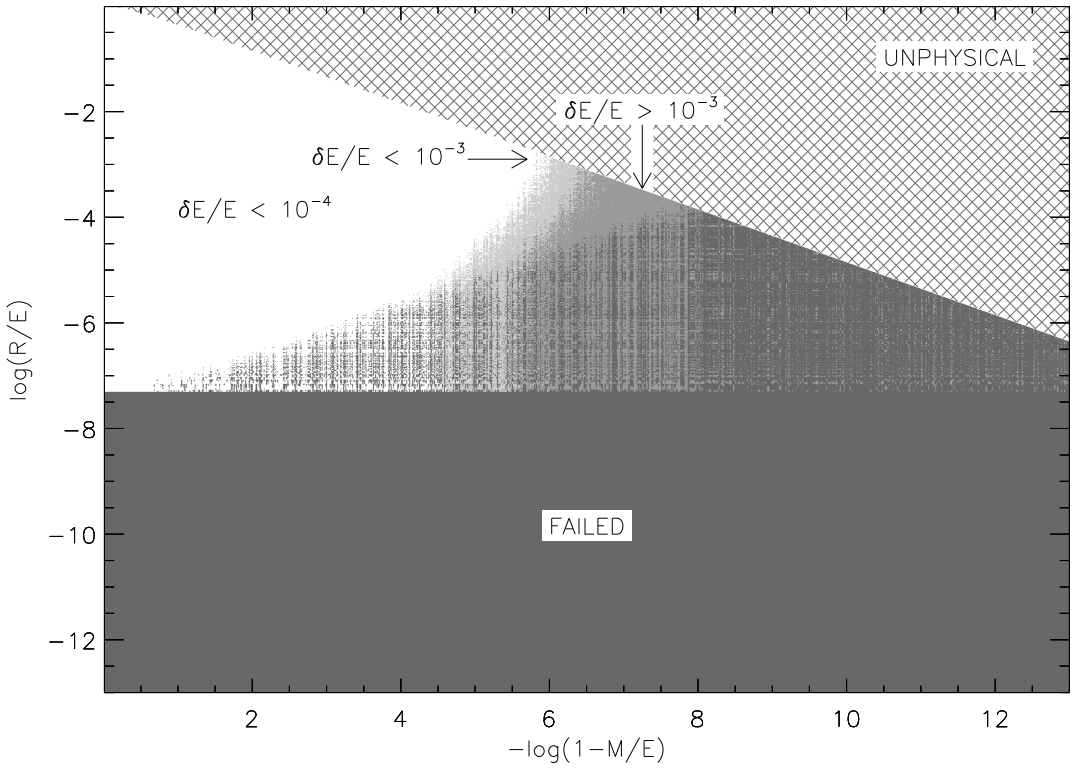

Figure 4.2: The accuracy (estimated as $\delta E/E$) of the Newton-Raphson (N-R) iterative primitives algorithm where white, light grey, medium grey, dark grey, and hatched regions correspond, respectively, to an accuracy of order at least 10^{-4}, at least 10^{-3}, worse than 10^{-3}, failure, and unphysical input ($R^2/E^2 \geq 1 - M^2/E^2$). Note that the Lorentz factor varies from order 1 at the far left to order 10^6 at the far right. There is a sizable white region representing $M/E < 0.999999$ ($\gamma < 500$) and $R/E > 5 \times 10^{-8}$ within which accuracy is generally significantly better than 10^{-4}. N-R iteration is unreliable due to sporadic failures for all M/E and R/E such that $R/E < 5 \times 10^{-8}$ and for an ever increasing fraction of $R/E > 5 \times 10^{-8}$ as M/E increases until accuracy becomes unacceptable or the code fails outright for M/E and R/E such that $M/E > 0.999999$. Failures are due to divide by zero (see §4.1) or nonconvergence within a reasonable number of iterations.

for the roots of the quartic that are the most amenable (of the methods surveyed) to integration into a computational environment. In order to provide a complete picture of the method, which includes steps not found in Bronshtein & Semendyayev (1997), I reproduce some sections of that text. I proceed as follows.

Given a quartic equation in x:

$$a_4x^4 + a_3x^3 + a_2x^2 + a_1x + a_0 = 0,\ a_n \in \Re,\ a_4 \neq 0, \tag{4.2}$$

normalizing the equation (dividing by a_4) and making the substitution $y = x + \frac{a_3}{4a_4}$ results in the reduced form:

$$y^4 + Py^2 + Qy + R \ = \ 0,$$

where, defining $\tilde{a}_n \equiv a_n/a_4$:

$$\begin{aligned} P &\equiv -\frac{3}{8}\tilde{a}_3^2 + \tilde{a}_2, \\ Q &\equiv \left(\frac{\tilde{a}_3}{2}\right)^3 - \left(\frac{\tilde{a}_3}{2}\right)\tilde{a}_2 + \tilde{a}_1, \\ R &\equiv -3\left(\frac{\tilde{a}_3}{4}\right)^4 + \left(\frac{\tilde{a}_3}{4}\right)^2\tilde{a}_2 - \left(\frac{\tilde{a}_3}{4}\right)\tilde{a}_1 + \tilde{a}_0. \end{aligned}$$

These coefficients allow the definition of the *cubic resolvent*:

$$u^3 + 2Pu^2 + (P^2 - 4R)u - Q^2 = 0, \tag{4.3}$$

upon whose solutions the solutions of the original quartic (Eqn. 4.2) depend. The product of the solutions of the cubic resolvent $u_1u_2u_3 = Q^2$ must be positive by Vieta's theorem. The characteristics of the quartic's roots depend on the nature of the roots of the cubic resolvent (see Tab. 4.1).

Given the solutions of the cubic resolvent u_1, u_2, and u_3, the solutions of the

Table 4.1: The dependence of the solutions to the parent quartic on the solutions to the cubic resolvent.

Solutions of the cubic resolvent	Solutions of the quartic equation
all real and positive	all real
all real, one positive	two complex conjugate (cc) pairs
one real, one cc pair	two real, one cc pair

quartic (Eqn. 4.2) are

$$\begin{aligned} x_1 &= \frac{1}{2}(\sqrt{u_1}+\sqrt{u_2}+\sqrt{u_3}) - \frac{a_3}{4a_4}, \\ x_2 &= \frac{1}{2}(\sqrt{u_1}-\sqrt{u_2}-\sqrt{u_3}) - \frac{a_3}{4a_4}, \\ x_3 &= \frac{1}{2}(-\sqrt{u_1}+\sqrt{u_2}-\sqrt{u_3}) - \frac{a_3}{4a_4}, \\ x_4 &= \frac{1}{2}(-\sqrt{u_1}-\sqrt{u_2}+\sqrt{u_3}) - \frac{a_3}{4a_4}. \end{aligned} \tag{4.4}$$

4.1.2 Solving a cubic equation

The equations of the previous section reduce the problem of solving a quartic equation to that of solving a cubic equation (i.e., the cubic resolvent of Eqn. 4.3).

Once again, following Bronshtein & Semendyayev (1997) (note the similarity to the method in the previous section), given a cubic equation:

$$b_3u^3 + b_2u^2 + b_1u + b_0 = 0,\ b_n \in \Re,\ b_3 \neq 0, \tag{4.5}$$

normalizing the equation and making the substitution $v = u + b_2/3b_3$ results in the reduced form:

$$v^3 + pv + q = 0,$$

where, defining $\tilde{b}_n \equiv b_n/b_3$:

$$\begin{aligned} p &\equiv -\frac{1}{3}\tilde{b}_2^2 + \tilde{b}_1, \\ q &\equiv 2\left(\frac{\tilde{b}_2}{3}\right)^3 - \left(\frac{\tilde{b}_2}{3}\right)\tilde{b}_1 + \tilde{b}_0. \end{aligned}$$

Table 4.2: The dependence of the solutions of a cubic equation on the sign of the discriminant (assuming a real variable).

D	Solutions of the cubic equation
positive	one real, one complex conjugate pair
negative	all real and distinct
$= 0$	all real, two (one, if $p = q = 0$) distinct

These coefficients allow the definition of the *discriminant*:

$$D \equiv \left(\frac{p}{3}\right)^3 + \left(\frac{q}{2}\right)^2, \tag{4.6}$$

upon which the characteristics of the solutions of the cubic equation depend (see Tab. 4.2).

Given p, q, and D, Cardando's formula for the reduced form of the cubic leads to the solutions of the original cubic (Eqn. 4.5):

$$\begin{aligned} u_1 &= s + t - \frac{b_2}{3b_3}, \\ u_2 &= -\frac{1}{2}(s+t) - \frac{b_2}{3b_3} + i\frac{\sqrt{3}}{2}(s-t), \\ u_3 &= -\frac{1}{2}(s+t) - \frac{b_2}{3b_3} - i\frac{\sqrt{3}}{2}(s-t), \end{aligned} \tag{4.7}$$

where:

$$\begin{aligned} s &\equiv \sqrt[3]{-\frac{1}{2}q + \sqrt{D}}, \\ t &\equiv \sqrt[3]{-\frac{1}{2}q - \sqrt{D}}, \\ i &\equiv \sqrt{-1}. \end{aligned}$$

If $D \leq 0$, then the cubic has three real roots, subject to the following two subcases, and the four real roots of the quartic follow directly from Eqn. 4.4. If $D = 0$, then $s = t$ and the cubic has three real solutions that follow directly from Eqn. 4.7 from which one can see that two are degenerate. If $D < 0$, the cubic has three distinct

real roots. Obtaining these solutions via Eqn. 4.7 requires intermediate complex arithmetic. However, this may be circumvented by making the substitutions:

$$\begin{aligned} r &= \sqrt{-\left(\frac{p}{3}\right)^3} \\ \cos(\phi) &= -\frac{q}{2r}, \end{aligned}$$

in which case the solutions of the cubic (Eqn. 4.5) are:

$$\begin{aligned} u_1 &= 2\sqrt[3]{r}\cos\left(\frac{\phi}{3}\right) - \frac{b_2}{3b_3}, \\ u_2 &= 2\sqrt[3]{r}\cos\left(\frac{\phi}{3} + \frac{2\pi}{3}\right) - \frac{b_2}{3b_3}, \\ u_3 &= 2\sqrt[3]{r}\cos\left(\frac{\phi}{3} + \frac{4\pi}{3}\right) - \frac{b_2}{3b_3}. \end{aligned} \tag{4.8}$$

If $D > 0$, then the cubic has one real root and a pair of complex conjugate roots and the quartic has two real roots and a pair of complex conjugate roots (see Tab. 4.1). Finding the roots of the quartic involves intermediate complex arithmetic which may be circumvented as follows. Defining:

$$\begin{aligned} R &\equiv -\frac{1}{2}(s+t) - \frac{b_2}{3b_3}, \\ C &\equiv \frac{\sqrt{3}}{2}(s-t), \end{aligned}$$

Eqn. 4.7 may be rewritten as:

$$\begin{aligned} u_1 &= s + t - \frac{b_2}{3b_3}, \\ u_2 &= R + iC, \\ u_3 &= R - iC. \end{aligned}$$

Next, I have $u_{2,3} = \sqrt{R^2 + C^2}e^{\pm iC/R}$. I then obtain the roots of the quartic from Eqn. 4.4:

$$\begin{aligned} x_{1,2} &= \frac{\sqrt{u_1}}{2} - \frac{a_3}{4a_4} \pm \sqrt[4]{R^2 + C^2}\cos\left(\frac{C}{2R}\right), \\ x_{3,4} &= -\frac{\sqrt{u_1}}{2} - \frac{a_3}{4a_4} \pm i\sqrt[4]{R^2 + C^2}\sin\left(\frac{C}{2R}\right). \end{aligned} \tag{4.9}$$

Note that x_1 and x_2 are the two real solutions.

4.2 The Refined Primitives Algorithm

Using the analytical method above, I created a SRHD primitive algorithm called "REST_FRAME" developed from the non-relativistic algorithm of the same name. Given the speed advantage of the iterative root finder (see below), it a desirable choice over the analytical method within its regime of applicability, i.e., for low Lorentz factors. As Fig. 4.2 shows, the iterative root finder is accurate to order 10^{-4} (see §4.3) for a sizable region of parameter space including all R/E above the diagonal line between the points (0, −7) & (9, 0) in the $\log(R/E)$ vs. $-\log(1-M/E)$ plane (i.e., for $\log(R/E) \geq -(7/9) \times \log(1-M/E) - 7$). Therefore, for a given M/E and R/E, the code checks if this inequality is true; if so, it calls the iterative root finder and, if not, it calls the analytical root finder. REST_FRAME calculates the primitive variables given the conservative variables and the adiabatic index as represented in the pseudo-code in §A.1 of the Appendix (note that it is a 2D example).

Using the Intel Fortran library function CPU_TIME, I calculated the CPU time required to execute 5×10^7 calls to REST_FRAME for $Y = 0.9975$ & $Z = 1\times10^{-4}$ ($\gamma \sim 10$) using the Newton-Raphson iterative method with $Q(v)$ and 8-byte arithmetic, and the analytical method with $Q(\gamma)$ and both 8-byte & 16-byte arithmetic (I investigated the use of 16-byte arithmetic due to an issue with subtractive cancellation – see §4.3). The CPU time for each of these scenarios was 29.5, 36.5 (averaged over ten runs and rounded to the nearest half second), and ∼11650 seconds (one run only), respectively. This indicates that while using the 8-byte analytical method is satisfactory, it is advantageous to use the iterative method when Lorentz factors are sufficiently low, and that the use of 16-byte arithmetic is a nonviable option. This result is not surprising as the accuracy of Newton-Raphson iteration improves by approximately one decimal place per iterative step (Duncan & Hughes, 1994) and the relative inefficiency of 16-byte arithmetic is a known issue (e.g., Perret-Gallix, 2006).

4.3 Solver Accuracy

The input parameters for our primitives algorithm are the ratios of the laboratory-frame momentum and mass densities to the laboratory-frame energy density (recall $Y \equiv M/E$ and $Z \equiv R/E$) both of which must be less than unity in order for solutions of Eqn. 3.2 to exist. In addition, the condition $Y^2 + Z^2 < 1$ must be met. Along with the fact that Y and Z must also be positive, this defines the comprehensive and physical input parameter space to be $0 < Y, Z < 1$ such that $Y^2 + Z^2 < 1$ (I identify a particular region of parameter space applicable to pulsar winds in the next section). I tested the accuracy of the iterative and hybrid primitives algorithms within this space as follows.

First, as I am most interested in light, highly relativistic flows (i.e., Z small and Y close to unity), to define the accuracy-search space I elected to use the quantities $-\log(1-Y)$, which for values greater than unity gives $0.9 < Y < 1$, and $\log(Z)$, which for values less than negative unity gives $Z \ll 1$. I selected $0 < -\log(1-Y) < 13$ and $-13 < \log(Z) < 0$ corresponding to Lorentz factors (γ) between 1 and 2×10^6. I chose a range with a maximal γ slightly above 1×10^6 in order to completely bound the PWN parameter space defined in the next section.

Choosing a relativistic equation of state $\Gamma = 4/3$ and using 1300 points for both $-\log(1-Y)$ and $\log(Z)$, I tested the accuracy of REST_FRAME by passing it Y and Z, choosing $E = 1$, and using the returned primitive quantities to derive the calculated energy density E_c, and calculating the difference $|1 - E_c/E| \equiv \delta E/E$. I chose this estimate of the error because $\delta E/E \sim \delta\gamma/\gamma$ and $\delta\gamma/\gamma$ is tied to the accuracy of the numerical, hydrodynamic technique (see the final paragraph in this section).

The results for the Newton-Raphson (N-R) and hybrid methods are given in Figs. 4.2 & 4.3 which show where the accuracy is of order at least 10^{-4}, at least 10^{-3}, worse than 10^{-3}, and where failure and unphysical input ($Z^2 \geq 1 - Y^2$) occur. I chose an accuracy of order 10^{-4} as the upper cutoff because N-R iteration returns

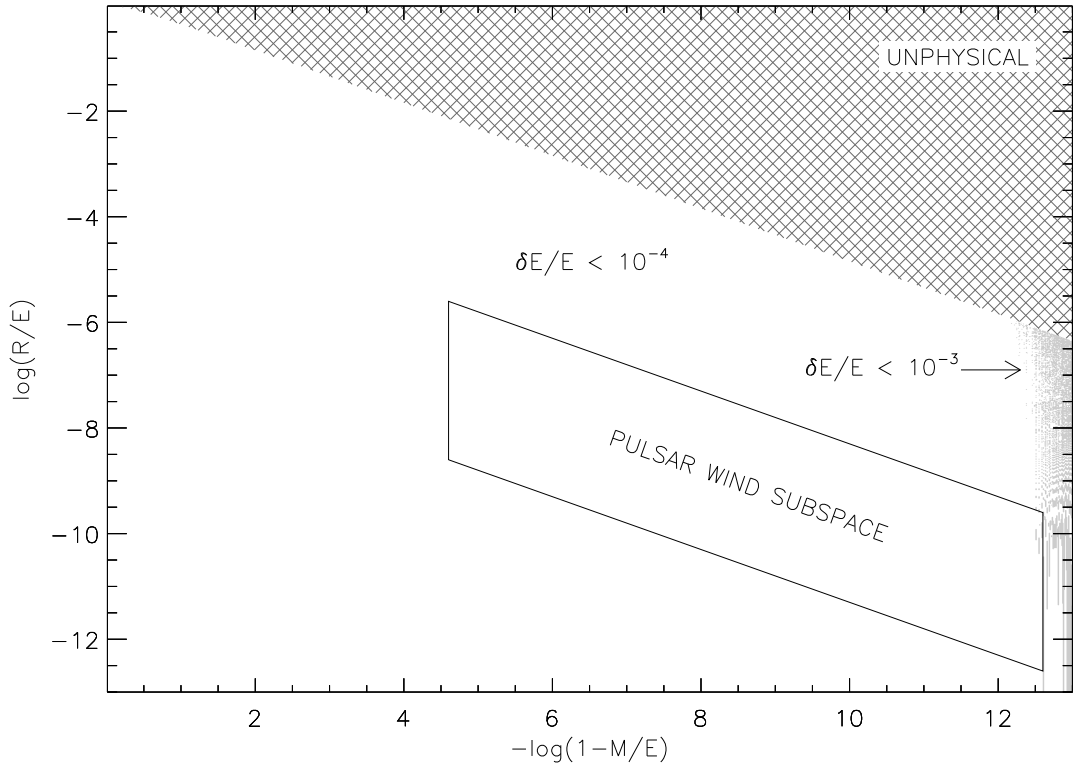

Figure 4.3: The accuracy (estimated as $\delta E/E$) of the hybrid primitives algorithm where white, light grey, and hatched regions correspond, respectively, to an accuracy of order at least 10^{-4}, at least 10^{-3}, and nonphysical input ($R^2/E^2 \geq 1 - M^2/E^2$). Note that the Lorentz factor varies from order 1 at the far left to order 10^6 at the far right. The space between the parallel lines represents PWNe input parameter space. The accuracy degradation at the extreme right is due to subtractive cancellation in the 4^{th}-order coefficient of the Lorentz-factor quartic as $M/E \rightarrow 1$.

accuracies on this order for $\gamma < 50$ and relativistic, hydrodynamic simulations of galactic jets by Duncan & Hughes (1994) and Hughes et al. (2002) produced robust results for Lorentz factors up to 50 using N-R iteration. An additional result of interest is that the ultra-relativistic approximation for v (i.e., taking $R = 0$ thereby reducing $Q(v) = 0$ to a quadratic equation) manages an accuracy of at least 10^{-4} for a large portion of the physical $Y - Z$ plane (see Fig. 4.4).

Fig. 4.2 shows the accuracy of the N-R iterative method. There are several noteworthy features. First is the presence of a sizable region corresponding to $\gamma < 500$ within which accuracy is generally significantly better than 10^{-4}. Second is that

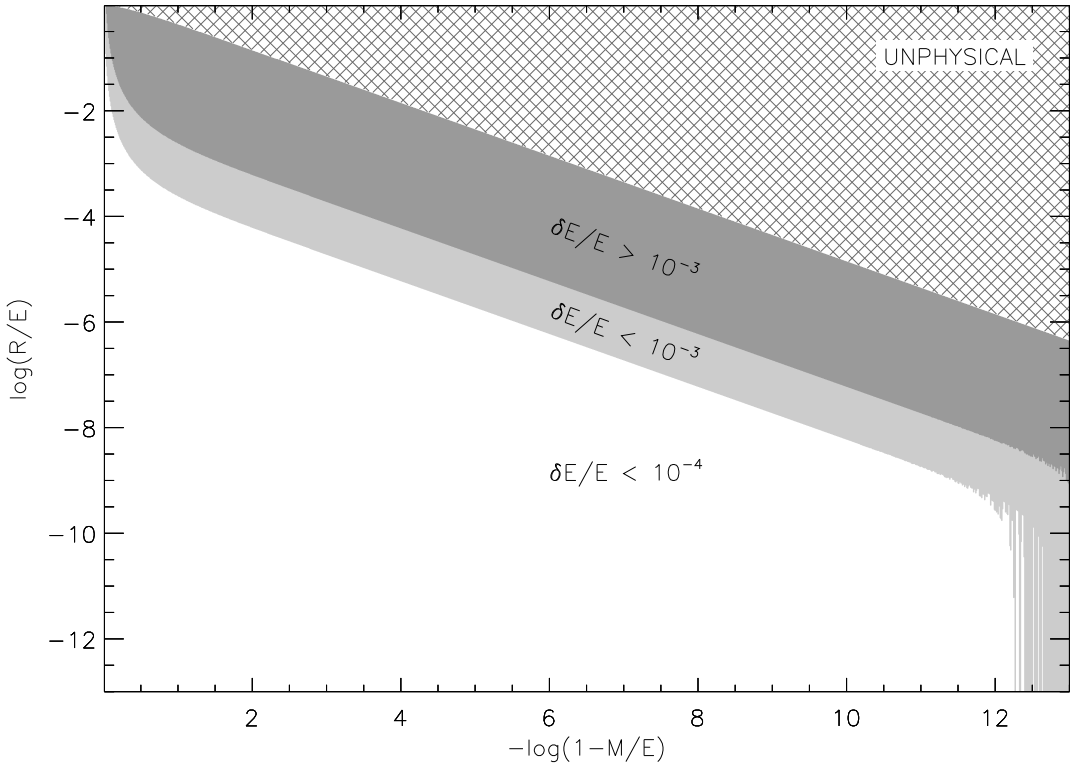

Figure 4.4: The accuracy (estimated as $\delta E/E$) of the ultra-relativistic approximation of the flow velocity where white, light grey, medium grey, and hatched regions correspond to an accuracy of order at least 10^{-4}, at least 10^{-3}, worse than 10^{-3}, and unphysical input ($R^2/E^2 \geq 1 - M^2/E^2$), respectively. Note that the Lorentz factor varies from order 1 at the far left to order 10^6 at the far right. The accuracy degradation at the extreme right is due to the fact that the fractional error in the Lorentz factor is proportional to the fractional error in the velocity divided by $1 - v^2$ which diverges as $v \rightarrow 1$.

N-R iteration is unreliable due to sporadic failures for increasing Lorentz factors until accuracy becomes unacceptable or the code fails outright due to divide by zero (see §4.1) or non-convergence within a reasonable number of iterations. In addition, though N-R iteration has been widely established as the primitives recovery method of choice for flows with Lorentz factors less than order 10^2, I found that for a subset of parameters, corresponding to $\gamma < 2$, the N-R algorithm suffered an unacceptable degradation in accuracy. The key to this problem lies in the how the flow velocity (v) is initially estimated for the first iterative cycle as follows:

1. the established approach (Duncan & Hughes, 1994; Schneider et al., 1993) is to bracket v with

$$\begin{aligned} v_{max} &= min(1, Y + \delta), \\ v_{min} &= \frac{\Gamma - \sqrt{\Gamma^2 - 4(\Gamma - 1)Y^2}}{2Y(\Gamma - 1)}, \end{aligned} \tag{4.10}$$

   where $\delta \sim 10^{-6}$ and v_{min} is derived by taking the ultra-relativistic limit (i.e., $R = 0$)
2. the initial velocity is then $v_i = (v_{min} + v_{max})/2 + \eta$, where $\eta = (1 - Z)(v_{min} - v_{max})$ for $v_{max} > \epsilon$ and $\eta = 0$ otherwise (ϵ order 10^{-9})
3. this method fails due to selection of the incorrect root when the roots converge
4. thus, I make a simpler initial estimate of $v_i = v_{max}$, which guarantees that v_i is "uphill" from v for all physical $Y - Z$ space and that N-R iteration converges on v.

Fig. 4.3 shows that the hybrid algorithm REST_FRAME is accurate to at least 10^{-4} for all but a smattering of the highest Lorentz factors. In fact, it is significantly more accurate over the majority of the physical portion of the $Y - Z$ plane. The space between the parallel lines represents the PWN input parameters discussed in the next section. I find that multiplying $Q(\gamma)$ by $(Y^2 - Y^{-2})$ and rewriting the new a_4 ($\tilde{a}_4$) in terms of the new a_2 ($\tilde{a}_2$) and new a_0 ($\tilde{a}_0$), e.g., $\tilde{a}_4 = 1 + Y^2 - \tilde{a}_0 - \tilde{a}_2$, improves

the accuracy somewhat, but does not entirely mitigate the problem. The issue of accuracy loss at large Lorentz factors in 8-byte primitives algorithms is a known issue (Noble, 2003; Mignone & McKinney, 2007) for which I know of no complete 8-byte solution. Employing 16-byte arithmetic provides spectacular accuracy but introduces an unacceptable increase in run time (see §4.2).

The issue of what constitutes an acceptable error in the calculated Lorentz factor is decided by the fact that a fractional error in γ translates to the same fractional error in p and n which are needed to calculate the wave speeds that form the basis of the numerical, hydrodynamic technique, a Godunov scheme (Godunov, 1959) which approximates the solution to the local Riemann problem by employing an estimate of the wave speeds. While I do not know *a priori* how accurate this estimate needs to be, past studies have shown that an accuracy of order 10^{-4} is sufficient, and so I proceed with 8-byte simulations of pulsar winds. If future developments so dictate, shock-tube tests (Thompson, 1986) are available to validate the accuracy of the computation of well-defined flow structures. It is also noteworthy that while $\gamma = 10^6$ is the canonical bulk Lorentz factor for pulsar winds, $\gamma = 10^4$ and 10^5 are still in the ultra-relativistic regime, and it may very well prove to be that these Lorentz factors are high enough to elucidate the general ultra-relativistic, hydrodynamic features of such a system. The hybrid algorithm achieves accuracies of at least 10^{-6} for $\gamma \sim 10^5$, which is safely in the acceptable accuracy regime.

4.4 Summary

I discussed the application of an existing special relativistic, hydrodynamic (SRHD) primitive-variable recovery algorithm to ultra-relativistic flows (Lorentz factor, γ, of 10^2–10^6) and the refinement necessary for the numerical velocity root finder to work in this domain. The velocity quartic, $Q(v)$, exhibits dual roots in the physical velocity range that move progressively closer together for larger γ leading to a divide by zero

and the failure of the Newton-Raphson iteration method employed by the existing primitives algorithm. The solution was to recast the quartic to be a function, $Q(\gamma)$, of γ. I demonstrated that $Q(\gamma)$ exhibits only one physical root. However, Newton-Raphson iteration also failed in this case at high γ, due to the extreme slope of the quartic near the root, necessitating the use there of an analytical numerical root finder.

The timing analysis indicated that using $Q(\gamma)$ with the 8-byte analytical root finder increased run time by only 24% compared to using $Q(v)$ with the 8-byte iterative root finder (based on 10 trial runs), while using $Q(\gamma)$ with the 16-byte analytical root finder ballooned run time by a factor of approximately 400. The iterative root finder is accurate to order 10^{-4} for a sizable region of parameter space corresponding to Lorentz factors on the order of 10^2 and smaller. Therefore, I implemented a computational switch that checks the values of M/E and R/E and calls the iterative or analytical root finder accordingly, thereby creating a hybrid primitives recovery algorithm called REST_FRAME.

In addition, an exploration of parameter space suggests that the discriminant of the cubic resolvent (as defined by Eqn. 4.6 in §4.1.1) will always be positive for physical flows. Therefore, I did not include code for negative discriminants in the routine. Formal proof remains elusive, however, leaving potential for future work.

I have shown that the refined primitives recovery algorithm is capable of calculating the primitive variables from the conserved variables to an accuracy of at least order 10^{-4} for $\gamma \leq 10^6$, with significantly better accuracy for $\gamma \leq 10^5$, and slightly worse (order 10^{-3}) for a small portion of the space corresponding to the highest Lorentz factors. I traced the degradation in accuracy for larger Lorentz factors to the effect of subtractive cancellation. Past studies have shown that an accuracy of order 10^{-4} is capable of robustly capturing hydrodynamic structures.

CHAPTER 5

Application to Pulsar Wind Nebulae

In this chapter, I present the application of the relativistic, hydrodynamic code discussed in Chaps. 3 & 4 to the interaction of pulsar winds with the interstellar medium. As Bucciantini (2002) discussed for the case of pulsar bow-shock nebulae, the magnetized, relativistic pulsar wind interacts indirectly with the ISM. The interaction is mediated by the magnetic field which is advected by the wind and compressed within the head of the nebula. Since the particle cross-sections are very small, this implies that the gyroradius is the mean free particle path. Blandford & Rees (1974) give an expression for the gyroradius, r_g, of a proton with Lorentz factor γ subject to a magnetic field B:

$$r_g \sim 10^{-12} \frac{\gamma}{B} \text{ pc} ,$$

where B is measured in Gauss. Taking the Guitar nebula as an example, the angular extent of the bubble is ~ 30 arcseconds (see Fig. 1.4). Chatterjee & Cordes (2002) quote a distance of 2.0 ± 0.5 kpc which implies a minimum bubble diameter of ~ 0.2 pc. Constraining the gyroradius to be less than 1% of this value, e.g., 10^{-3} pc, for $\gamma \sim 10^6$ thus requires the magnetic field to be greater than 10^{-3} G. This is clearly satisfied very close to the pulsar (surface $B \sim 10^{12-13}$ G) where the canonical Lorentz factor of 10^6 is realized. At the light cylinder γ is $\sim 10^2 \Rightarrow B > 10^{-7}$ G, which is an order of magnitude smaller than the ambient Galactic field. Therefore, everywhere within PWNe the gyroradii of pulsar wind particles are small compared to the nebular diameter scale and a fluid approach to modeling is valid.

This leaves the question of why a purely hydrodynamic treatment is warranted. After all, the theoretical paradigm for pulsar magnetics has long prescribed a strong, virtually dipole magnetic field. This leads to the conclusion that magnetic fields must certainly have a significant effect on the energy and transport of particles in a pulsar wind. However, there is a fundamental weakness in the pulsar paradigm. Near the light cylinder, pulsar models predict that the ratio of the Poynting flux to kinetic-energy flux, σ, should be of order of 10^4 (Arons, 2002). The canonical models for the Crab nebula (Rees & Gunn, 1974; Kennel & Coroniti, 1984a) require $\sigma << 1$ immediately behind the termination shock in order to meet boundary conditions with the ambient medium, and simple conservation arguments imply that σ should be constant. This is the long-standing "σ-problem".

In addition, the magnetic field is largely unknown. First, the field geometry of the pulsar wind is far from settled (Chevalier, 2000; Melatos, 2004), and the complex polarization structure of PWNe suggests that the magnetic field has no simple form (Bietenholz & Kronberg, 1991). Second, the production of detailed, synthetic synchrotron emission maps depends critically on having followed the evolution of the radiating particle species (Tregillis et al., 2001). Detailed knowledge of the magnetic field alone leaves one as far from being able to produce a robust estimation of the flow emissivity as one is with a purely hydrodynamic study. For all these reasons, a purely hydrodynamical initial study is warranted.

5.1 Setting Up the Pulsar Problem

5.1.1 Adaptive mesh setup

Recall from §3.2 the salient AMR parameters left to the choice of the user: the number of coarse grid cells, $\mathrm{N_c}$, the number of refinement levels, $\mathrm{L_{max}}$, the refinement factor, $\mathrm{N_r}$ for each coordinate direction (in this case, I use grid I & J corresponding to the axisymmetric coordinates ρ & $z \Rightarrow \mathrm{N_r I}$ & $\mathrm{N_r J}$), and the density change threshold

F_{TOL}. These three quantities are specified in the initial problem setup file. Based on Philip Hughes' work on relativistic galactic jets, I selected $F_{TOL} = 0.005$ for all levels, meaning that 0.5% of the largest difference in density between adjacent cells in all meshes at a given level is sufficient to invoke refinement for the cell under consideration. Initial tests showed that this setting resulted in satisfactory flagging of areas of physical interest, i.e., shocks, a conclusion borne out by the significance of the results presented in §5.2. Future, more detailed studies may require a smaller value of F_{TOL}. I chose $N_c = 750 \times 200$, and the values of L_{max}, N_rI, and N_rJ as follows.

Computational expense scales rapidly with the number of refinement levels due to the exponential increase in the number of cells: each cell at level L is divided into $N_rI \times N_rJ$ refined cells at level L+1, and so a level 0 cell will have $(N_rI \times N_rJ)^L$ "daughter" cells at level L. Thus, the challenge is to minimize $(N_rI \times N_rJ)^{Lmax}$ while still obtaining a sufficiently detailed flow solution. Given its position in the exponent, minimizing L_{max} is of utmost importance. Thus, I selected $N_r = N_rJ = 4$ (based on Hughes' experience with relativistic galactic jets), and explored L_{max}. As shown in §5.2, one level of refinement is sufficient to produce sufficiently detailed results. From the experience of P. A. Hughes, there is known to be a critical resolution at which key structures of any flow suddenly appear. At lower refinement levels, the flow is amorphous. At higher levels, details improve somewhat, but the basic rarefactions and shocks are already captured at the critical level. As the simulation in §5.2 shows, $L_{max} = 1$ captures the key structures and the extent of the refined region is limited. It is noteworthy that adding a second level of refinement resulted in the run time ballooning by a factor of ~ 8.4 during the beginning stages (0 to 10,000 iterations) of the simulation shown in §5.2 without significantly changing the overall features of the flow solution. As the simulation advanced, the number of refined cells increased significantly, making 8.4 a lower bound (indeed, for the evolution stage of 20,000 to 30,000 iterations, the factor had already increased to 11.7).

5.1.2 Identifying suitable input parameters

I have implemented the refined primitives algorithm within the context of simulating the interaction of a light, fast pulsar wind with a dense, slow-moving ambient medium arising from the space velocity that is typical of pulsars (Cordes & Chernoff, 1998). This interaction gives rise to the classic structure of forward and reverse shocks separated by a contact surface (Weaver et al., 1977). This inquiry is motivated by the existence of asymmetric pulsar wind nebulae such as PSR1929+10 (Wang et al., 1993) and the Guitar nebula (Cordes et al., 1993, recall Figs. 1.4 & 1.6). In particular, Wang et al. (1993) proposed that the observed X-ray trail is due to a relativistic backflow opposite the motion of the pulsar. In this picture, the wind particles are blown behind the pulsar by the ram pressure of the ISM, and flow inside a tunnel along which pressure decreases rapidly leading to the acceleration of the wind particles to relativistic, supersonic velocities. As detailed in this chapter, my simulations have validated this scenario for realistic values of pulsar space velocities and wind Lorentz factors.

An initial state is specified through the unitless ambient-flow velocity, v_a, in units of the speed of light, Mach number, $\mathcal{M}$, and mass density, n_a, of the ambient medium, and the Lorentz factor, γ_o, pressure, p_o, and mass density, n_o, of the pulsar wind (or, more generally, the "outflow"). The ambient velocity flow arises from the space velocity of the pulsar, which is typically 400–500 km s^{-1} but is known to be as high as 1740 km s^{-1} (Chatterjee & Cordes, 2002). In order to cover typical to nonphysical yet bounding velocities, I use values in the range 500-5500 km s^{-1}, which implies v_a on the order 10^{-3}–10^{-2}. I further select values of $\mathcal{M}$ corresponding to ambient-medium sound speeds in the range 1–100 km s^{-1}. The value of n_a is arbitrary and n_o is scaled accordingly. Pulsar winds have bulk Lorentz factors up to order 10^6 and I consider $\gamma_o = 10^2$–10^6.

5.2 Application

5.2.1 Identifying suitable input parameters

The outflow streams relativistically into the ambient medium generating a strong shock. I derive a value for p_o from the assumption that the outflow is interacting with the ambient medium, requiring that the momentum flux be comparable on either side of this shock; if the fluxes were not comparable, then either the ambient flow or outflow would dominate and the problem would be uninteresting. The momentum flux of the non-relativistic ambient medium and ultra-relativistic outflow are, respectively:

$$\begin{aligned} F_{M,a} &= n_a v_a^2 + p_a, \\ F_{M,o} &= \gamma_o^2 (e_o + p_o) v_o^2 + p_o. \end{aligned}$$

For an ultra-relativistic outflow, $p_o \gg n_o \Rightarrow e_o \rightarrow 3p_o$, and $v_o \rightarrow 1$, and, for the ambient medium, $n_a v_a^2 \gg p_a$. Applying these conditions, and noting that $\gamma_o^2 p_o \gg p_o$, gives:

$$p_o \sim n_a \left(\frac{v_a}{2\gamma_o} \right)^2 \sim 10^{-19} \; for \; \gamma_o = 10^6, \; n_a = 1.$$

I am then free to pick any n_o meeting the conditions of a light, relativistic outflow, i.e., $n_a, \; p_o \gg n_o$. I select $n_o = 10^{-l} p_o$, $3 < l < 6$. This clearly satisfies $p_o \gg n_o$ and one may verify it satisfies $n_a \gg n_o$ by noting that the equation for p_o implies $n_a \gg p_o$ since $\gamma_o^2 \gg v_a^2$ for the flows of interest here.

5.2.2 A relativistic backflow

Fig. 5.1 shows a simulation of a $\gamma_o = 10^5$ outflow interacting with an ambient flow with velocity $v_a = 0.00583$ (1750 km s^{-1}). The outflow pressure was calculated for an ambient-flow velocity of 500 km s^{-1} in order to match the typical value for pulsars in general. The outflow originates inside the circular region to the left of the evolving structure and the ambient flow streams in along the left edge of the computational

domain. Fig. 5.3 shows the limited extent of the refined grid, supporting the choice of $L_{max} = 1$. Recall the Hα image of the Guitar Nebula (see Fig. 1.4), a well-known pulsar wind nebula with the most rapidly moving pulsar ever observed, with a transverse velocity of $(1.7\pm0.4)\times10^3$ km s^{-1} (Chatterjee & Cordes, 2002). The simulation qualitatively resembles the nebula. This result constitutes compelling motivation for the conclusion that interstellar-medium flows set up by the space motion of pulsars can indeed produce "cometary" nebulae.

I believe this simulation to be the first demonstrating asymmetry arising from a spherically-symmetric, light, ultra-relativistic flow interacting with a dense, slow ambient flow. The lines labeled "1" and "2" on the density map in Fig. 5.1 mark 1-dimensional cuts (hereafter "cut-h1"and "cut-h2", respectively) made to probe the state of the simulation. Cut-h1 spans the entire structure while cut-h2 spans the interior space occupied by the pressure enhancements clearly visible in the pressure map. Figs. 5.2a & 5.2b show the values of the flow parameters along these cuts. These plots clearly show the outer bounding shockwave represented by the red boundary in the density map as well as a series of weaker internal on-axis shocks visible in the pressure map. The x-component of the flow velocity shows that a relativistic back flow harboring a series of weak shocks has arisen down stream. This validates the interpretation by Wang et al. (1993) of the origin of the X-ray trail behind PSR1929+10, and demonstrates the ability of the refined solver to elucidate the internal structure of diffuse, ultra-relativistic pulsar wind nebulae which is often difficult to observe directly.

It is noteworthy that the termination shock of the wind is not evident in the simulation discussed above. This is due to numerical shocking of the wind as it emerges from the on-axis hemisphere, as follows. Consider the cells depicted in Fig. 5.4. Let the angle of the line connecting the center of the hemisphere and the center of a cell 1, 2, 3, or 4 be θ_i, $i = 1, 2, 3, 4$. Since I have taken the pulsar wind to be spherically

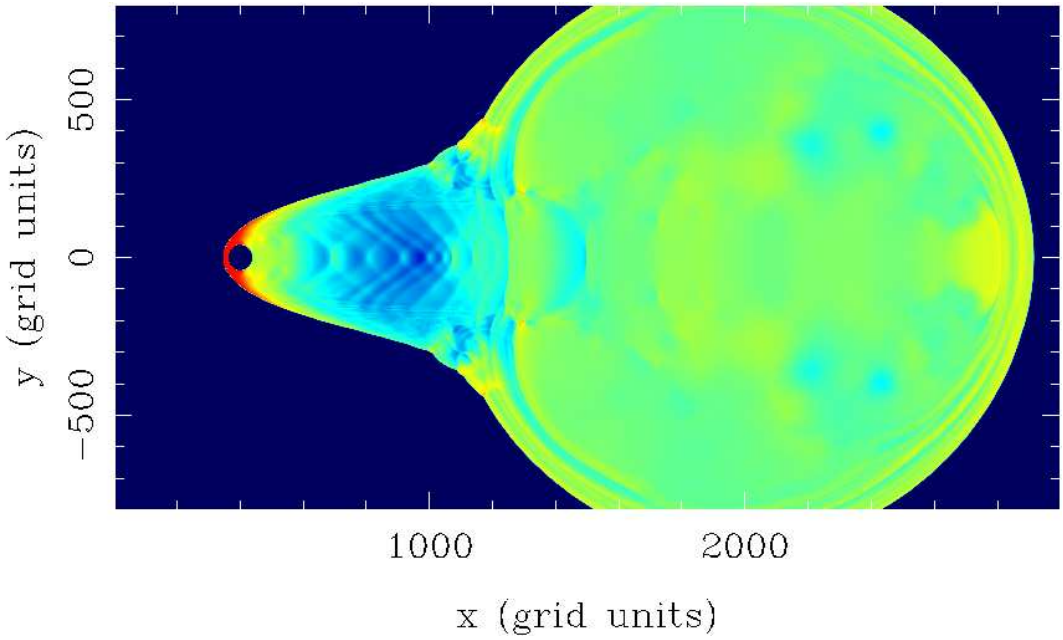

(a) Exponential pressure map.

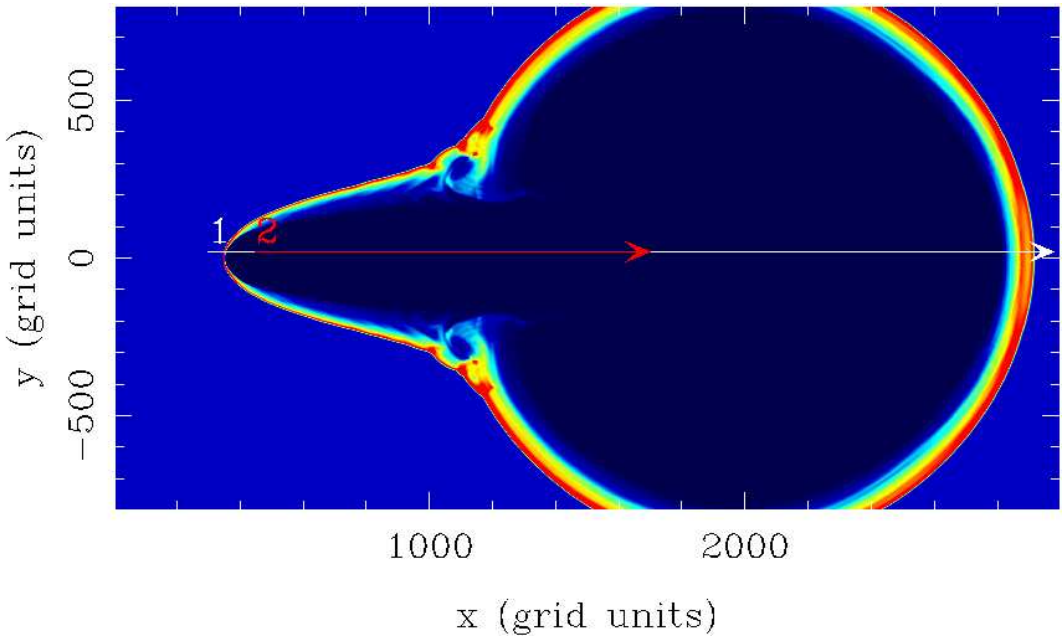

(b) Linear laboratory-frame mass density map.

Figure 5.1: An 871,200-iteration simulation of a light, ultra-relativistic outflow interacting with a dense, slow ambient flow. The input parameters are: $v_a = 0.00583$ ($\Rightarrow$ 1750 km s^{-1}), $\mathcal{M} = 300$, $n_a = 1$, $\gamma_o = 10^5$, $p_o = 7{\times}10^{-16}$, and $n_o = 10^{-3} p_o$. The upper (lower) panel shows an exponential (linear) color map of the rest-frame pressure (laboratory-frame mass density). Both have been reflected along the symmetry axis. The outflow originates within the circular region to the left of the evolving structure and the ambient flow streams in along the left edge of the domain. The lines labeled "1" and "2" are 1-D data cuts (hereafter "cut-h1"and "cut-h2", respectively) with flow parameters plotted in Figs. 5.2a & 5.2b. See http://ustw.info/dissertation/figures for a high-quality electronic version.

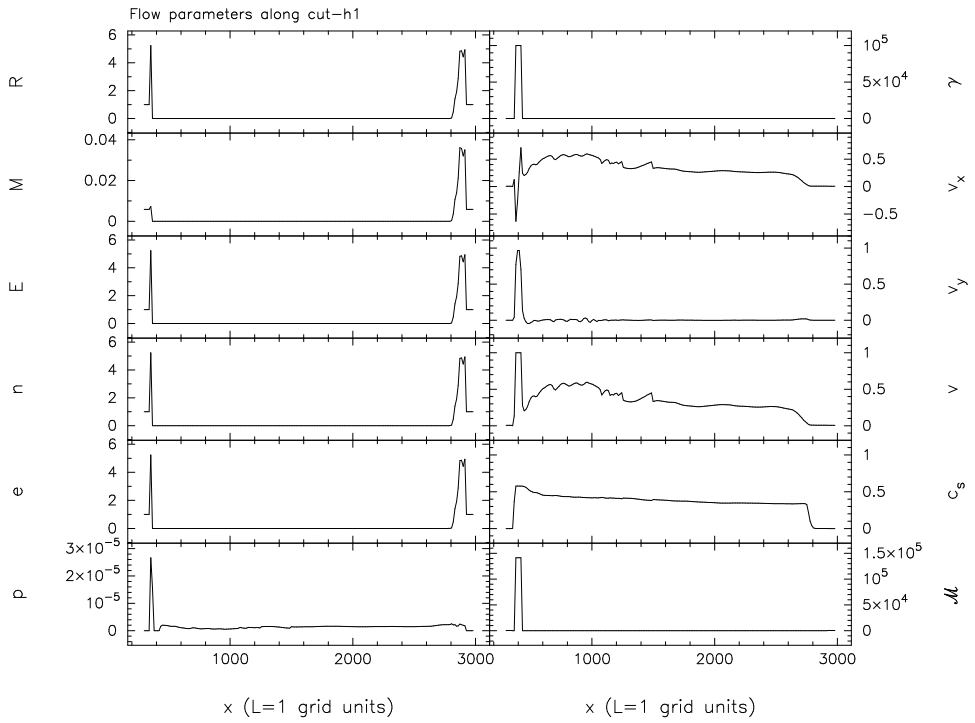

(a) Flow parameters along cut-h1.

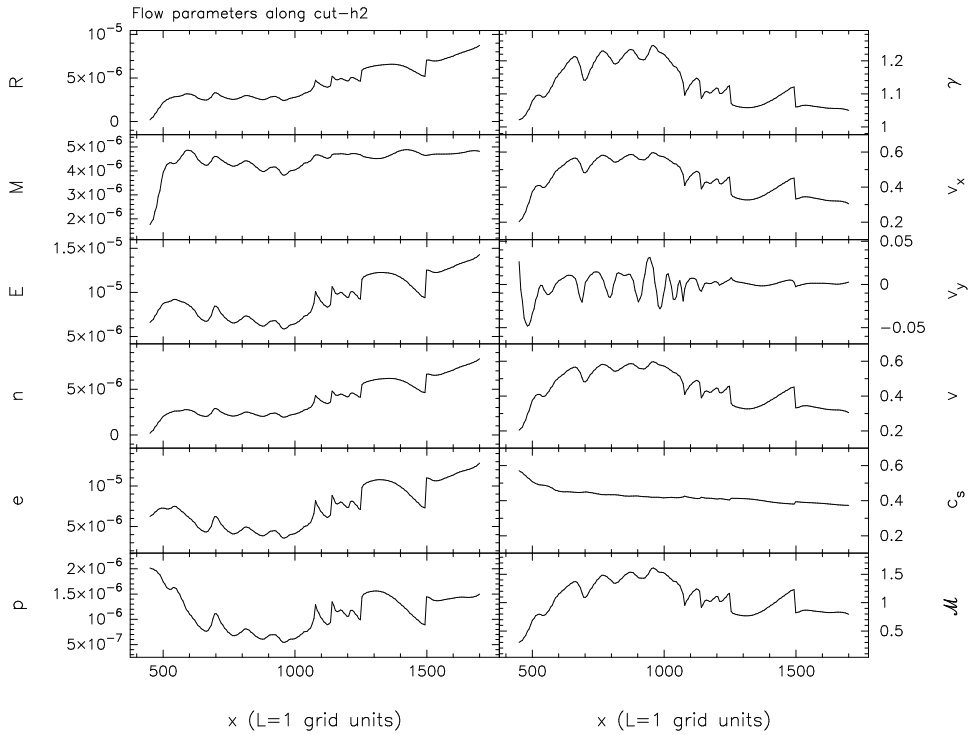

(b) Flow parameters along cut-h2.

Figure 5.2: The run of the laboratory-frame mass (R), momentum (M), and total energy (E) densities, rest-frame mass (n), and total energy (e) densities, and pressure (p), Lorentz factor (γ), x- and y-components of the flow velocity (v_x, v_y), the flow velocity (v), sound speed (c_s), and generalized Mach number ($\mathcal{M}$) along (a) cut-h1 and (b) cut-h2 in Fig. 5.1.

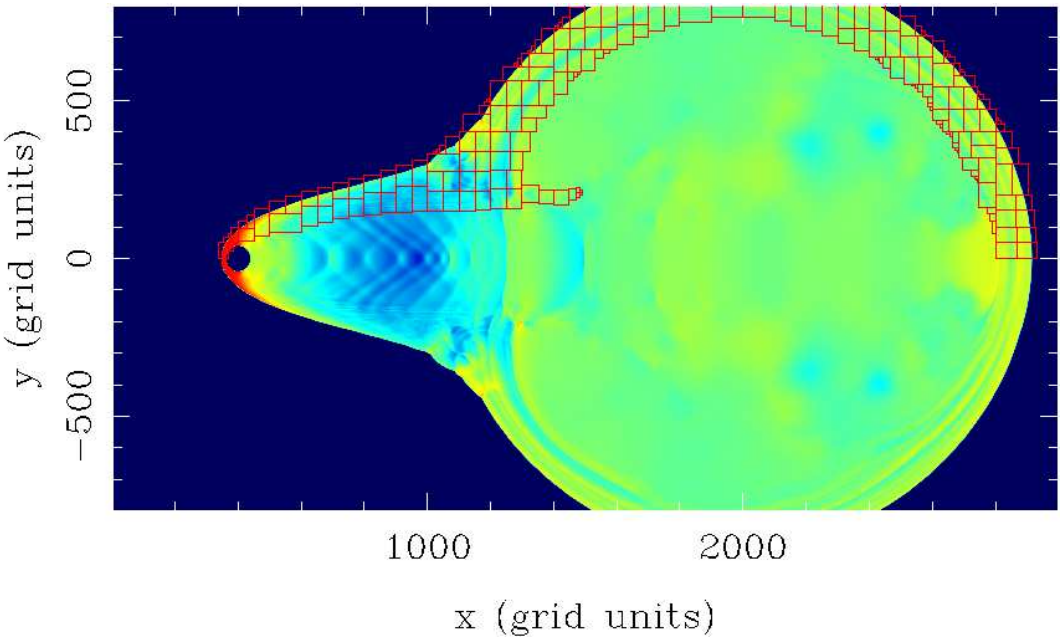

Figure 5.3: Plotted in red overlaying the pressure map for the simulation shown in Fig. 5.1 is the refined grid at level L=1. The bottom half of the map is a reflection of the top half and has the same refined grid even though it is not shown. Note that the red lines trace the outlines of the meshes of refined cells, but not the cells themselves. While the boundary shock is well-refined, the axial shocks within the nebula are not refined at all. Flagging is determined by TOL = FTOL(L)*TESTFMAX, where TESTFMAX is the largest difference in R between adjacent cells for all cells at level L. I suspect that refinement follows only the boundary shock because R differences inside the nebula are small compared to the difference between the nebula and the ambient medium. I will investigate refinement flagging in more detail as a follow-up to this dissertation. See http://ustw.info/dissertation/figures for a high-quality electronic version.

symmetric as it emerges from the hemisphere, I may calculate the relative flow velocities Δv_{12} and Δv_{34} (normalized to the speed of light) at the centers of cells 1 & 2 and 3 & 4:

$$\begin{aligned}
\Delta v_{12} &= \sqrt{\left(\frac{\cos\theta_1 - \cos\theta_2}{1 - \cos\theta_1\cos\theta_2}\right)^2 + \left(\frac{\sin\theta_1 - \sin\theta_2}{1 - \sin\theta_1\sin\theta_2}\right)^2} \\
&\approx 0.80, \\
\Delta v_{34} &= \sqrt{\left(\frac{\cos\theta_3 - \cos\theta_4}{1 - \cos\theta_3\cos\theta_4}\right)^2 + \left(\frac{\sin\theta_3 - \sin\theta_4}{1 - \sin\theta_3\sin\theta_4}\right)^2} \\
&\approx 0.03.
\end{aligned}$$

This shows that the relative velocity between vertically adjacent on-axis cells just outside the hemisphere is supersonic relative to the pulsar outflow sound speed of 0.57 (for the parameters relevant to Fig. 5.1). Thus, the wind near the axis shocks immediately and is thermalized, producing a post-termination-shock flow. Given that at early times the wind shows no deviation from spherical symmetry, it is clear that this asymmetric numerical shocking of the wind is smeared out by the interaction with the ambient flow and does not impact the global evolution of the simulation.

Additional levels of refinement, perhaps needed only at early simulation times, will mitigate the numerical shocking issue. However, since tests have shown this immediate shocking is present for $L_{max} = 2$, and the significant results discussed below were possible with $L_{max} = 1$, explorations of higher numbers of refinement levels are left to future studies. When these higher refinement-level studies result in unshocked wind flows with ultra-relativistic Lorentz factors entering the computational domain, and the resolution of the termination shock, I will perform new shock-tube tests. However, while the refined REST_FRAME routine is essential for proper handling of the $\gamma >> 1$ outflow, in the simulations presented here, there are no structures involving Lorentz factors higher than those previously explored by Duncan & Hughes (1994) & Hughes et al. (2002) with the RHLLE solver. All structures referenced

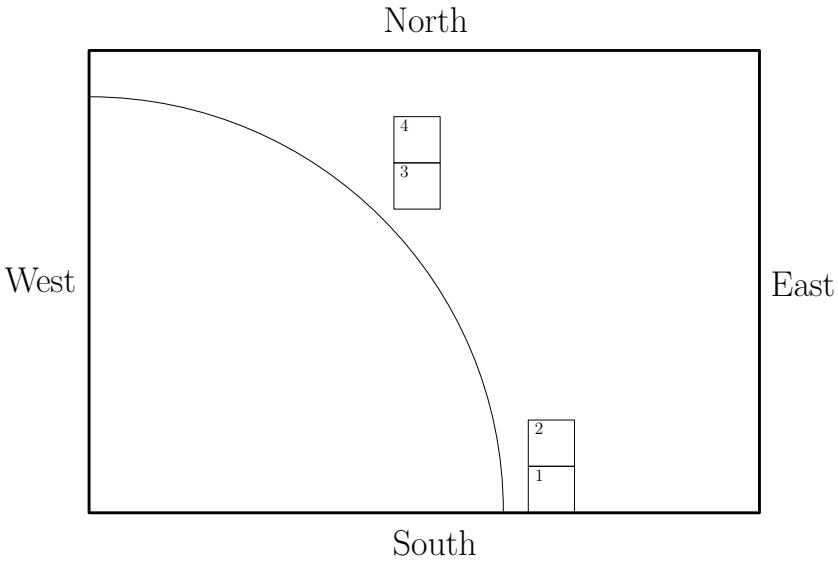

Figure 5.4: Schematic showing the geometric layout of the cells discussed in regards to numerical shocking of the pulsar wind. The arc represents the on-axis hemisphere with radius 37.5 fine cells. Cell 1 is on-axis and is centered at 41.5 fine cells from the center of the hemisphere (relative center coordinates (x,y) = (41.5,0.5). The center coordinates of cells 2, 3, and 4 are (41.5,1.5), (29.5,29.5), and (29.5, 30.5) respectively.

below originated in the computational domain where the the tried-and-true Newton-Raphson iterative solver was toggled into action (recall §4.2). Therefore, I proceed with firm confidence rooted in the previous shock-tube tests (recall the introduction in Chap. 3).

5.3 Discussion

The physics behind the formation of the structure observed in Fig. 5.1 is as follows. The wind streams outward and sweeps up ambient material which drives pressure waves (weakly at first) into the shocked wind. As the nebula expands, the pressure inside decreases. Once enough material has accumulated, an inflection point develops in the boundary of the nebula along the leading edge at approximately 45° from

the axis as measured from W to N[1], intensifying the pressure waves. See Figs. 5.5 & 5.6 for a sequence of pressure maps showing the time development of the simulation shown in Fig. 5.1 with particular attention given to the inflection point. The pressure waves propagate to the axis and reflect, leading to the formation of a relativistic backflow harboring internal shockwaves reminiscent of shock diamonds (Fig. 5.7 shows an Earthly example). The fact that the backflow does not develop until after the inflection point supports this picture. The internal shockwaves, in turn, thermalize energy, allowing the flow to expand and inflate the trailing spherical bubble. As the bubble inflates, it "pinches" the inflection point enhancing the cuspy shape, maintaining the pressure-wave influx that sets up the energy-thermalizing backflow responsible for inflating the bubble. The Guitar pulsar was not born at the center of the trailing bubble: given its proper motion, the pulsar moves a distance corresponding to the entire nebula in less than 500 yr (Romani et al., 1997), a time orders of magnitude too short for the age of a pulsar powering a bow-shock nebula. However, such a feedback cycle is relevant to the Guitar nebula because it explains how the bubble persists. Such a scenario is analogous to the formation of structure in relativistic galactic jets, where the evolution is driven by Kelvin-Helmholtz modes along the contact surface that separates the shocked ambient medium from the shocked jet material (e.g., Hughes et al., 2002).

In order to closely simulate realistic conditions, I performed the run with a $\gamma_o = 10^5$ outflow (closer to the canonical value of 10^6) interacting with an ambient flow with velocity $v_a = 0.00583$ (1750 km s^{-1}; representing the Guitar pulsar). The evolution of the Guitar-like shape is rather sensitive to the choice of parameters. As Tab. 5.1 shows, the appearance of the inflection point marking the onset of the formation of the "neck" of the Guitar takes a significantly larger number of computational iterations as

[1]This is sensible as it is the location where the wind velocity transitions from having its largest component at 180° to the inflow direction to having it at 90°.

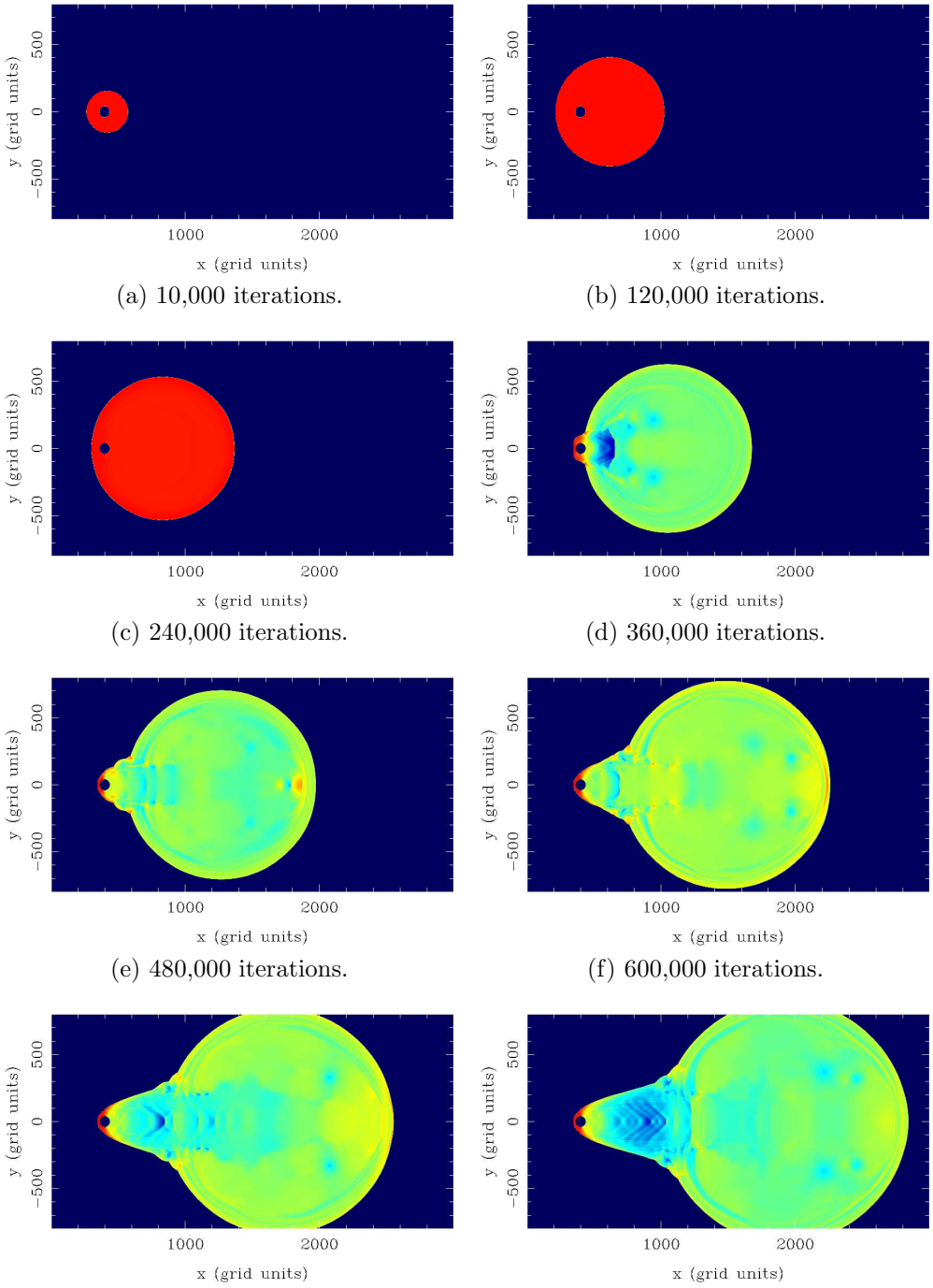

(a) 10,000 iterations.

(b) 120,000 iterations.

(c) 240,000 iterations.

(d) 360,000 iterations.

(e) 480,000 iterations.

(f) 600,000 iterations.

(g) 720,000 iterations.

(h) 840,000 iterations.

Figure 5.5: A time sequence of exponential pressure maps for the simulation shown in Fig. 5.1. The sequence shows that the appearance of the inflection point is preceded by a pressure drop inside the nebula. I show a sequence of finer time steps between panels c) and d) (240K – 360K iterations) in Fig. 5.6. Note that the color map is relative to the minimum and maximum for each plot individually. However, the minimum is the same and the maximum is similar for all plots, so the variation is minimal. See http://ustw.info/dissertation/figures for a high-quality electronic version.

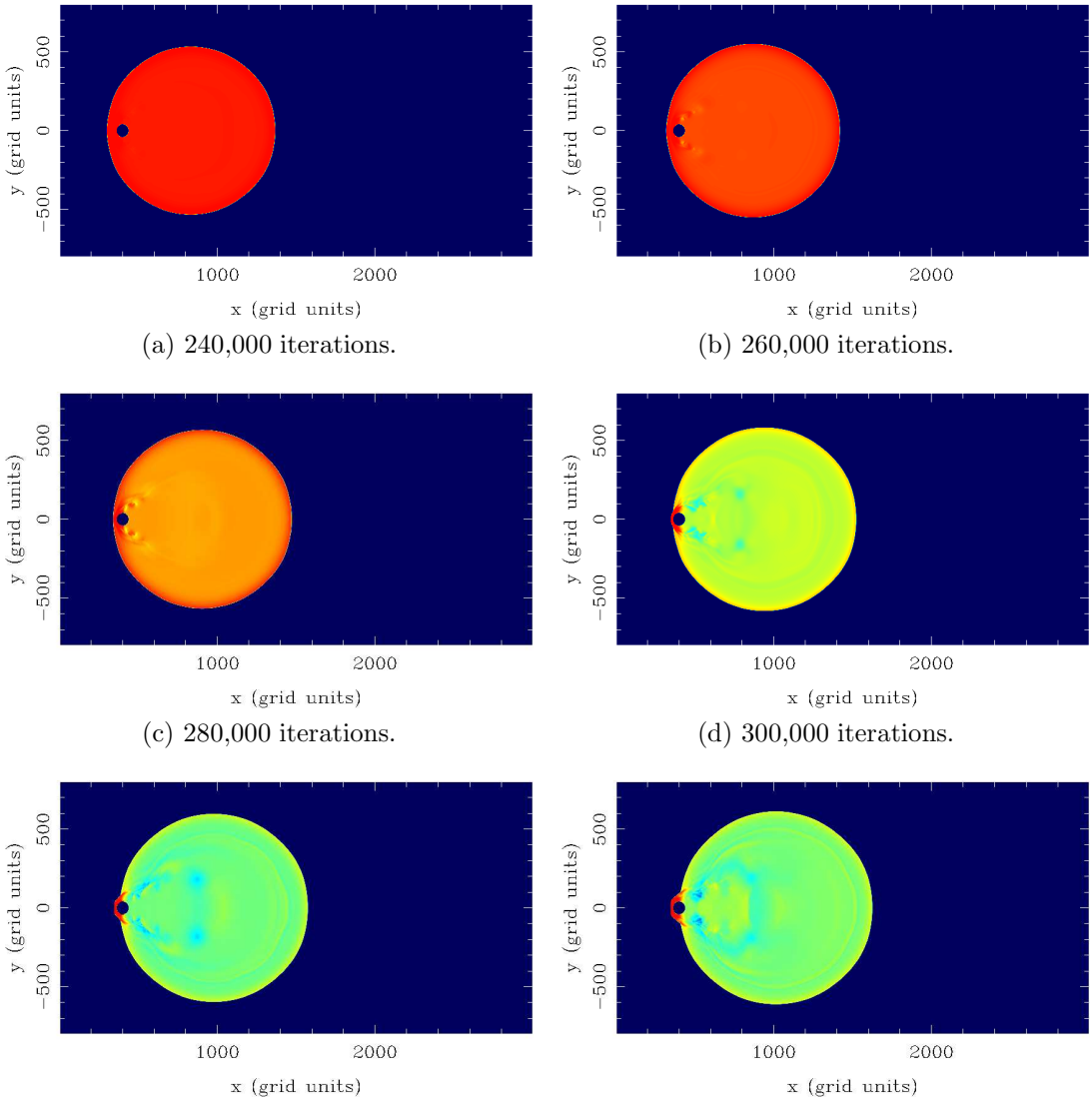

(a) 240,000 iterations.

(b) 260,000 iterations.

(c) 280,000 iterations.

(d) 300,000 iterations.

(e) 320,000 iterations.

(f) 340,000 iterations.

Figure 5.6: A time sequence of exponential pressure maps for the simulation shown in Fig. 5.1. This a finer sequence of time steps showing the appearance of the inflection point in more detail. Note that the color map is relative to the minimum and maximum for each plot individually. However, the minimum is the same and the maximum is similar for all plots, so the variation is minimal. See http://ustw.info/dissertation/figures for a high-quality electronic version.

Figure 5.7: Shock diamonds in the exhaust of the SR-71 Blackbird. Credit: NASA.

the ambient-flow velocity decreases. This is expected as the asymmetry of the nebula should evolve more slowly in this scenario: as the ambient-flow velocity decreases, it takes more time for enough ambient material to be swept up for the neck to start forming. Exploratory simulation runs show a similar behavior as the Lorentz factor of the wind increases: raising γ_o by a factor 10 means lowering the wind pressure by a factor of 10^2 in order to preserve the momentum-balance condition given by Eqn. 5.1.[2] Thus, the wind progresses into the ambient medium more slowly and, once again, it takes longer for sufficient ambient material to be swept up. If a pulsar velocity of 1500 km s^{-1}, 1250 km s^{-1}, or 1000 km s^{-1} is required for Guitar-like morphology to arise, then the velocity distribution of Arzoumanian et al. (2002) imply <5%, 7-8%, or ∼15% of radio pulsars, respectively, have the possibility of developing such features depending on the nature of their ambient environment.

[2]The outflow pressure was calculated for an ambient-flow velocity of 500 km s^{-1}.

Table 5.1: The dependence of the Guitar-like inflection point on the number of iterations. As expected, the higher the ambient-flow velocity, the sooner the inflection point develops due to the increased rate at which ambient material is swept-up.

Wind Lorentz factor (unitless)	ambient-flow velocity (km s^{-1})	Iterations until inflection (10^4)
10^5		
	1750	30
	1500	39
	1250	54
	1000	81
	750	unseen at 90
10^4		
	5500	4
	4250	6
	3000	12
	1750	30

5.4 Summary

I have applied the refined solver to an ultra-relativistic problem and have shown that it is capable of reproducing observed structures. In particular, a $\gamma_o = 10^5$, $v_a = 0.00583$ (1750 km s^{-1}) simulation shows a morphology strikingly reminiscent of the Guitar nebula. While I have not demonstrated how the Guitar nebula formed, I have motivated how its morphology persists. The simulation also shows that for a realistic pulsar velocity, a relativistic, on-axis backflow harboring a series of internal shocks developed, validating the origin of the X-ray trail behind PSR1929+10 proposed by Wang et al. (1993). In addition, I have shown that the evolution of observed structures is rather sensitive to the choice of input parameters. This justifies a concerted future effort to completely sample input parameter space in order to discover precisely under what conditions prominent asymmetry forms. Of particular interest will be the lowest ambient-flow velocity, and most extreme density mismatch between the wind and ambient medium, for which Guitar-like morphology arises.

CHAPTER 6

Modeling Shock Acceleration and Synchrotron Cooling of Particles in Pulsar Winds

The purely hydrodynamic model of pulsar wind nebulae discussed to this point has been successful in shedding light on the global properties of PWNe. Considerable advancement of this model is readily attainable, without making the substantial jump to magnetohydrodynamic simulations, by taking into account two linked effects: 1) the acceleration of particles, i.e, the generation of cosmic rays at PWNe shocks and 2) the radiative loss of energy, i.e., cooling via synchrotron emission. Taking these effects into consideration will have a substantial impact on the simulation results as the strength of the shocks will be modified due to the fact that they will become radiative. This, in turn, will impact the nebular backflow and the evolution of the bubble. For example, in the extreme case of dominance of synchrotron losses, the morphology of the nebula will be radically changed as energy is sapped from the system. Thus, an interesting test will be how much synchrotron loss the wind can bear before bubble formation falters.

Understanding the acceleration of particles at shocks within PWNe is important because it may lead to an explanation of the γ-ray emission now known to be a ubiquitous feature of these objects. The Crab has long been known to produce γ-rays (e.g., Jung, 1989), and there has been a recent explosion in the literature of claims associating other PWNe with γ-ray sources. In fact, Horns et al. (2007) has characterized PWNe as appearing to be a dominant source population for very high energy γ-rays. I approach this problem as follows. Cosmic-rays (CRs; Millikan, 1925)

are charged particles that strike Earth's atmosphere with energies up to 10^{21} eV. The CR spectrum (see Fig. 6.1) is a broken power-law that steepens near 3×10^{15} eV and flattens near 3×10^{19} eV (the so called "knee" and "ankle" representing a shift to a decrease and increase in the number of particles, respectively, at subsequent energies). SNRs have long been thought to be sources of CRs (e.g., Chevalier et al., 1976; Uchiyama et al., 2007) up to the knee. However, direct, convincing evidence has yet to be obtained (Ellison & Cassam-Chenaï, 2005). Whether or not PWN shocks are important in CR generation, and play a role in the production of CRs above the knee, is an open question. If PWN/SNR systems do produce such CRs, their significantly higher energy relative to CRs below the knee will result in γ-ray emission.

While elucidating the origin of CRs is certainly of great interest, the primary focus of this work, at least in the early stages, is the exploration of the effects of cooling on PWN morphology. The energy invested in CR generation, whether above or below the knee, is ultimately lost from the system, leading to a direct morphological influence. Thus, fleshing out the role of PWNe shocks in the acceleration of charged particles is germane to understanding nebular cooling. But how does the energy loss arise? Magnetic fields accelerate charged particles giving rise to synchrotron radiation, for relativistic particle motions, and cyclotron radiation, for non-relativistic motions. In addition to having relativistic bulk velocities, the particles comprising pulsar winds have thermal motions that are sufficient to produce synchrotron emission and, given the presence of the neutron star's strong magnetic field, synchrotron cooling is undoubtedly of importance in pulsar wind systems. The ubiquitous power-law spectrum exhibited by PWNe validates this picture. Thus, the inclusion of synchrotron cooling is a critical step in moving toward producing a realistic PWNe model, the development of which, as stressed by Bucciantini (2002), is crucial to the interpretation of observational data (such as the MSH 11–6*2* observations presented in Chap. 2). By

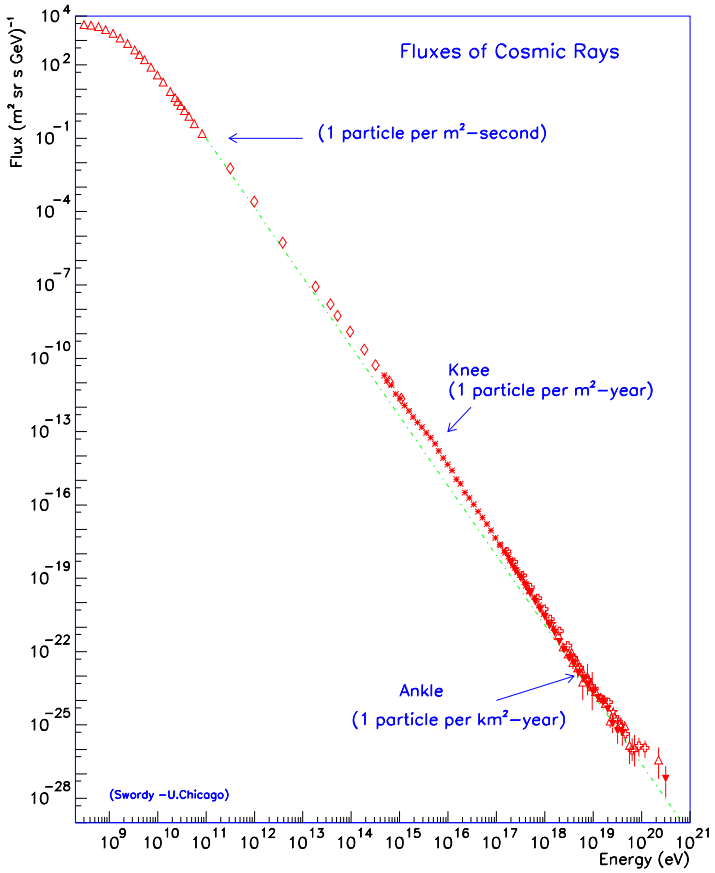

Figure 6.1: The spectrum of cosmic rays. Credit: unknown (downloaded from: http://astroparticle.uchicago.edu).

applying the AMR code to these issues, I can address fundamental questions about the origin of cosmic rays and PWN cooling and, therefore, the energetics of the ISM.

6.1 Physical Framework

6.1.1 The first-order Fermi process

In order to explain the origin of cosmic rays, Fermi (1949) proposed what has come to be known as Fermi acceleration. The basic principle is that charged particles can be reflected by moving interstellar magnetic fields, or "magnetic mirrors". The relative motion of the particle and the field determine if the particle gains energy (if the

particle is approaching the field) or looses it (if receding). Fermi argued that, while the motion of particles is random, the former scenario is more likely, on average, and that the net change in energy is positive. One problem with this model is that it is quite inefficient, so that particles take a long time to reach cosmic-ray energies.

Subsequently, supernova remnants were theorized (Shapiro & Silberberg, 1977) to house very efficient Fermi acceleration sites because the particle motions are not random. If a particle crosses a shock it gains energy, is scattered back across the shock by inhomogeneities in the magnetic field, is scattered again, re-cross the shock, and so on. Each time the particle crosses the shock, it gains energy, and thus can be accelerated to cosmic-ray energies very efficiently. This has come to be known as *first-order* Fermi acceleration (see, e.g., Rieger et al., 2007; Kato & Takahara, 2003; Berezhko & Ellison, 1999), as the mean energy gain per bounce is linearly dependent on the shock velocity. In Fermi's original mechanism, the mean energy depends on the square of the mirror velocity, and is therefore called *second-order* Fermi acceleration.

6.1.2 Physical sink and source terms

In order to model shock acceleration and synchrotron cooling, I define a species of passive tracer "particles" that are coupled to the hydrodynamic flow. These are passive particles in the sense that they are introduced via two new evolved variables, the laboratory-frame tracer mass and total energy density (R_{tr} and E_{tr}, respectively), and two new physical source terms, $S_{shock} > 0$ and $S_{sync} < 0$. With these defined, the evolved-variable, flux, and source vectors (recall Eqn. 3.1) become:

$$\begin{aligned} U &= (R, M_\rho, M_z, E, R_{tr}, E_{tr})^T, \\ F^\rho &= (Rv^\rho, M_\rho v^\rho + p, M_z v^\rho, (E+p)v^\rho, R_{tr}v^\rho, (E_{tr}+p_{tr})v^\rho)^T, \\ F^z &= (Rv^z, M_\rho v^z, M_z v^z + p, (E+p)v^z, R_{tr}v^z, (E_{tr}+p_{tr})v^z)^T, \\ S &= (0, p/\rho, 0, 0, 0, S_{shock} - S_{sync})^T, \end{aligned} \tag{6.1}$$

which are evolved via the Euler equations (recall Eqn. 3.2):

$$\frac{\partial U}{\partial t} + \frac{1}{\rho}\frac{\partial}{\partial \rho}(\rho F^{\rho}) + \frac{\partial}{\partial z}(F^{z}) \;\; = \;\; S.$$

The tracer pressure is given by the ultra-relativistic equation of state $p_{tr} = (1/3)e_{tr}$, where e_{tr} is the rest-frame tracer total energy density. This assumes that the tracer adiabatic index has the relativistic value 4/3 and that $e_{tr} >> n_{tr}$, where n_{tr} is the rest-frame tracer mass density.

As a simple first approximation, I take the particle energy gain from Fermi acceleration to be a constant: $S_{shock} = \Delta E_{shock} =$ constant. Such acceleration to a mono-energetic distribution is overly simplistic. In reality, cooling of pulsar winds is thought to arise from a population of particles Fermi-accelerated (e.g., Berezhko & Ellison, 1999) into a power-law distribution, and so I will adopt such a prescription in future studies. In general, the rate of energy loss via synchrotron radiation increases as the square of the energy times the magnitude of the magnetic field. Thus, I take the synchrotron source term to be:

$$S_{sync} = C_{syn} \times \left(\frac{e_{tr}}{n_{tr}}\right)^{2} \times n^{2}, \tag{6.2}$$

where C_{syn} is a tunable proportionality constant, e_{tr}/n_{tr} is the energy density per particle, and I have taken the magnitude of the magnetic field to be proportional to the hydrodynamic mass density as the field is advected by the hydrodynamic flow and compressed at shockwaves.

6.2 Implementation in a Relativistic, Hydrodynamic Code

Tracer code is implemented in the problem setup file, the hemispherical pulsar outflow routine, and in the axisymmetric RHLLE solver as represented in the pseudo-code shown in §A.2 of the Appendix. In regards to the solver, I show only the coding relevant to the tracer source terms as the calculation of the tracer quantities for the

RHLLE fluxes mirror those for the hydrodynamic flow. I flag shocks by looking for specific jumps in the hydrodynamic mass density and concomitant pressure:

$$\begin{aligned} R_{\rm crit} &\equiv \frac{\Delta R}{R} \\ p_{\rm crit} &\equiv \frac{\Delta p}{p} \\ &= \frac{2\Gamma}{\Gamma+1}(\mathcal{M}^2_{\rm crit}-1) \\ \mathcal{M}^2_{\rm crit} &= \frac{2(R_{\rm crit}+1)}{2-R_{\rm crit}(\Gamma-1)}\,. \end{aligned} \tag{6.3}$$

I use the non-relativistic quantities since the results from Chap. 5 show that the wind component within the computational domain includes only post-shock flows that are barely relativistic. The difference, Δ, can be either temporal or spatial. The first case means comparing the mass density for a given computational cell at a given time step to the value at the previous time step. The second involves comparing the mass density for a given cell to the values in the adjacent cells (to the left and right and above and below). If conditions are met, the cell is flagged if it was not flagged previously (once a tracer encounters a shockwave, its energy is incremented only once for that particular shock in order to avoid runaway energization). I only flag for shocks by comparing the fully updated density and pressure (not half-step quantities – recall the update is a two-step process – see §3.1). This means checking either at the beginning of MESH_UPDATE before the half-step update or at the end after the full time-step update. The temporal case has the additional stipulation that the check must take place before the evolved quantities from two time steps previous are overwritten by the quantities from the last update. This is necessary because the evolved quantities for the previous time step are temporary variables and are not stored in the simulation output files. Thus, MESH_UPDATE has to be called before they are defined.

6.3 Application

6.3.1 Identifying suitable input parameters

I discussed input parameters for the purely hydrodynamic simulations in §5.2.1. In this section I consider the tracer case. The primary goal of this subsection of my work is to explore the interplay of the acceleration of particles at PWN shocks, and the subsequent loss of the gained energy via synchrotron radiation. Thus, it is important to match the strengths of these effects such that the timescale for the loss of energy is long enough to allow the change in the tracer energy to be sampled using a reasonable time between data output events during the simulation run.

For example, given initial values of $n = 1.0$, $R_{tr} = 0.01$, and $E_{tr} = 1.0$, the synchrotron source term has an initial value of $C_{syn} \times 10^4$ (recall Eqn. 6.2). Thus, for a simulation that needs to be run an order of 10^4 iterations, and for choices of S_{shock} $= 1.0$ and a 10^3-iteration data output interval, a sensible selection for C_{syn} is one that leads to a loss of $\Delta E_{tr} = 1.0$ in 10^4 iterations. This means $C_{syn} \sim 1.0/(10^4) \times 10^{-4} =$ 1.0×10^{-8}. Of course, such an estimate will need to be modified once a cooling enabled simulation run has progressed sufficiently for a relativistic backflow harboring internal shocks to developed, and the tracer energy and density changes at these shocks can be established.

The remaining parameter to set is the critical density change $R_{\rm crit}$. The Mach number of the shocks that are the object of study determine what value to choose. Recall the shocks within the relativistic backflow that I discussed in Chap. 5. Fig. 5.2b shows that the relevant Mach numbers are in the range 1.1 – 1.4 which straddles the border between transonic and supersonic shocks. This implies $0.175 \leq R_{\rm crit} \leq 0.725$.

6.3.2 Tracer-enabled simulations

Fig. 6.2 shows a 1200-iteration advancement of the simulation state 1200 iterations before that shown in Fig. 5.1 (i.e., both figures show the same simulation time).

Fig. 6.3 shows the hydrodynamic density map from Fig. 5.1 and the layout of the refined grid. Given the months-long time scale to run such a hydro simulation from the first iteration, I chose to start my investigation of tracer behavior from the evolved state of the pure hydro simulation. I converted the file by laying down an even distribution of tracers across the computational domain. Once evolution progresses, tracers enter with the hydro outflow originating inside the circular region to the left of the evolving structure and with the ambient flow streaming in along the left edge of the domain. Recall that the wind Lorentz factor and ambient-flow speed for the hydro component are $\gamma_o = 10^5$, and $v_a = 0.00583$ (1750 km s^{-1}). For the tracers, I chose $R_{\rm crit}$ = 0.15, initial energy and mass densities of E_{tr} = 1.0 and R_{tr} = 0.01, respectively, S_{shock} = 1.0, and $S_{sync} = 10^{-13}$ (constant) meaning cooling was effectively disabled. Test runs showed that temporal density and pressure checking for tracer acceleration led to incomplete flagging for shocks. I suspect the cause to be the fact that the time step is sufficiently fine such that temporal evolution is very slow. Thus, for the simulations discussed here, I employed spatial density and pressure checking.

I believe these to be the first simulations addressing shock acceleration and synchrotron cooling within the context of ultra-relativistic simulations of bow-shock PWNe. The lines labeled "1" and "2" on the density map in Fig. 6.2 mark 1-dimensional cuts (hereafter "cut-t1"and "cut-t2", respectively) made to probe the state of the simulation. Cut-t1 spans the entire structure while cut-t2 spans the interior space occupied by the tracer energy enhancements and density enhancements clearly visible in Fig. 6.2. Fig. 6.4 shows the values of the flow parameters along these cuts. Recall that while the hydrodynamic flow is not affected, the tracers are impacted by the hydro flow via the hydrodynamic flow velocity in Eqn. 6.1. The energization and mass buildup of tracers at shocks is clearly evident. Of particular note is the fact that the nebular hot spot shown in Fig. 6.2 corresponds to tracer energization comparable to that occurring at the boundary shock.

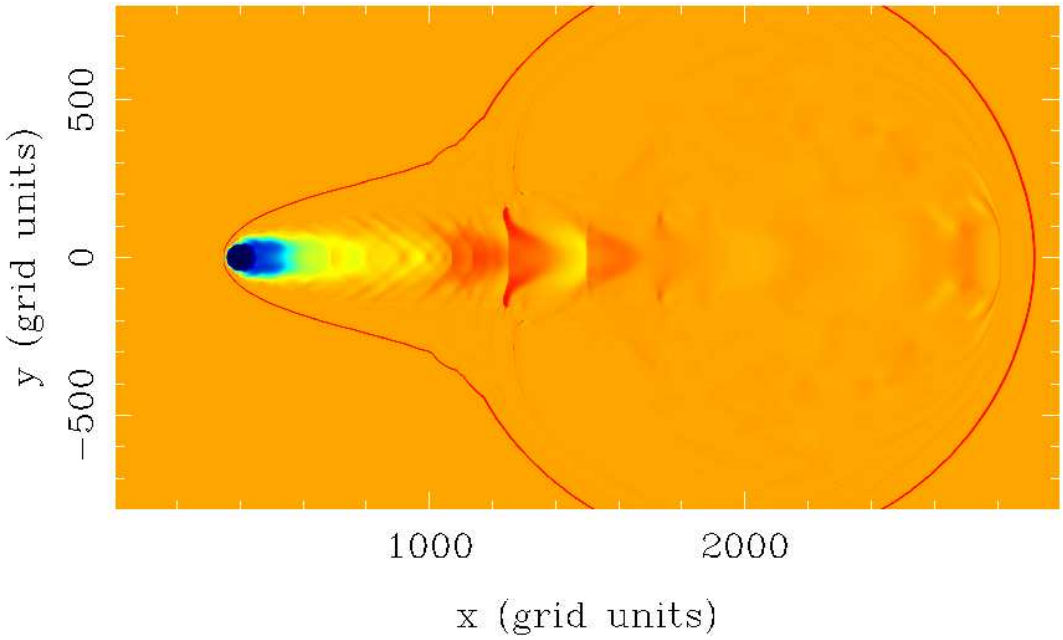

(a) Exponential tracer energy density map.

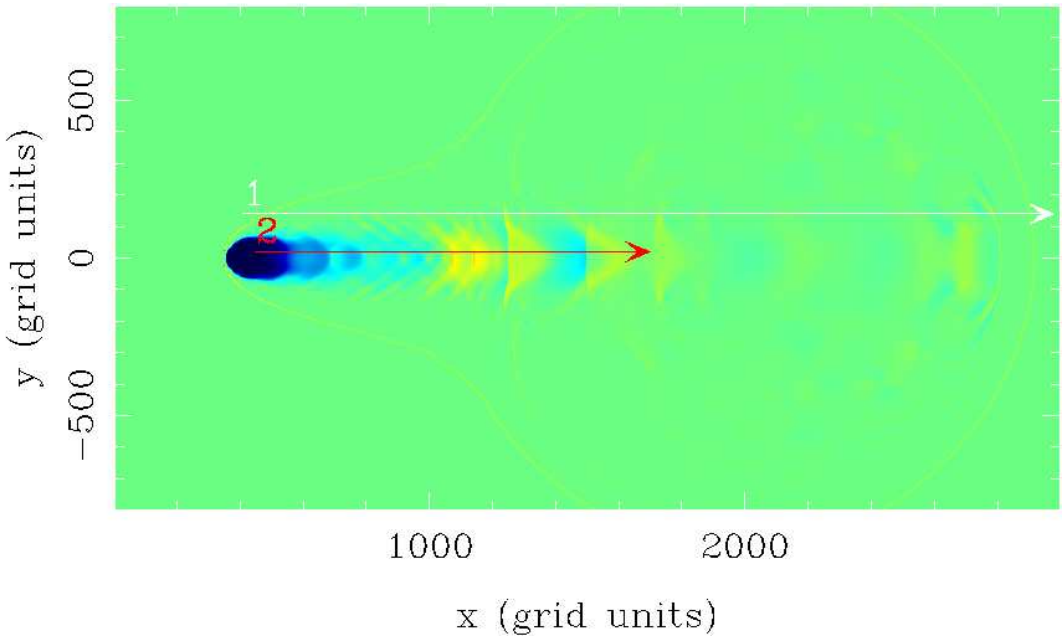

(b) Linear tracer mass density map.

Figure 6.2: An 1200-iteration run-on from an 870K-iteration, purely hydrodynamic simulation of a light, ultra-relativistic outflow interacting with a dense, slow ambient flow. The upper and lower panels show an exponential map of the laboratory-frame tracer energy density and a linear map of the tracer mass density, respectively (both reflected along the symmetry axis). The parameters are $R_{\rm crit} = 0.20$ ($\Rightarrow \mathcal{M}_{\rm crit} \approx 1.11$, $p_{\rm crit} \approx 0.28$), initial energy & mass densities $E_{tr} = 1$ & $R_{tr} = 0.01$, $S_{shock} = 1.0$, and $S_{sync} = 10^{-13}$ (constant; i.e., cooling effectively disabled). The lines labeled "1" and "2" are the 1-D data cuts (hereafter "cut-t1" and "cut-t2", respectively) with flow parameters plotted in Figs. 6.4. See http://ustw.info/dissertation/figures for a high-quality electronic version.

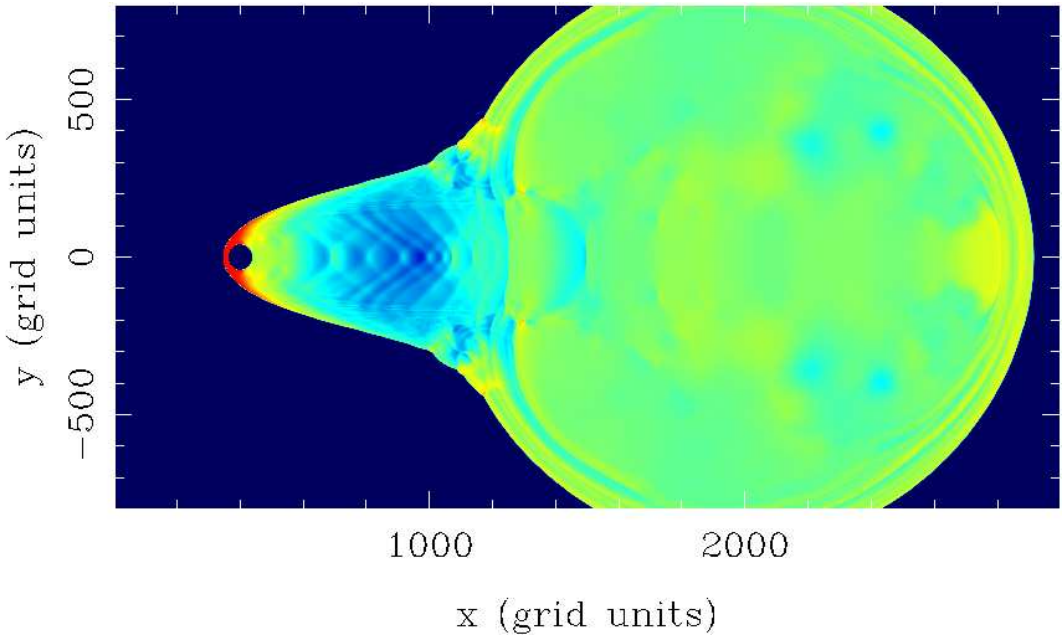

(a) Exponential hydrodynamic pressure map.

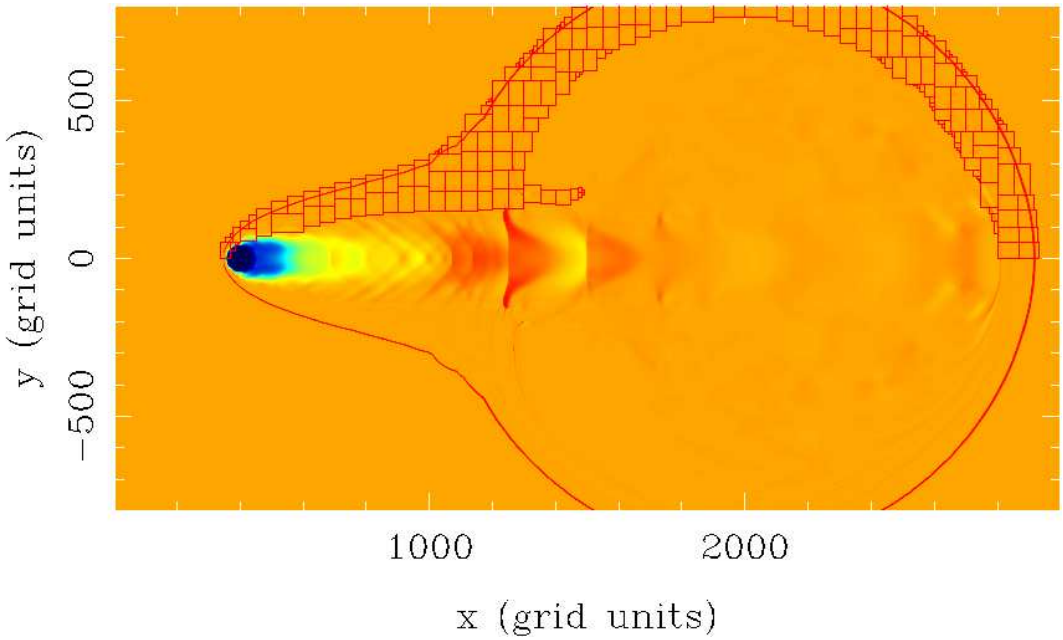

(b) Exponential tracer energy map with refinement grid overlaid.

Figure 6.3: Plotted are the hydrodynamic pressure map (above) and the refined grid at level L=1 in red overlaying the energy map (below) for the simulation shown in Fig. 6.2. The bottom half of the energy map has the same refined grid even though it is not shown. Note that the red lines trace the outlines of the meshes of refined cells, but not the cells themselves. See http://ustw.info/dissertation/figures for a high-quality electronic version.

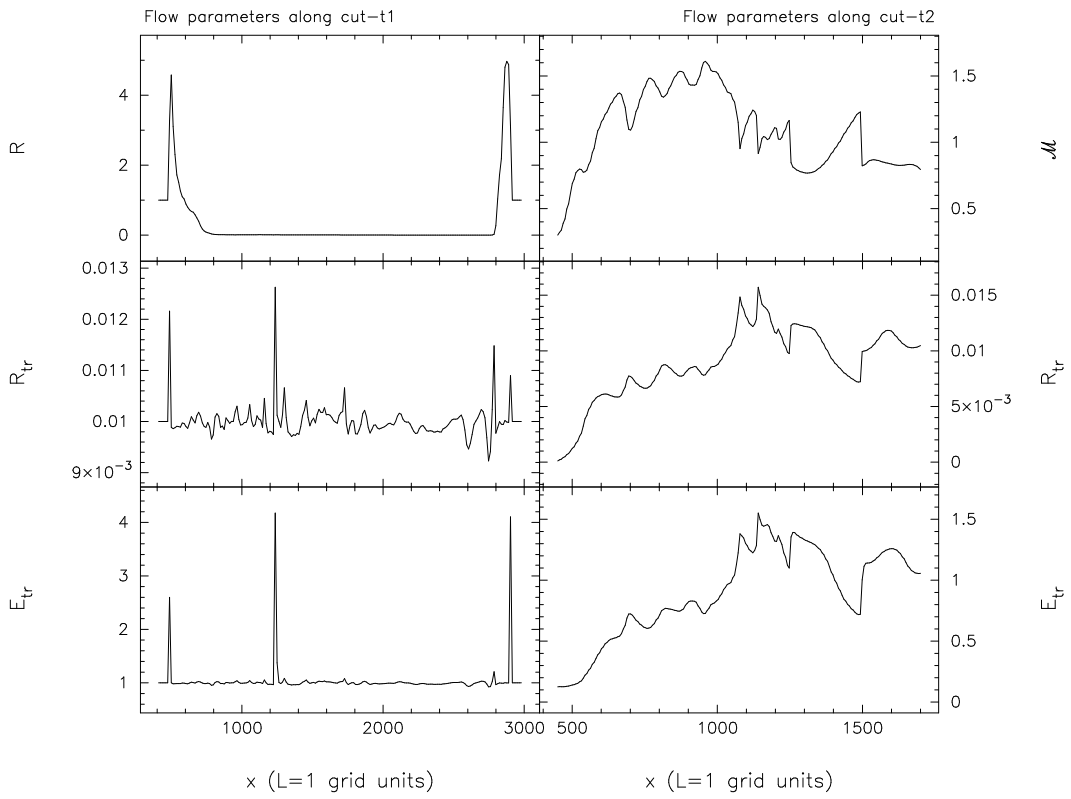

Figure 6.4: The run of the laboratory-frame hydrodynamic mass (R), laboratory-frame tracer mass density (R_{tr}), and total energy density (E_{tr}) along cut-t1 in Fig. 6.2 (left panels) and the generalized Mach number ($\mathcal{M}$), laboratory-frame tracer mass density (R_{tr}), and total energy density (E_{tr}) along cut-t2 in Fig. 6.2 (right panels). The plots clearly show that tracers are being energized at the boundary shock and nebular shocks confirming the action of the shock-acceleration source term. The middle peak in the tracer energy for cut-t1 corresponds to a nebular shock. Note that the energization is comparable to that associated with the boundary shock.

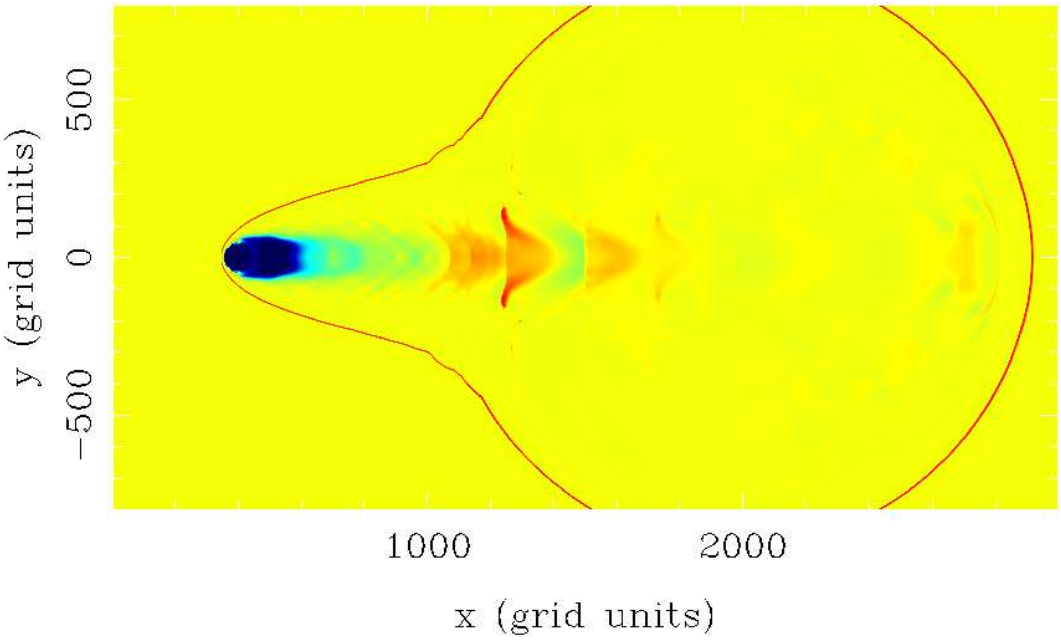

Figure 6.5: A 1200-iteration run-on from an 870K-iteration, purely hydrodynamic simulation of a light, ultra-relativistic outflow interacting with a dense, slow ambient flow. The 871,200-iteration stage for the hydro flow is shown in Fig. 6.3. Shown is an exponential map of the laboratory-frame tracer energy density (reflected along the symmetry axis). The parameters are $R_{\rm crit} = 0.20$, initial energy & mass densities of $E_{tr} = 1$ & $R_{tr} = 0.01$, $S_{shock} = 1.0$, and $S_{sync} = 0.001$ (constant). Flow parameters along the same cuts as cut-t1 & cut-t2 (from Fig. 6.2) are plotted in Fig. 6.6. See http://ustw.info/dissertation/figures for a high-quality electronic version.

In order to assess the synchrotron source term, I ran a simulation with parameters matching those for the simulation shown in Fig. 6.2 with the exception that I set $S_{sync} = 0.001$. I chose this value to produce significant energy loss on the order of 1000 iterations. Fig. 6.5 shows a 1200-iteration advancement of the simulation state 1200 iterations before that shown in Fig. 5.1. Fig. 6.6 shows the values of the flow parameters along the same cuts as cut-t1 and cut-t2. Energy loss from the source term is clearly evident. So too is the fact that tracers energized by the boundary and nebular shocks have retained more energy than those in the ambient medium. Balancing these two effects will be critical to meaningfully probing PWN cooling in a future series of tracer runs started from the first iteration.

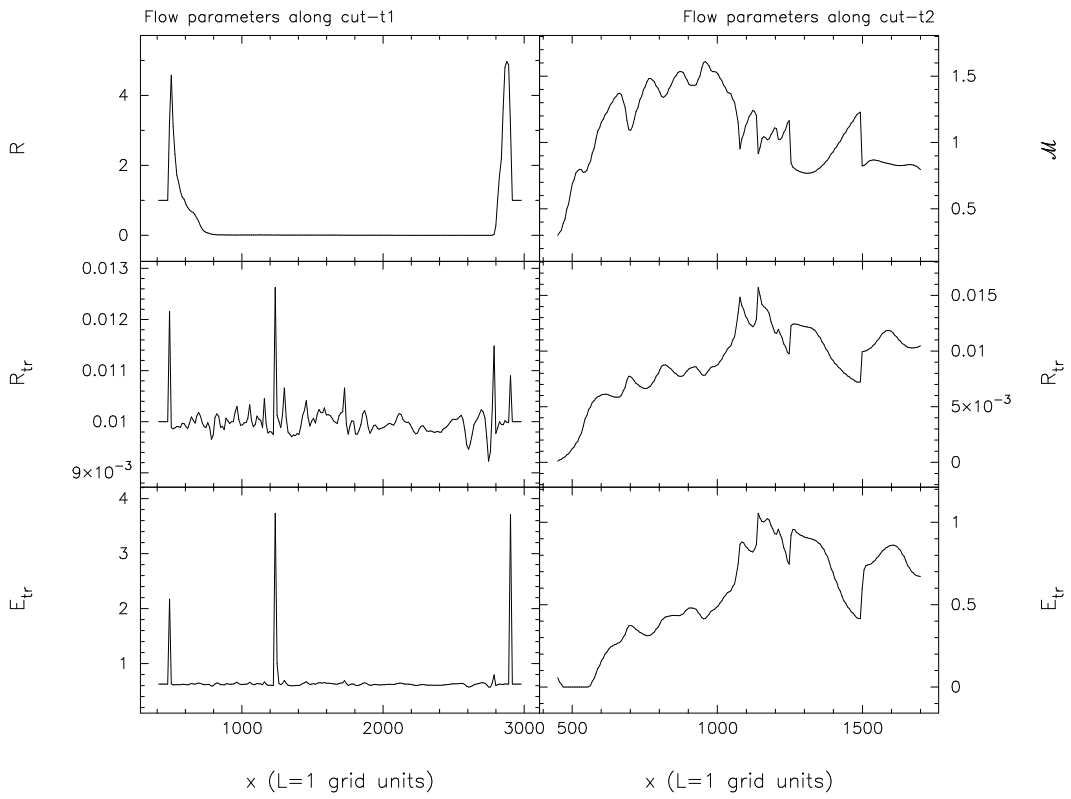

Figure 6.6: The run of the laboratory-frame hydrodynamic mass (R), laboratory-frame tracer mass density (R_{tr}), and total energy density (E_{tr}) along the same cut as cut-t1 (left panels) and the generalized Mach number ($\mathcal{M}$), laboratory-frame tracer mass density (R_{tr}), and total energy density (E_{tr}) along the same cut as cut-t2 (right panels) for the simulation shown in Fig. 6.5. The plots clearly show that tracer energization is reduced compared to the non-cooling case (see Fig. 6.4) confirming the energy-sink action of the synchrotron source term.

6.4 Discussion

Fig. 6.7 shows additional tracer simulations identical to that shown in Fig. 6.2 except that they were run with $R_{\rm crit} = 0.20$ and $R_{\rm crit} = 0.25$. These plots clearly show that tracer energization within the nebula fades as $R_{\rm crit}$ increases from 0.15. This is expected given the range of Mach numbers for the on-axis shocks shown in Fig. 5.1. Thus, the results to date show that the strength of PWN shocks places them near the borderline of the transition between transonic and supersonic making their role in cosmic-ray energization and the subsequent synchrotron energy loss from SNR/PWN systems uncertain. Thus, the question remains an interesting one that I will devote significant effort to answering in a future study.

Initial runs have shown that this simple prescription is successful in producing meaningful physical results. There are significant questions that can be addressed. A future series of simulations will elucidate how changing the cooling rate effects the shocked wind. Rough estimates of the X-ray emissivities can be computed by wrapping an axisymmetric simulation around the symmetry axis and collapsing onto a plane to obtain a 2-D projection of the flow energy density. Ultimately, the tracer mass and energy density may be used to generate a sink for the energy density of the hydrodynamic flow to initiate a study of the effects of energy loss on PWNe morphology.

The simulations presented in this chapter apply to, e.g., PSR 2224+65. Observations (Romani et al., 1997) show that the ROSAT HRI surface brightness appears to follow the limb of the nebula, brightening toward the pulsar, while the area in the vicinity of the pulsar is X-ray dark. $H\alpha$ emission is observed around the entire perimeter of the nebula, with the forward edge possessing the shape of a bow shock nebula. It is not believed that the shocked ISM can cool sufficiently to produce the X-rays, and the Balmer-line spectrum of the bow-shock nebula suggests that it is non-radiative (Cordes et al., 1993). The shocked ISM may cool within the tail, eventually

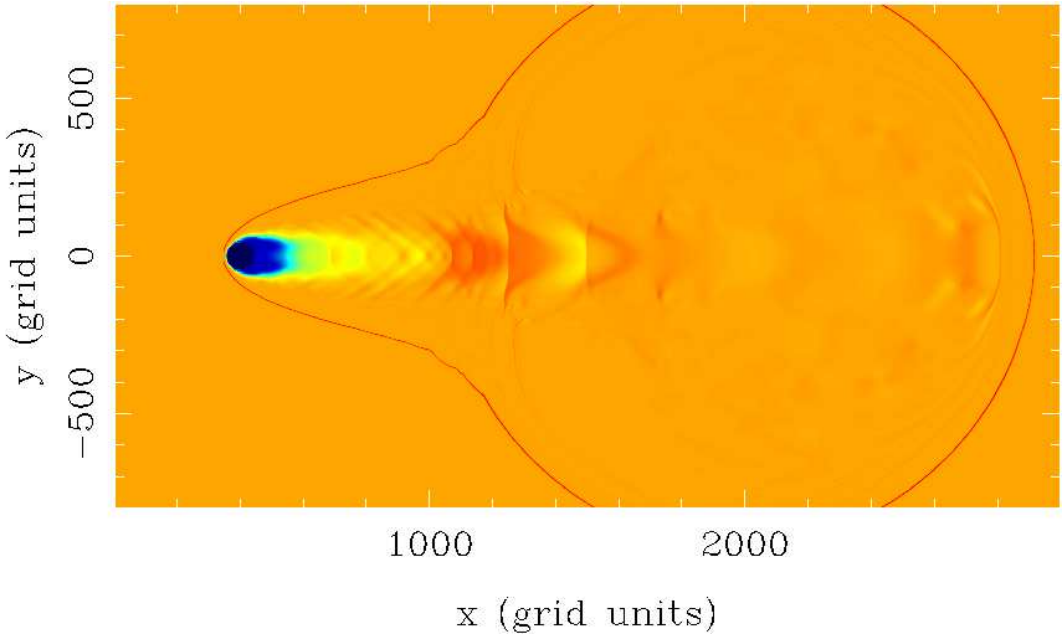

(a) Exponential tracer energy density map for $R_{\rm crit} = 0.20$.

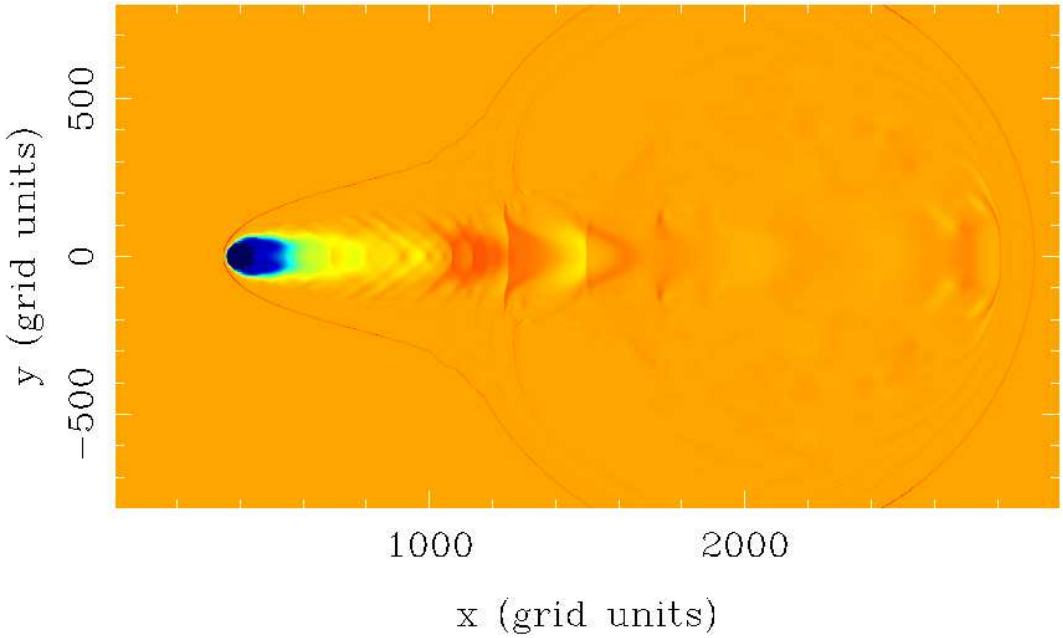

(b) Exponential tracer energy density map $R_{\rm crit} = 0.25$.

Figure 6.7: Tracer simulations identical to that in Fig. 6.2 expect $R_{\rm crit} = 0.45$ and 0.70 ($\Rightarrow \mathcal{M}_{\rm crit} \approx 1.25$, $p_{\rm crit} \approx 0.65$ and $\mathcal{M}_{\rm crit} \approx 1.39$, $p_{\rm crit} \approx 1.06$, respectively) for panel (a) and (b), respectively. The plots clearly show that tracer energization decreases as $R_{\rm crit}$ increases as expected and that energization by nebular shocks remains significant. See http://ustw.info/dissertation/figures for a high-quality electronic version.

producing limited thermal emission. Another source for the X-rays is synchrotron cooling of the swept-back relativistic pulsar wind. ISM cooling, in general, depends in a complicated way on the plasma state (e.g. Franco et al., 1994). One method of modeling is to use the collisional ionization cooling function $\Lambda_N(T)$ from Sutherland & Dopita (1993). This function is valid over a wide range of temperatures and is widely used in astrophysics. The calculation requires the gas temperature which the code does not explicitly follow. However it may be obtained from the rest-frame energy and mass densities.

The work presented in this chapter may be extended in the future to compute the physical state of the shocked pulsar wind and shocked ISM to determine whether, and under what conditions, the former or the latter dominates the X-ray emission. Thus, the code may be applied to the determination of how the pulsar's available power is distributed between radio, optical, and X-ray emission for given values of the wind speed, density, etc. Such a study, therefore, can provide a fundamental probe of pulsar energy loss and the interaction of pulsars with their environment.

6.5 Summary

I have implemented a simple model of the shock acceleration of passive tracer particles. I assume that shock acceleration proceeds via the first-order Fermi process and 1) monitor the mass density and pressure of the hydrodynamic flow and 2) flag tracer particles that experience a predetermined jump in flow density with a concomitant pressure jump. I regard flagged particles as having crossed a shock and increment their energy density. The energy increment and the magnitude of the density trigger are tunable and set the shock heating strength. The addition of a physical source term to the Euler equations accomplishes the energization.

I have further implemented a simple model of synchrotron cooling via the addition of a second physical source term. I assume the synchrotron term is proportional to the

square of the product of the energy per particle and the magnetic field. The former is calculable from the mass and energy densities, and the latter I take to be proportional to the mass density of the hydrodynamic flow. The tunable proportionality constant sets the cooling strength. Initial runs have confirmed the ability of these simple models to produce physically meaningful results justifying future work to expand the models in order to apply the newly developed code to a full exploration of the cooling of pulsar winds. The future addition of an ISM cooling model can position the code to be applied to studies of pulsar "calorimetry".

CHAPTER 7

Conclusions

7.1 Summary of Results

This work has made substantial progress in the study of asymmetric pulsar wind nebulae by bringing together techniques of computational fluid dynamics and observational X-ray astronomy. I have provided the first ultra-relativistic simulations of bow-shock PWNe for realistic pulsar space motions and wind Lorentz factors. My results elucidated the evolution of the highly elongated PWN in MSH 11–6*2* and the morphology of the Guitar nebula, and validate a long-standing interpretation of the PSR1929+10 X-ray trail. I have provided the first simulations addressing shock acceleration and synchrotron cooling within the context of ultra-relativistic backflows in bow-shock PWNe with the aim of studying PWN morphology and the origin of cosmic-rays. In summary, my main conclusions are as follows:

- Analysis of X-ray data for the SNR MSH 11–6*2* supports a model wherein the reverse shock of the SNR has asymmetrically crushed the PWN leading to the classification of the remnant as a bilateral SNR that has been dynamically impacted by the ISM rather than as one produced by the Galactic magnetic field. This suggests that there are two classes of bilateral SNRs.
- Relativistic, hydrodynamic simulations have shown that the relatively slow, dense ISM flow resulting from the space motion of a pulsar can set up an interaction with the *extremely* light, ultra-relativistic pulsar wind leading to an asymmetric nebula with a morphology reminiscent of the Guitar nebula.

- Simulations have validated the interpretation that a relativistic backflow behind PSR1929+10 is responsible for the X-ray morphology. Results further show that the backflow can harbor a series of internal shockwaves that inflates a nebular bubble, and that the bubble provides positive feedback to the backflow, explaining how the Guitar bubble persists.
- The evolution of the bubble/backflow structure is sensitive to the choice of input parameters justifying a future series of simulation runs that will determine what pulsar velocities and wind/ISM density ratios are required for the bubble/backflow feedback loop to arise.
- Simple code modules for shock acceleration and synchrotron cooling can model particle energization at shocks and time-dependent cooling within hydrodynamic, relativistic, axisymmetric simulations of PWNe. Finding a balance of these two effects such that meaningful results can be obtained over the hundreds of thousands of iterations required for nebular shocks to develop is challenging.
- Simulations have suggested that the strength of PWN shocks places them in the transition region between transonic and supersonic regimes obscuring their roll in nebular cooling and shock-acceleration of particles. Initial results indicate that PWN shocks retain the ability to energize cosmic-rays as the critical density change ($\Delta R/R$) required to trigger shock acceleration increases from 0.20 to 0.70 ($\Rightarrow \mathcal{M}_{\rm crit} \approx 1.11$–$1.39$).
- The preceding two points justify a future series of runs in order to identify optimized input parameters. The goal is to determine if shocks within PWNe can effectively accelerate charged particles leading to substantial energy loss via cooling and the generation of cosmic-rays that possibly produce γ-ray emission and ultimately escape the system. Of further interest is elucidating if the comparison of simulated emission maps with observational data can distinguish between particle acceleration to a mono-energetic or power-law distribution.

7.2 Future Work

This work lays the foundation for a future study to provide important input for cosmic-ray acceleration models via elucidating the distribution, structure, and strength of shocks formed in the pulsar wind-SNR/ISM interaction. This will be key in explaining the origin of Gamma-rays observed for a number of PWNe. NASA's Gamma-ray Large Area Space Telescope (GLAST, scheduled for a May 2008 launch) will provide the next generation of data.

An important extension of this work will be the development of an ISM cooling model. The cooling rate will be a complicated function of the plasma's physical state, e.g., elemental abundances and the plasma temperature, requiring the use of a collision-ionization, time-dependent cooling law, $\Lambda_{\rm N}$(T), such as that of Sutherland & Dopita (1993), which is applied widely to astrophysical problems. While the hydrodynamic code employed herein does not follow the gas temperature, it is obtained from the gas density and internal rest energy. Since the cooling function depends on temperature, an iterative approach will be needed to calculate the rate of cooling in one computational cycle.

The effects of cooling are germane to understanding PWN morphology; the literature is replete with examples of asymmetric PWNe. In order to realistically explore these effects, linking the tracer energy to that of the hydrodynamic flow is critical so that the synchrotron losses of the latter may be explored. With cooling models for the ISM and pulsar wind in place, an investigation of the full effects of cooling on the PWN/SNR system can be undertaken. Wind cooling is likely to dominate morphological effects since it impacts the driving energy source. ISM cooling, however, will be an important diagnostic for energy partitioning, i.e., pulsar "calorimetry". The performance of spectral and spatial emission models will elucidate pulsar energy loss and allow for a new attack on the "σ-problem".

APPENDIX

A.1 REST_FRAME Pseudo-code

PROCEDURE REST_FRAME

RECEIVED FROM PARENT PROGRAM: Y, Z

RETURNED TO PARENT PROGRAM: γ, v, C

Comment: recall $Y \equiv M/E$ and $Z \equiv R/E$.

Comment: C is returned < 0 for code failures.

GLOBAL VARIABLE: Γ

SET VALUE OF $m_{underflow}$

SET VALUE OF v_{tol}

Comment: determines iterative method velocity accuracy.

Comment: I set $v_{tol} = 10^{-8}$, 10^{-10}, 10^{-12}, 10^{-14}

Comment: for $-\log(1-Y) < 8.3$, < 10.3, < 12.3, otherwise, respectively

SET $M = \sqrt{M_x^2 + M_y^2}$

IF $M < m_{underflow}$ THEN

$v = 0$, $\gamma = 1$

Comment: avoids code failure if v is numerically zero.

ELSE

TEST FOR UNPHYSICAL PARAMETERS

IF PASSED, SET C NEGATIVE AND RETURN

IF $\log(Z) \geq -(7/9) \times \log(1-Y) - 7$, THEN

Comment: check to see if input parameters are within the acceptable.

Comment: accuracy region of the iterative routine.

CALL ITERATIVE_QUARTIC(Y, Z, v_{tol}, v, C)

Comment: updates v_{n-1} to v_n using n cycles of Newton-Raphson iteration.

Comment: returns $v = v_n$ when $|v_n - v_{n-1}| \leq v_{tol}$.

IF $C < 0$, THEN

Comment: this means the iteration failed to converge.

RETURN

ELSE

$\gamma = \sqrt{\frac{1}{1-v^2}}$

END IF

ELSE

CALL ANALYTICAL_QUARTIC(Y, Z, γ)

Comment: calculates γ using analytical solution – see below.

$v = \sqrt{1 - \frac{1}{\gamma^2}}$

END IF

END IF

END PROCEDURE REST_FRAME

PROCEDURE ANALYTICAL_QUARTIC

Comment: see §4.1.1 for equations

RECEIVED FROM PARENT PROGRAM: Y, Z

RETURNED TO PARENT PROGRAM: γ

GLOBAL VARIABLE: Γ

$\tilde{a}_3 = 2\Gamma(\Gamma - 1)Z(Y^{-2} + 1)$

$\tilde{a}_2 = (\Gamma^2 - 2\Gamma(\Gamma - 1)Y^2 - (\Gamma - 1)^2 Z^2)(Y^{-2} + 1)$

$\tilde{a}_1 = -a_3$

$\tilde{a}_0 = (\Gamma - 1)^2(Y^2 + Z^2)(Y^{-2} + 1)$

$\tilde{a}_4 = 1 + Y^2 - a_0 - a_2$

Comment: coefficients recast to counter subtractive cancellation – see §4.3.

NORMALIZE COEFFICIENTS TO a_4

Comment: e.g., $a_{3N} = a_3/a_4$.

CALCULATE CUBIC RESOLVENT COEFFICIENTS

CALCULATE DISCRIMINANT, D

IF $D \leq 0$ THEN

WRITE ERROR MESSAGE AND STOP

Comment: exploration suggests $D \leq 0$ is unphysical but formal proof is elusive;

Comment: thus, I leave $D \leq 0$ uncoded with a error flag just in case.

ELSE

Comment: $D > 0 \Rightarrow Q(\gamma)$ has 2 real roots (see Tab. 4.1 & 4.2)

CALCULATE ROOTS OF CUBIC RESOLVENT

Comment: the cubic has one real root and a pair of complex conjugate roots.

IF REAL ROOT < 0, SET REAL ROOT $= 0$

Comment: the real root cannot be less than zero analytically.

Comment: numerically, however, it can have a very small negative value.

CALCULATE THE TWO REAL ROOTS OF THE QUARTIC

TEST FOR TWO OR NO PHYSICAL ROOTS

IF PASSED, WRITE ERROR MESSAGE, AND RETURN

IF FAILED, SET γ = PHYSICAL ROOT

END IF

END PROCEDURE ANALYTICAL_QUARTIC

A.2 Tracer Pseudo-code

PROCEDURE SETUP_PROBLEM (TRACER-SPECIFIC CONTENT ONLY)

Comment: non-tracer coding omitted.

IF TRACERS DEFINED THEN INCLUDE TRACER GLOBAL VARIABLES

Comment: non-tracer coding omitted.

IF TRACERS DEFINED THEN

SET TRACER REST-FRAME MASS DENSITY: $n_{tr} = C_1 \times n$, $C_1 < 1$

Comment: n is hydro flow mass density.

SET TRACER REST-FRAME ENERGY DENSITY: $e_{tr} = C_2 \times n_{tr}$, $C_2 > 1$

SET TRACER REST-FRAME PRESSURE: $p_{tr} = e_{tr}/3$

Comment: assumes relativistic species $\Rightarrow$ tracer adiabatic index is 4/3.

SET MULTIPLIER FOR SYNCHROTRON SOURCE TERM, C_{syn}

Comment: tunable knob: sets strength of synchrotron cooling.

SET CRITICAL DENSITY CHANGE, R_{crit}

Comment: tunable knob sets minimum change for shock acceleration activation.

CALCULATE MACH NUMBER FOR R_{crit}

CALCULATE CONCOMITANT PRESSURE CHANGE, P_{crit}

SET ENERGY ADDED BY SHOCK ACCELERATION, $shockDE$

CALCULATE TRACER LAB FRAME MASS DENSITY, R_{tr}

CALCULATE TRACER LAB FRAME ENERGY DENSITY, E_{tr}

Comment: from rest-frame quantities using hydro flow velocity.

END IF

Comment: non-tracer coding omitted.

END PROCEDURE SETUP_PROBLEM

PROCEDURE SET_SPHERE (TRACER-SPECIFIC CONTENT ONLY)

Comment: calculates weighted flow variables given the fraction of the area of.

Comment: a cell falling inside the hemispherical outflow boundary.

Comment: non-tracer coding omitted.

IF TRACERS DEFINED THEN INCLUDE TRACER GLOBAL VARIABLES

Comment: non-tracer coding omitted.

IF TRACERS DEFINED THEN

SET REST-FRAME TRACER MASS DENSITY: $n_{tr}^{ave} = C_1 \times n^{ave}$

SET REST-FRAME TRACER ENERGY DENSITY: $e_{tr}^{ave} = C_2 \times n_{tr}^{ave}$

Comment: C_1, C_2 are from *SETUP_PROBLEM* above.

Comment: n^{ave} is the weighted mass density for hydro the flow.

SET WEIGHTED TRACER PRESSURE: $p_{tr}^{ave} = e_{tr}^{ave}/3$

Comment: assumes relativistic species.

CALCULATE TRACER LAB FRAME MASS DENSITY, R_{tr}^{ave}

CALCULATE TRACER LAB FRAME ENERGY DENSITY, E_{tr}^{ave}

Comment: from rest-frame quantities using hydro weighted flow velocity.

END IF

Comment: non-tracer coding omitted.

END PROCEDURE SET_SPHERE

PROCEDURE MESH_UPDATE (TRACER-SPECIFIC CONTENT ONLY)

RECEIVED FROM PARENT PROGRAM: LEVEL #, GRID #, & STEP #

RETURNED TO PARENT PROGRAM: none (variables are common)

Comment: updates the flow variables given the RHLLE fluxes.

Comment: STEP = 1 (half time-step) or 2 (full time step – see §3.1).

Comment: non-tracer coding omitted.

IF TRACERS DEFINED THEN

INCLUDE TRACER GLOBAL VARIABLES

INITIALIZE VARIABLE $S_{phys}(K)$ TO ZERO, K=1,2,...,6

Comment: first call only.

INITIALIZE VARIABLE $SHOCKFLAG$ and $SHOCKFLAGo$ TO ZERO

Comment: first call only.

END IF

Comment: non-tracer coding omitted.

IF TRACERS DEFINED THEN

SET SYNCHROTRON SOURCE TERM: $S_{syn} = C_{syn} \times (n \times e_{tr}/n_{tr})^2$

Comment: n is the hydro flow rest-frame mass density.

SET PHYSICAL SOURCE TERM: $S_{phys}(6) = -S_{syn}$

Comment: to be distinguished from coordinate source term from axisymmetry.

IF $SHOCKFLAG = 1$ FOR COMPUTATIONAL CELL

SET $S_{phys}(6) = S_{phys}(6) + shockDE$

SET $SHOCKFLAGo = 0$

ELSE

SET $S_{phys}(6) = S_{phys}(6)$

END IF

END IF

Comment: non-tracer coding omitted.

IF TRACERS DEFINED THEN

CALCULATE CHANGE IN FLOW VARIABLES INCLUDING $S_{Sphys}(K)$

Comment: $S_{phys}(K)$ is only non-zero for $K = 6$.

ELSE

CALCULATE CHANGE IN FLOW VARIABLES WITHOUT $S_{phys}(K)$

END IF

Comment: non-tracer coding omitted.

IF TRACERS DEFINED THEN

IF $K = 6$ THEN

IF $E_{tr} < 0$ THEN SET $E_{tr} = 10^{-30}$

Comment: this test is performed after the flow variables are updated.

Comment: given that S_{syn} is an energy sink, this protects against negative energy.

END IF

Comment: note that the following density tests are for the lab frame quantity,

Comment: while the pressure tests are for the rest frame – this should not be

Comment: problematic as I seek unambiguous shocks flagged in both frames.

IF TEMPORAL SHOCK-FLAGGING SELECTED THEN

IF STEP = 2 & NEW & OLD HYDRO MASS DENSITY > 0 THEN

ELSE IF SPATIAL SHOCK-FLAGGING SELECTED THEN

IF STEP = 2 & HYDRO MASS DENSITY > 0 THEN

Comment: density positive for current cell AND those to the N, S, E, and W.

CONTINUE

Comment: one of the above must be selected.

CALL REST_FRAME (see §A.1)

Comment: temporal: for both new & old hydro variables in order to obtain pressures.

Comment: spatial: for hydro variables for all 5 cells in order to obtain pressures.

IF DENSITY & PRESSURE CHANGE SUFFICIENT THEN

Comment: checks density & pressure change against R_{crit}, P_{crit}.

Comment: temporal only one difference to check.

Comment: spatial: only one of N, S, E, OR W needs be have above critical difference.

IF $SHOCKFLAGo = 0$ THEN

Comment: add energy only if density & pressure tests were not tripped last iteration.

SET $SHOCKFLAG = 1$

END IF

ELSE

$SHOCKFLAG = 0$

$SHOCKFLAGo = 0$

END IF

END IF

END IF

END PROCEDURE MESH_UPDATE

REFERENCES

Arnaud, K. A. 1996, in ASP Conf. Series, ed. G. Jacoby & J. Barnes, Vol. 101, 17

Arons, J. 2002, in Astronomical Society of the Pacific Conference Series, Vol. 271, Neutron Stars in Supernova Remnants, ed. P. O. Slane & B. M. Gaensler, 71

Arzoumanian, Z., Chernoff, D. F., & Cordes, J. M. 2002, *ApJ*, 568, 289

Becker, W. & Truemper, J. 1997, *A&A*, 326, 682

Begelman, M. C. 1998, *ApJ*, 493, 291

Berezhko, E. G. & Ellison, D. C. 1999, *ApJ*, 526, 385

Berger, M. J. 1982, PhD thesis, Stanford Univ.

Berger, M. J. & Colella, P. 1989, Journal of Computational Physics, 82, 64

Bietenholz, M. F. & Kronberg, P. P. 1991, *ApJ*, 368, 231

Blandford, R. D. & Rees, M. J. 1974, *MNRAS*, 169, 395

Blondin, J. M., Chevalier, R. A., & Frierson, D. M. 2001, *ApJ*, 563, 806

Bogovalov, S. V., Chechetkin, V. M., Koldoba, A. V., & Ustyugova, G. V. 2005, *MNRAS*, 358, 705

Borkowski, K. J. 2000, in Revista Mexicana de Astronomia y Astrofisica Conference Series, Vol. 9, Revista Mexicana de Astronomia y Astrofisica Conference Series, ed. S. J. Arthur, N. S. Brickhouse, & J. Franco, 288

Borkowski, K. J., Lyerly, W. J., & Reynolds, S. P. 2001, *ApJ*, 548, 820

Brazier, K. T. S. & Johnston, S. 1999, *MNRAS*, 305, 671

Bronshtein, I. N. & Semendyayev, K. A. 1997, Handbook of Mathematics, ed. K. A. Hirsch, 3rd edn. (Springer-Verlag Telos)

Bucciantini, N. 2002, *A&A*, 387, 1066

—. 2008, Advances in Space Research, 41, 491

Bucciantini, N., Amato, E., & Del Zanna, L. 2005, *A&A*, 434, 189

Chatterjee, S. & Cordes, J. M. 2002, *ApJ*, 575, 407

Cheng, K. S. & Zhang, L. 1999, *ApJ*, 515, 337

Chevalier, R. A. 1977, in Supernovae, ed. D. N. Schramm (D. Reidel Publ. Co., Dordrecht, Holland), 53

—. 2000, *ApJ*, 539, L45

Chevalier, R. A., Scott, J. S., & Robertson, J. W. 1976, *ApJ*, 207, 450

Contopoulos, I. & Kazanas, D. 2002, *ApJ*, 566, 336

Cordes, J. M. & Chernoff, D. F. 1998, *ApJ*, 505, 315

Cordes, J. M., Romani, R. W., & Lundgren, S. C. 1993, *Nature*, 362, 133

Courant, R., Friedrichs, K., & Lewy, H. 1928, Mathematische Annalen, 100, 32, in German, translation in: IMB J., 1968 (March), 215-234

Del Zanna, L., Amato, E., & Bucciantini, N. 2004, *A&A*, 421, 1063

Del Zanna, L. & Bucciantini, N. 2002, *A&A*, 390, 1177

Del Zanna, L., Bucciantini, N., & Londrillo, P. 2003, *A&A*, 400, 397

Del Zanna, L., Volpi, D., Amato, E., & Bucciantini, N. 2006, *A&A*, 453, 621

Delettrez, J. A., Myatt, J., Radha, P. B., Stoeckl, C., Skupsky, S., & Meyerhofer, D. D. 2005, Plasma Physics and Controlled Fusion, 47, B791

Dodson, R., Legge, D., Reynolds, J. E., & McCulloch, P. M. 2003, *ApJ*, 596, 1137

Dubner, G., Giacani, E., Gaensler, B. M., Goss, W. M., & Green, A. 2002, in Astronomical Society of the Pacific Conference Series, Vol. 271, Neutron Stars in Supernova Remnants, ed. P. O. Slane & B. M. Gaensler, 415

Duncan, A. R., Stewart, R. T., Haynes, R. F., & Jones, K. L. 1996, *MNRAS*, 280, 252

Duncan, G. C. & Hughes, P. A. 1994, *ApJ*, 436, L119

Dyer, K. K., Reynolds, S. P., & Borkowski, K. J. 2004, *ApJ*, 600, 752

Einfeldt, B. 1988, SIAM J. Numerical Analysis, 25, 294

Ellison, D. C. & Cassam-Chenaï, G. 2005, *ApJ*, 632, 920

Emmering, R. T. & Chevalier, R. A. 1987, *ApJ*, 321, 334

Fermi, E. 1949, Physical Review, 75, 1169

Franco, J., Miller, W. W. I., Arthur, S. J., Tenorio-Tagle, G., & Terlevich, R. 1994, *ApJ*, 435, 805

Fryxell, B., Olson, K., Ricker, P., Timmes, F. X., Zingale, M., Lamb, D. Q., MacNeice, P., Rosner, R., Truran, J. W., & Tufo, H. 2000, *ApJS*, 131, 273

Fulbright, M. S. & Reynolds, S. P. 1990, *ApJ*, 357, 591

Gaensler, B. M. 1998, *ApJ*, 493, 781

Gaensler, B. M., Hendrick, S. P., Reynolds, S. P., & Borkowski, K. J. 2003, *ApJ*, 594, L111

Gaensler, B. M. & Slane, P. O. 2006, *ARA&A*, 44, 17

Gammie, C. F., McKinney, J. C., & Tóth, G. 2003, *ApJ*, 589, 444

Godunov, S. K. 1959, Mat. Sb., 47, 271, in Russian, translation in: US Joint Publ. Res. Service, JPRS, 7226 (1969)

Gonzalez, M. & Safi-Harb, S. 2003, *ApJ*, 591, L143

Gotthelf, E. V. 2003, *ApJ*, 591, 361

Graebner, G. 1985, PhD thesis, Frankfurt

Harrus, I. M., Hughes, J. P., & Slane, P. O. 1998, *ApJ*, 499, 273

Harten, A., Lax, P., , & Van Leer, B. 1983, SIAM Rev., 25, 35

Heger, A., Fryer, C. L., Woosley, S. E., Langer, N., & Hartmann, D. H. 2003, *ApJ*, 591, 288

Hirano, T. 2004, Journal of Physics G Nuclear Physics, 30, S845

Horns, D., Aharonian, F., Hoffmann, A. I. D., & Santangelo, A. 2007, *Ap&SS*, 309, 189

Hughes, J. P., Slane, P. O., Park, S., Roming, P. W. A., & Burrows, D. N. 2003, *ApJ*,

591, L139

Hughes, P. A. 2005, *ApJ*, 621, 635

Hughes, P. A., Miller, M. A., & Duncan, G. C. 2002, *ApJ*, 572, 713

Hui, C. Y. & Becker, W. 2007, *A&A*, 467, 1209

Ibanez, J. M. 2003, in Lecture Notes in Physics, Berlin Springer Verlag, ed. L. Fernández-Jambrina & L. M. González-Romero, Vol. 617, 113

Inoue, H. 1993, Experimental Astronomy, 4, 1

Jackson, M. S., Safi-Harb, S., Kothes, R., & Foster, T. 2008, *ApJ*, 674, 936

Jung, G. V. 1989, *ApJ*, 338, 972

Kargaltsev, O. & Pavlov, G. G. 2008, ArXiv e-prints, 801

Kato, T. N. & Takahara, F. 2003, *MNRAS*, 342, 639

Kennel, C. F. & Coroniti, F. V. 1984a, *ApJ*, 283, 694

—. 1984b, *ApJ*, 283, 710

Kesteven, M. J. & Caswell, J. L. 1987, *A&A*, 183, 118

Kirk, J. G. & Skjæraasen, O. 2003, *ApJ*, 591, 366

Komissarov, S. S. 1999, *MNRAS*, 303, 343

Lyutikov, M. 2003, *MNRAS*, 339, 623

Martí, J. M. & Müller, E. 2003, Living Reviews in Relativity, 6

Matheson, H. & Safi-Harb, S. 2005, Advances in Space Research, 35, 1099

Melatos, A. 2004, in IAU Symposium, Vol. 218, Young Neutron Stars and Their Environments, ed. F. Camilo & B. M. Gaensler, 143

Michel, F. C. 1969, *ApJ*, 158, 727

—. 1973, *ApJ*, 180, L133

Mignone, A. & McKinney, J. C. 2007, *MNRAS*, 378, 1118

Millikan, R. A. 1925, Science, 62, 445

Mori, K., Burrows, D. N., Hester, J. J., Pavlov, G. G., Shibata, S., & Tsunemi, H. 2004, *ApJ*, 609, 186

Noble, S. C. 2003, ArXiv General Relativity and Quantum Cosmology e-prints

Norman, M. L. & Winkler, K.-H. A. 1986, in NATO Advanced Research Workshop on Astrophysical Radiation Hydrodynamics, ed. K.-H. A. Winkler & M. L. Norman (D. Reidel Publishing Co., Dordrecht, Holland), 449

Orlando, S., Bocchino, F., Reale, F., Peres, G., & Petruk, O. 2007, *A&A*, 470, 927

Pacini, F. & Salvati, M. 1973, *ApJ*, 186, 249

Perret-Gallix, D. 2006, Concluding remarks: Emerging topics, Proceedings of the X International Workshop on Advanced Computing and Analysis Techniques in Physics Research - ACAT 05

Possenti, A., Cerutti, R., Colpi, M., & Mereghetti, S. 2002, *A&A*, 387, 993

Quirk, J. J. 1991, PhD thesis, Cranfield Inst. Tech.

Rees, M. J. & Gunn, J. E. 1974, *MNRAS*, 167, 1

Reynolds, S. P. & Chevalier, R. A. 1984, *ApJ*, 278, 630

Rieger, F. M., Bosch-Ramon, V., & Duffy, P. 2007, *Ap&SS*, 309, 119

Roberts, M. S. E. 2004, The Pulsar Wind Nebula Catalog (March 2005 version), WWW: http://www.physics.mcgill.ca/%7Epulsar/pwncat.html

Roberts, M. S. E., Tam, C. R., Kaspi, V. M., Lyutikov, M., Vasisht, G., Pivovaroff, M., Gotthelf, E. V., & Kawai, N. 2003, *ApJ*, 588, 992

Romani, R. W., Cordes, J. M., & Yadigaroglu, I.-A. 1997, *ApJ*, 484, L137

Schneider, V., Katscher, U., Rischke, D. H., Waldhauser, B., Maruhn, J. A., & Munz, C.-D. 1993, Journal of Computational Physics, 105, 92

Sedov, L. I. 1959, Similarity and Dimensional Methods in Mechanics (Similarity and Dimensional Methods in Mechanics, New York: Academic Press, 1959)

Shapiro, M. M. & Silberberg, R. 1977, in International Cosmic Ray Conference, Vol. 2, International Cosmic Ray Conference, 20

Shibata, M. 2003, Phys. Rev. D, 67, 024033

Slane, P., Helfand, D. J., van der Swaluw, E., & Murray, S. S. 2004, *ApJ*, 616, 403

Sutherland, R. S. & Dopita, M. A. 1993, *ApJS*, 88, 253

Taylor, G. I. 1950a, Proc. R. Soc. London A, A201, 159

—. 1950b, Proc. R. Soc. London A, A201, 175

Thompson, K. W. 1986, Journal of Fluid Mechanics, 171, 365

Tregillis, I. L., Jones, T. W., & Ryu, D. 2001, *ApJ*, 557, 475

Uchiyama, Y., Aharonian, F. A., Tanaka, T., Takahashi, T., & Maeda, Y. 2007, *Nature*, 449, 576

Vallée, J. P. 2005, *AJ*, 130, 569

van der Swaluw, E. 2005, Advances in Space Research, 35, 1123

van der Swaluw, E., Achterberg, A., & Gallant, Y. A. 1998, Memorie della Societa Astronomica Italiana, 69, 1017

van der Swaluw, E., Achterberg, A., Gallant, Y. A., Downes, T. P., & Keppens, R. 2003, *A&A*, 397, 913

van der Swaluw, E., Achterberg, A., Gallant, Y. A., & Tóth, G. 2001, *A&A*, 380, 309

van der Swaluw, E., Downes, T. P., & Keegan, R. 2004, *A&A*, 420, 937

van Leer, B. 1979, Journal of Computational Physics, 32, 101

Vigelius, M., Melatos, A., Chatterjee, S., Gaensler, B. M., & Ghavamian, P. 2007, *MNRAS*, 374, 793

Vlahakis, N. 2004, *ApJ*, 600, 324

Wang, Q. D., Gotthelf, E. V., Chu, Y.-H., & Dickel, J. R. 2001, *ApJ*, 559, 275

Wang, Q. D., Li, Z.-Y., & Begelman, M. C. 1993, *Nature*, 364, 127

Weaver, R., McCray, R., Castor, J., Shapiro, P., & Moore, R. 1977, *ApJ*, 218, 377

Weisskopf, M. C., O'dell, S. L., & van Speybroeck, L. P. 1996, in Proc. SPIE, ed. R. B. Hoover & A. B. Walker, Vol. 2805, 2

Willingale, R., West, R. G., Pye, J. P., & Stewart, G. C. 1996, *MNRAS*, 278, 749

Wilms, J., Allen, A., & McCray, R. 2000, *ApJ*, 542, 914

Zhang, W., Woosley, S. E., & MacFadyen, A. I. 2003, *ApJ*, 586, 356